# THE GROWTH AND LOCALIZED BREAKDOWN OF THE PASSIVE FILM ON IRON IN 0.05 M NaOH STUDIED *IN SITU* USING RAMAN MICROSCOPY AND POTENTIODYNAMIC POLARIZATION

Michél Karin Nieuwoudt

A thesis submitted to the Faculty of Science, University of the Witwatersrand, Johannesburg, in fulfilment of the requirements for the degree of Doctor of Philosophy

Johannesburg, October 2012

# DECLARATION

I declare that this thesis is my own, unaided work. It is being submitted for the Degree of Doctor of Philosophy in the University of the Witwatersrand, Johannesburg. It has not been submitted before for any degree or examination in any other University.

MK Nieuwoudt

26th day of October 2012 in Auckland

# ABSTRACT

A unique Raman spectroscopic investigation combining a number of different techniques has been conducted *in situ* on the composition of the passive film on iron, both during its growth in 0.05 M NaOH by potentiodynamic polarization and during localized breakdown by pitting after addition of 0.05 M NaCl.

There are differing theories for the mechanism of pit initiation and formation in the passive film on iron, and while these are in part due to different environmental factors, they are also influenced by differing theories for the nature of the passive film. The detailed information obtained in this study corroborate the two layer model for the passive film on iron, with $\gamma$-$Fe_2O_3$ forming the inner layer and the outer layer consisting of $\delta$-FeOOH, $\alpha$-FeOOH, $\gamma$-FeOOH, other components such as $Fe(OH)_2$ and other intermediates. In the passive region of anodic polarization the film became increasingly hydrated with increasing anodic potential and with increased cycles became amorphous, comparing well with the Hydrated Polymeric Oxide model.

Pre-resonance enhancement of the Raman bands of iron oxides and particularly iron oxy-hydroxides was afforded by excitation at 636.4 nm, and particularly at low wavenumbers. The use of Multivariate Curve Resolution with Alternating Least Squares (MCR-ALS) enabled determination of the relative amounts of the iron oxide and oxy-hydroxide components from the complex spectra recorded during potentiodynamic polarization. The amount of water incorporated in the passive film under the same conditions was also monitored *in situ* at similar potentials using excitation at 514.5 nm.

Addition of chloride ions resulted in an increase in hydration and a change of the composition of the passive film to comprise mainly $\beta$-FeOOH and Green complex with some $\gamma$-$Fe_2O_3$ and $\gamma$-FeOOH. At the pitting potential significant changes in the composition occurred along with reduction in hydration, so that re-passivation could no longer be maintained at the same rate as dissolution by the chloride ions, enabling stable pitting. These observations indicate that water plays a protective role in the passive film and reinforce the mechanisms for pit initiation based on the De-passivation–Re-passivation theory and Chemical Dissolution theory.

# DEDICATION

*I would like to dedicate this to my Dad*

*Otto August Huckschlag*

*1935 - 1998*

# ACKNOWLEDGEMENTS

This research would not have been possible without the constant support, encouragement, patient guidance and wisdom of my supervisor, Prof. Darrell Comins. I am deeply grateful for this. I also wish to thank my co-supervisor, Prof. Ignacy Cukrowski, for his positivity, encouragement and expert help. I am deeply grateful to both for their invaluable contributions.

I would like to thank my family and friends who have encouraged me during the course of this study, in particular my Mum, my husband, Piet and my girls, Natalie, Claire, Christine and Melanie: thank you for your patience and support and for believing in me.

I would also like to thank those who have contributed in many helpful ways to the experiments: Buddhika Gunawardana for her kind provision of some of the iron oxides used to create the standard Raman reference spectra, Rudolph Erasmus for his expert and going-the-extra-mile type help in the Raman laboratory, particularly over the last year, Paul Stoddart for the design of the electrochemical cell and for his enthusiasm in stimulating my interest in this research, André van Benekom for helpful discussions in commissioning the electrochemical cell, Barry Fairbrother and Steve Gannon for their glassblowing expertise and Shaun Riekert, Andrew Carpede and Steve van der Schyff for their expertise in the construction of the electrochemical cell and help with the other equipment. I am also grateful to Anna de Juan for her kind email correspondence and helpful advice with the MCR-ALS optimization.

Finally, I wish to acknowledge the support of the South African National Research Foundation under Grant Number 2053306, the Materials Physics Research Institute, University of the Witwatersrand and the DST/NRF Centre of Excellence in Strong Materials.

# TABLE OF CONTENTS

# LIST OF FIGURES

# LIST OF TABLES

# CHAPTER 1
# INTRODUCTION

## 1.1. GENERAL INTRODUCTION

Iron is the major component of steel and can comprise up to 80 % of some stainless steels. The main advantage of stainless steels over pure iron is their increased resistance to corrosion in environments exposed to oxygen and water; addition of selected amounts of other metals such as Cr, Mo, Mn, Ni, Cu and V enables the spontaneous formation of a stable passive film of metal oxide on the surface which acts as a barrier to further oxidation. This is mainly because the passive film inhibits ionic transport, thus significantly reducing or preventing the transport rate of reactant species through the layer. An alternate viewpoint is that that the passive film as a barrier layer serves as a resistor to drop a large part of the applied voltage, thus lowering the electric field at the interface with a consequent decrease in the corrosion rate [1]. In the case of pure iron, the oxide film that spontaneously forms on the surface does not impede further corrosion to the same extent. Exposure of the iron surface to water and oxygen will result in spontaneous oxidation by $O_2$ as follows [2]:

$$Fe \rightarrow Fe^{2+} + 2e^{-}$$

driven by the reduction of water or $OH^{-}$:

$$\tfrac{1}{2}O_2 + H_2O + 2e^{-} \rightarrow 2OH^{-}$$ (in neutral/basic solutions)

or

$$\tfrac{1}{2}O_2 + 2H^{+} + 2e^{-} \rightarrow 2H_2O$$ (in acid solutions)

These reactions occur spontaneously because the reduction potential of oxygen is greater than that of iron and so the oxidation of iron is driven by reduction of oxygen. The other factor driving the corrosion process is the acid-base interaction [3] between water or anions in the electrolyte and the $Fe^{2+}$ ions. The $Fe^{2+}$ ions produced by the oxidation reaction are the Lewis acid relative to the water molecules (or $OH^{-}$ ions in alkaline solution), and are transferred into solution where they undergo Lewis acid-base reactions to form hydrated aquo-metal ions or aniono-complexes of metal ions [3].

At pH > 4, the corrosion reactions result in the formation of $Fe(OH)_2$ which is further oxidized by $O_2$ to $Fe_3O_4$ and FeOOH or $Fe_2O_3.H_2O$, which is rust.

The iron surface can, however, be made more corrosion resistant or passive if it is exposed to a strong oxidant, or if it is subjected to electrochemical techniques which involve application of constant potential, constant current or potentiodynamic polarization. In the latter technique the applied potential is increased at a fixed rate and the current fluctuations resulting from oxidation reactions occurring on the metal surface may be observed in a polarization curve of current vs. applied potential [4,5]. The passive region in the polarization curve may be defined such that a substantial reduction is reached in the rate of oxidation of the metal surface [5]; this occurs at relatively high anodic potentials.

Although metals with passive films have the advantage of being more corrosion resistant, they are more susceptible to localized corrosion such as pitting, in which metal is removed preferentially from vulnerable sites on the surface, usually at areas such as grain boundaries or at visible surface defects. The latter comprise inclusions in the metal surface, pores, flaws, second phase precipitates or weak spots produced by the cold-working and heated processes for stainless steels [6]. An *in situ* study measuring the distribution of $Cl^-$ ions at the metal/solution interface using Scanning Combination Microelectrodes has shown that adsorption of aggressive anions such as $Cl^-$ from the surrounding medium is more pronounced at these sites than elsewhere [7]. When aggressive anions are present in solution they migrate to these areas and pit growth occurs there as a result of increased rate of metal dissolution. This induces the localized formation of an aggressive environment resulting from hydrolysis and dissolution of the metal, thus forming a metal salt which hydrolyses in water to form an insoluble oxide and acid [2]:

$$MCl_2 + 2H_2O \rightarrow M(OH)_2 + 2HCl \qquad (\text{in the presence of } Cl^-)$$

or

$$MSO_4 + 2H_2O \rightarrow M(OH)_2 + H_2SO_4 \qquad (\text{in the presence of } SO_4^{2-}).$$

Some of the $M(OH)_2$ products that form initially will readily be oxidized to form for e.g., $M_3O_4$, $M_2O_3$ and MOOH or $M_2O_3.H_2O$ compounds. The fresh oxide that is formed adheres to the surface, allowing momentary repair but after repeated collapses and repairs the liquid in the small area will become acidic

enough for metal ions to pass into the liquid. The $H^+$, $Cl^-$ or $SO_4^{2-}$ ions in the solution thus stimulate rapid metal dissolution forming a micro-depression or pit in the surface while oxygen reduction occurs on adjacent surfaces. The rapid dissolution in turn produces an excess of $H^+$ ions which then stimulate more $Cl^-$ ions to migrate into the pit, eventually resulting in a high concentration of $H^+$ and $Cl^-$ ions there. This sequence of events is basically illustrated in the schematic diagram shown in Figure 1.1 below.

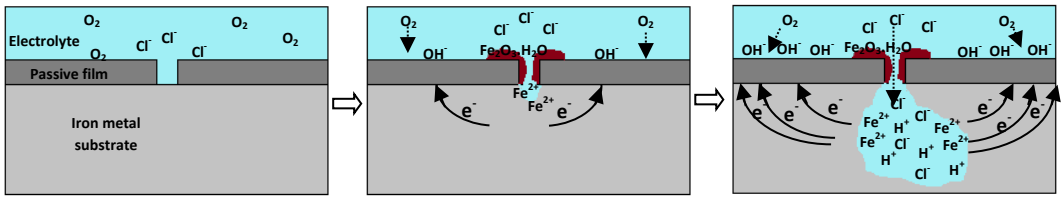


Figure 1.1 Schematic diagram illustrating the sequence of events in stable pit growth

This results in diminished solubility of $O_2$ which prevents formation of insoluble hydroxides and a stable pit begins to form [2]. This can progress to insidious dissolution of the iron under a small pin-hole on the surface, resulting in unexpected mechanical failure of metal structures.

The performance of these metals is thus severely limited in circumstances where otherwise low corrosion rates would be expected, such as in the industrial use of not only stainless steels and related alloys, but also aluminium and aluminium-base, nickel-base and titanium-base alloys [8]. Pitting corrosion is of major commercial significance and as a result has been the subject of many studies by others and described in an extensive body of literature. The mechanism of pit growth, once pitting is underway, is well understood; but there is less agreement on the mechanisms of pit initiation and formation in the stages leading up to stable pit growth. During the induction time before stable pit growth, localized breakdown of the passive film begins to occur followed almost immediately by re-growth of the film. Different theories for the events occurring at the metal surface and in the passive film leading up to and during this period have been proposed. While the differences in these theories are in part due to different environmental factors, they are also influenced by the different theories for the nature of the passive film.

## 1.2. OBJECTIVES

The aim of the present work was to examine the composition of the passive film formed on pure iron, and subsequently at the stage at which stable pitting occurs under the influence of chloride ions. Many pitting studies have been conducted with potentiodynamic polarization in buffered solutions of pH 8-14, which are particularly suitable for *in situ* Raman microscopic monitoring of the passive film in the presence of chloride anions. At these pH values the passive films undergo longer induction times before stable pitting occurs, during which transient spikes in current are observed due to pitting events followed by re-passivation of the surface. A solution of 0.05 M NaOH (pH 12.7) has been chosen for study, because passive films are more stable under alkaline environments compared with acidic or neutral environments, and undergo longer induction times for pitting [9], which enables more time for controlled Raman spectra.

The techniques that are used to investigate the nature and breakdown of the passive film on iron are *in situ* Raman microscopy with potentiodynamic polarization. Potentiodynamic polarization is used for the electrochemical control of the iron surface and is the method fundamental to the study of the formation of passive films and their pitting behaviour. As the potential is varied, the changes in current resulting from the oxidation and reduction reactions occurring on the iron surface are monitored.

Raman spectroscopy is an ideal technique for investigating the composition of the passive film because it is non-destructive and enables *in situ* measurement of the iron surface during electrochemical control. It has been used during electrochemical control to detect iron oxides on the iron surface [10-19]. However its success was limited, chiefly because the Raman cross sections of the iron oxide compounds were very weak under the excitation wavelengths used. This resulted in very weak spectral bands, and the necessary use of increased number of polarization cycles to increase the passive layer thickness inevitably resulted in changes of its composition. Different compositions have therefore been suggested for the passive film on iron using this technique, even under similar experimental conditions. Also contributing to the variety of conclusions is the fact that the strongest bands of some of the different iron oxides used to identify them occur at

or near the same frequency and it has not been possible to distinguish between them clearly.

The present study provides a fresh Raman spectroscopic investigation of the composition of the passive film by increasing the intensity of the Raman bands using pre-resonance enhancement. In this phenomenon enhancements of up to ten times can be obtained when the excitation frequency approaches, but does not coincide with, one of the electronic transitions. This is described in greater detail in Chapter 2, section 2.3. The enhanced intensity enables firstly the improved characterization of the iron oxide compounds in the passive film during its growth by electrochemical polarization, and secondly, identification of the changes in the composition of the film which have been found to occur at the critical pitting potential from ellipsometry and electrochemical studies [20,21]. Detailed potentiodynamic [22-24] and ellipsometric [21,25,26] studies on iron in 0.05 M NaOH have already been described in the literature in which changes have been observed in the composition of the passive film associated with pitting. These studies have prompted this investigation into the composition of the film, particularly under pitting conditions in the presence of chloride ions.

Furthermore, because water has been found to play a prominent role in the passive film [6,25,27-33], the same techniques are used to monitor the behaviour of water incorporated in the surface, and thereby gain more insight into the role played by water, which appears to be subject to differences of opinion. Characterization of the composition of iron oxide compounds and monitoring the changes in the amount of water on the film in 0.05M NaOH at different stages of pitting under the influence of chloride ions would contribute to a better understanding of the mechanism of pitting of iron, specifically under these conditions.

A study of the pre-resonance enhancement of the Raman spectra of the iron oxide compounds using a tuneable dye laser is described Chapter 4, which has been published in the *Journal of Raman Spectroscopy* **2011**; *42*, 1335. In Chapter 5, the use of such enhancement to study the composition of the passive film is described during its growth using potentiodynamic polarization of the iron surface in 0.05M NaOH. This study has been published in the *Journal of Raman Spectroscopy* **2011**; *42*, 1353. Chapter 6 describes the application of these techniques to study the composition of the film *in situ* under pitting conditions

resulting from the addition of 0.05 M chloride ions and has been published online in the *Journal of Raman Spectroscopy* **2012**; *43*, 928. The conclusions reached from the results obtained in each of Chapters 4, 5 and 6 are given in Chapter 7. The instruments and techniques used for this study are described in Chapter 3 and an outline of the theory of Raman spectroscopy is given in Chapter 2. The remainder of this chapter reviews the literature relevant to the passive film on iron in alkaline conditions and its localized breakdown in the presence of chloride ions.

## 1.3. LITERATURE REVIEW

### 1.3.1. The nature of the passive film on iron

The literature concerned with the nature and growth of the passive film on iron formed by electrochemical techniques is extensive, but with a few exceptions a broad consensus has emerged from the many studies on iron and a variety of steels. Using a number of techniques, it has emerged that the composition of the passive film is complex and inhomogeneous and, as such, its structure, composition and mechanism of formation have not yet been firmly established. Different models have been proposed [4,19,31,33-37] for the structure and composition of the passive film which describe either a Crystalline Oxide structure, a Hydrated Polymeric Oxide structure or a Two-layer model.

In the Crystalline Oxide model the protective nature of the layer formed on the metal surface by oxidation is connected to the crystal structure of the film and is either a duplex layer consisting of $Fe_3O_4$ and $\gamma$-$Fe_2O_3$ [34], or $\gamma$-$Fe_2O_3$ alone or an intermediate $Fe_3O_4$/$\gamma$-$Fe_2O_3$ cubic oxide structure [4,19,35,36].

In the Hydrated Polymeric Oxide model the film is considered to be an amorphous, hydrated polymeric layered structure of $Fe(OH)_2$ [4,32,37], bound with water molecules in such a way as to hinder diffusion of $Fe^{2+}$ ions from the metal base to hydration sites at the oxide/solution interface.

There appears to be more agreement on a Two-layer model [10,21,22,39-42] in which the passive film is considered to comprise a continuous inner layer with a spinel structure, composed of a cubic oxide which adheres to the metal surface, being magnetite ($Fe_3O_4$) [10,21,40,41] maghemite ($\gamma$-$Fe_2O_3$) [39,44], a Fe(II)/FeIII)

oxide [42] or an intermediate composite of $Fe_3O_4/\gamma$-$Fe_2O_3$ [4,21,45] and an outer layer that is more loosely bound and composed of $Fe(OH)_2$ [36], FeOOH [2,8,21,39,40,46], hydrated Fe(III) hydroxide [42], $Fe_2O_3.H_2O$ [21], $Fe(OH)_2$ [45,47], hydrated FeOOH (α-, β-, δ- or γ-forms)[4,25], γ –FeOOH [18,30,39], hydrated amorphous or polymeric oxide [30,32,48-51], hydrated $Fe_2O_3$ [2] or a $Fe(OH)_2/\ \gamma$-$Fe_2O_3$ [41]. It has been proposed [2] that the growth of the outer film is made possible by the good electronic conduction of an inner $Fe_3O_4$ layer by the exchange of electrons between the $Fe^{2+}$ and $Fe^{3+}$ ions in the cubic $Fe^{2+}/Fe^{3+}$ lattice. The inner layer grows inwards toward the bulk metal but is kept at a finite thickness by further outward oxidation, which proceeds by two $Fe^{3+}$ associating with the O atom of three $OH^-$ ions while the H parts join with three other $OH^-$ ions to form water [2]. The composition of the inner layer has been further investigated by X-ray diffraction [35] in which a new phase was identified with a spinel structure related to $Fe_3O_4$ and γ-$Fe_2O_3$, more closely resembling $Fe_3O_4$ but with notable differences in the octahedral, tetrahedral and interstitial sites.

In a detailed ellipsometric measurement of iron in 0.05M NaOH [21] it was concluded that the passive film consists of an inner compact layer with a density close to that expected for $Fe_3O_4$, with progressive build-up of a lower density outer layer made up of partially dissolved oxidation products which were oxidized and reduced on each cycle and with a refractive index less than that of a solid phase oxide film [21]. In a separate ellipsometry study of the kinetics and mechanism of passive film formation in 0.05M NaOH [25] the index of refraction of the outer layer was found to be complex but to correspond most closely with that of FeOOH.

Various iron oxide compounds have been reported to be present in the passive film on the surface of iron from a number of different techniques, such as Raman [10-12,18,34,54], X-Ray Photo-electron Spectroscopy (XPS) [55], Mössbauer [31], ellipsometry [21,26,30,56] and Secondary Ion Mass Spectrometry (SIMS) [30,56] studies. These include hematite (α-$Fe_2O_3$), maghemite (γ-$Fe_2O_3$), magnetite ($Fe_3O_4$), goethite (α-FeOOH), akaganeite (β-FeOOH), lepidocrocite (γ-FeOOH) and feroxyhyte (δ-FeOOH). However, as will be discussed in more detail in Section 1.3.5, differences in the number and type of these iron oxide compounds were observed in these studies.

### 1.3.2. Models for the mechanism of pit initiation

Different pitting behaviour is exhibited by different metals and for each of these metals the pitting process varies with electrolyte, alloy composition and temperature [1]. In general, pit growth proceeds by local acidification due to agglomeration of aggressive anions at imperfect sites in the metal, as described in the previous section; however, it is not fully understood how the different factors contribute to the initiation of pits. Many different mechanisms and often conflicting models have been proposed for the initiation and formation of pits and in some cases the models applicable depend on the model chosen for the passive film. Some of these models are more statistical in nature and relate to the potential of the passive film and to the potential gradient in the film while others are associated with transport by cation and anion vacancies in the passive film [1,6]. The leading models are considered to be [6,48] the Adsorption-Displacement models [6,58-61], Flaw or Pore models [62,63], Ion exchange models [3,6,20,64-68], Chemico-mechanical models [69-71], the Point Defect model [72,73], the Local Acidification theory [9] and the Hydrated Polymeric Oxide model [32,39,45,74].

The Adsorption-Displacement models [6,58-61] propose that competitive adsorption of $Cl^-$ ions and O occurs on the surface in the events leading to the formation of pits; these will develop at sites where the adsorbed O is displaced by $Cl^-$ ions which then form soluble complexes with the surface $Fe^{2+}$, resulting in local thinning and a stronger local anodic field at these sites. This would cause more $Fe^{2+}$ to diffuse preferentially to these surface sites where they would complex with $Cl^-$ ions and dissolve.

The Flaw or Pore models [62,63] propose that $Cl^-$ ions pass through pores or flaws in the porous passive film toward the iron lattice where they form complexes which then diffuse back out to the film/solution interface, resulting in formation of pits at the bottom of the pores.

According to the Ion Exchange models [3,6,20,63-68] $Cl^-$ ions permeate through the protective oxide film across the film/solution interface under the influence of the electrostatic field, assisted by bound water; they enter the surface via cation vacancies or by ion exchange of two chloride ions for lattice $O^{2-}$ at sites where the metal-O bond is weakest. The migration of $Cl^-$ ions creates anion vacancies and the $Cl^-$ ions could exchange with $O^{2-}$ and $OH^-$ [67]. The $Cl^-$ ions that displace $O^{2-}$

from inside the oxide surface agglomerate, and then lead to pit formation by local acidification.

In the Chemico-mechanical models [69-71] pits are initiated at ruptures or flaws in the passive film arising from electrostriction pressure effects or repulsive forces between adsorbed ions which effectively lower the interfacial tension at the film/solution interface.

In the Point Defect model, [72,73] cation diffusion occurs from the metal/film to the film/solution interface, eventually resulting in formation of voids at the metal/film interface which disappear into the bulk metal. When the cation diffusion is greater than the disappearance of voids due to an increase in chloride concentration and increased potential difference across the film, breakdown due to void formation increases at the metal/film interface, and this leads to a local collapse of the film, resulting in pit growth.

According to the Local Acidification theory [9], the main reason for passivity breakdown at the initial stages of pit growth is localized acidification due to metal ions hydrolysis. Pits develop at micro pits already on surface because hydrolysis of corrosion products occurs at these sites causing acidification. The corrosion products are transported by diffusion. A low pH of the pit solution is one of the critical factors in maintaining pit growth.

In the Hydrated Polymeric Oxide model [32,39,45,74] bound water molecules are responsible for the protective properties of the passive film and localized breakdown of the passive film occurs at sites where chloride ions displace the water molecules, forming soluble chloride-containing iron complexes which diffuse outward to the solution.

The number of different models described in more detail in Appendix 1, suggests that different mechanisms of pit initiation may be occurring under different conditions [75]. However, even for the same metals under similar conditions there appears to be no complete agreement on the causes and mechanism of pit initiation and growth. The localized breakdown of the passive film formed specifically on iron under the influence of aggressive anions has been extensively studied under a variety of different conditions, and the literature on this has been reviewed by a number of authors [6,48,65,76-78]. A universal theory of the mechanism of pit initiation and growth of the passive film on iron in the presence of aggressive anions is probably not feasible. Even so, it is possible to

draw some broadly applicable conclusions from the different studies. It is generally accepted that aggressive anions agglomerate more readily at defective sites than elsewhere and that the localized adsorption of these anions at imperfections on the surface is considered to be the first step in pitting [6]. The facilitated release of cations and migration of anions at these defective sites induces the formation of an aggressive environment resulting from hydrolysis. At the same time, formation of insoluble iron oxide compounds enable repair of the film and it is also generally agreed that a dynamic equilibrium occurs between localized breakdown and re-passivation of the passive film. When either a critical acidity or aggressive anion concentration is reached which would hinder re-passivation, the equilibrium is shifted in favour of the localized breakdown and stable pits can form. These conditions can be achieved by application of a high enough anodic potential and by addition of aggressive ions to the electrolyte.

After continued attack, pit growth is able to occur unhindered to form a stable pit and the time needed to reach this stage is referred to as the induction time. Stable pitting occurs only at a potential more positive than a critical value referred to as the pitting potential, *Ep* or *Ec*. This potential has been found from potentiodynamic polarization experiments to depend on the electrochemical environment, such as aggressive anion concentration, temperature, electrolyte pH, availability of dissolved oxygen, film thickness, surface roughness and presence of defects and the square root of the sweep rate of the applied potential [1,6,75].

The special ability of chloride ions to hinder re-passivation is due to their ability to form complexes with cations and hydroxides, to increase the activity of $H^+$ in the pit electrolyte, to form a salt layer on the pit bottom at low pH and to decrease the film/electrolyte interface energy [6]. Results arising from the technique of Scanning Combination Ion-selective Microelectrodes (SCIM) in studying the distribution of $Cl^-$ ions during pitting corrosion on stainless steel [7] showed a non-uniform distribution of $Cl^-$ ions on the surface, and a higher chloride concentration at pitting areas, confirming that localized chloride concentration inside corroded pits plays a major role in maintaining pit growth by suppressing the re-passivation of the pits. From SIMS studies [48] it was shown that $Cl^-$ ions were incorporated in the passive film at maximum levels close to the surface, at a depth of around 3 Å. From an electrochemical study of the pitting of iron by $Cl^-$ ions in borate buffer solution [21] changes were observed to occur in the behaviour

of the surface during passivation associated with some variation in the composition and structure of the passive film. It was proposed that iron is most vulnerable to pitting at a critical stage in the development of the passive film associated with a particular composition of the oxide. It was suggested that initially the passive film probably consists of FeOOH which incorporates large amount of water, which decreases continuously as the passivation progresses. In a separate ellipsometry study [25] it was also found that a large amount of water was incorporated during the initial low density stage of passive film formation, which decreased continuously as the passivation progressed and eventually consolidates into FeOOH. It was also found in the same study that in the presence of $Cl^-$ ions structural changes occurred on the surface around the critical pitting potential. It was proposed that pitting occurs through interaction of the $Cl^-$ ions with bound $H_2O$ molecules on the surface. From this ellipsometric study it is evident that water plays a significant role in the protective properties of the passive film on iron, and other studies have also highlighted the role of water in the passive film. Accordingly a separate section follows to review them.

### 1.3.3. The role of water in pitting of the passive film on iron

Numerous studies of both Fe and stainless steels in aqueous solutions of pH 8-14 have agreed on the presence of increased water in the surface film in the passive region [20,25,28-33,48,50,68,70,74] while the amount incorporated appears to increase with increasing pH [27]. However, there appear to be some differences of opinion on the role of the incorporated water in the film. In the ellipsometric study mentioned in the previous section of iron in 0.05M NaOH with added $Cl^-$ ions [25], it was suggested that the water incorporated in the film contributed to pitting by facilitating the migration of chloride ions via water paths in the film. The surface was suggested to consist of FeOOH incorporating a large amount of water which decreased continuously as the passivation progresses, and it was proposed that the film resisted pitting at a particular stage in the formation of the film when the water content was sufficiently reduced. It was observed that compact FeOOH can be destroyed by $Cl^-$ ions if it contains incorporated water and it was proposed that through water paths in the film, $Fe^{3+}$ migrate to the film/electrolyte interface while $Cl^-$ ions move in the opposite direction and react with $Fe^{3+}$, followed by

hydrolysis and resulting in a decreased pH and pitting [25]. It was, however, pointed out that the presence of water alone is not a sufficient condition for pitting, because pitting does not occur at potentials less than the pitting potential even though water is also present in the film at this stage. It was suggested that the reason for this was that the pH produced within water paths in the film was not low enough at potentials below *Ep* because the concentration of $Cl^-$ ions adsorbed in the film surface was not high enough and/or their migration was too slow [25].

In XPS, SIMS and ISS (Ion Scattering Spectroscopy) studies [48] it was found that when $Cl^-$ ions caused breakdown, the $O_{total}$/Fe changed from 2 to 1.5 and the $H_2O$/Fe changed from 0.5 to 0.1. Dehydration by heating resulted in $Cl^-$ ions penetrating the whole film thickness, showing that water plays an essential role in transforming the properties of iron oxide to those of a protective passive layer: it was suggested that water stops $Fe^{3+}$ from diffusing from the metal base to hydration sites at the oxide/solution interface by keeping the film amorphous. The XPS studies also showed that $Cl^-$ ions can remove water in a process of de-passivation.

In a separate study differences were observed in Raman spectra of the passive film recorded *in situ* in solution and *ex situ* after drying, which reflect the effect of water on the structure of the passive film [47]. Water in the film was found to result in an increase in the Fe-O distance, suggesting that the H atoms introduced can lead to increased structural flexibility by forming M-OH bonds in addition to M-O bonds which would promote a more glass-like structure for the film.

A reflectivity study [80] revealed that the higher refractive index corresponding with higher anodic potentials is due to dehydration of the film which is induced by the high anodic electric field:

$$Fe(OH)_3 \rightarrow FeOOH + H^+ + OH^-$$

$$2FeOOH \rightarrow Fe_2O_3 + H^+ + OH^-.$$

Mössbauer studies [31,43,51] showed that the passive film has an amorphous character which is due of incorporation of water. The O:Fe ratio was found to be close to 2 when film is passive, but dropped to 1.5 when the film was made non-passive by heating or by addition of $Cl^-$ ions. It was suggested that passivity was associated with amorphous $Fe_2O_3.H_2O$ and the non-passive form with $Fe_2O_3$ or

$Fe_3O_4$. It was proposed that $Cl^-$ ions remove water and thus destroy the passivity by removing its amorphous character.

In a kinetic study of the localized corrosion of stainless steel in the presence of $Cl^-$ ions [81], two reactions were described to occur simultaneously with metal ions which have moved from the bulk metal through the oxide film to the film/solution phase boundary and the electrolyte:

$$M + pCl^- \rightarrow MCl_p^{2-p} + 2e^-$$

$$nM + mH_2O \rightarrow M_nO_m + 2mH^+ + 2me^-$$

while at the same time dissolution of oxide occurs:

$$M_nO_m + 2mH^+ + npCl^- \rightarrow MCl_p^{2(m/n)-p} + mH_2O$$

It was suggested that as long as the second and third reactions occur at the same rate, the thickness of the oxide film does not change and the metal dissolution in the pits proceeds at constant rate. If the second reaction occurs at a faster rate than the third, the oxide film grows more quickly than it dissolves allowing the surface to re-passivate; this would be encouraged by a higher water concentration and insufficient chloride. It follows that reduced amounts of water and an increased chloride concentration would therefore lead to faster localized dissolution, resulting in the growth of stable pits.

### 1.3.4. Green Rusts

Considerable attention has been given to the presence of Green Rust which forms on iron surfaces in aqueous and alkaline solutions [45,52,80-92] in the presence of anions such as chlorides, sulphates, halides, phosphates, carbonates and nitrates [82]. Green Rusts are dark green gelatinous precipitates formed as intermediate aqueous complexes from the solid state oxidation of $Fe(OH)_2$ [88] and are temporarily stabilized by the presence of the anions, but eventually further oxidize to $Fe_3O_4$, $\gamma$-$Fe_2O_3$ or FeOOH compounds depending on the temperature, rate of oxidation and ratio of concentration of anion to $OH^-$ [45,80,84,89]. They form layered Fe(II)-Fe(III) hydroxide compounds belonging to the hydro-talcite mineral group, with positively charged brucite-like layers separated by inter-layers of anions and water molecules [49] and their composition and stoichiometry depend on the environment and on the nature of the anions in solution [82]. Two types of Green Rust have been characterized depending on the nature of the

anions [52,82,93]; rhombohedral Green Rust I which forms in the presence of chloride, sulphate and bromine ions, and hexagonal Green Rust II which forms only in the presence of sulphate ions by decomposition of Green Rust I [82,93]. Various compositions for Green Rust I have been given: $2Fe(OH)_2.Fe(OH)Cl.Fe(OH)_2Cl$ [94], $3Fe(OH)_2.Fe(OH)_2Cl.nH_2O$ [81], $([Fe^{II}_2Fe^{III}O_x(OH)_y]Cl_{(7-2x-y)})$ [52], $Fe^{III}_2Fe^{II}_4(OH)_{12}Cl_2$ [86,95,96] or varying between $Fe^{II}_3Fe^{III}(OH)_8Cl.nH_2O$ and $Fe^{II}_{2.2}Fe^{III}(OH)_{6.4}Cl.nH_2O$ with *n* probably equal to 2 [88].

The $Fe^{III}/Fe^{II}$ ratio increases continuously upon aerial oxidation and converts to $Fe_3O_4$ in the case of slow oxidation by air [45,52], or to γ-FeOOH in the case of rapid oxidation [52]. Green Rust II has been reported as $4Fe(OH)_2.FeOOH.FeSO_4.nH_2O$ [82], $[Fe^{II}_4Fe^{III}_2(OH)_{12}]^{2+}[SO_4.mH_2O]^{2-}$ [83], or $4Fe(OH)_2.2FeOOH.FeSO_4.nH_2O$ with *n* probably equal to 4 [96]. Green Rust II transforms to γ-FeOOH [52,85,86].

From a Mössbauer study [84] it was found that different ferrous hydroxide compounds are involved in the formation of Green Rust depending on the ratio of $[Cl^-]/[OH^-]$. For $[Cl^-]/[OH^-] \leq 1$, ferrous hydroxide I ($Fe(OH)_2$) forms which transforms into α-FeOOH and $Fe_3O_4$, and for $[Cl^-]/[OH^-] \geq 1$, ferrous hydroxide II ($2Fe(OH)_2$,FeOHCl) forms which transforms to Green rust I, which in turn transforms into γ-FeOOH, with parallel formation of α-FeOOH and $Fe_3O_4$. For $[Cl^-]/[OH^-] \geq 4$, β-FeOOH is predominantly formed.

In a separate XRD study [89] it was found that for $[Cl^-]/[OH^-] > 1.75$, γ-FeOOH, α-FeOOH and β-FeOOH were formed, and for $[Cl^-]/[OH^-]$ between 1.025 and 1.11 a hydrated magnetite of the form $Fe(OH)_2.2FeOOH$ forms which leads to a non-stoichiometric magnetite, $Fe_{3-x}O_4$. For $[Cl^-]/[OH^-]$ between 1 and 1.205 it was found that formation of hydrated magnetite occurred from hydrated ferrous hydroxide without formation of Green Rust [89].

### 1.3.5. Raman spectroscopic studies of the passive film on iron

Raman micro-spectroscopy is a preferred method in principle, not only because it is non-destructive and can be carried out *in situ* during electrochemical control of the iron surface, but also because it measures molecular vibrations and thus gives specific information on the composition of the film. *In situ* Raman

micro-spectroscopy studies have been carried out in the past of the passive oxide film grown with electrochemical control in alkaline pH-controlled 0.05 M – 1 M NaOH or KOH [10-12,18,40] or borate buffer solutions [11-17,19,40,54,94,97-99]. However, a selection of these results, presented below in chronological order, although showing the feasibility of the method, provide results that differ significantly. In an early Raman study of iron in 1M NaOH, $Fe_3O_4$ was detected over a wide range of potentials, and γ-$Fe_2O_3$ and α-FeOOH at certain potentials [10]. In an *in situ* investigation of iron in 0.05M NaOH two layers were proposed, in which $Fe_3O_4$ formed the primary layer and was covered by a loosely bound outer layer of other products such as α-FeOOH, δ-FeOOH, $Fe(OH)_3$ and γ-$Fe_2O_3$ [41]. However, in a separate study only $Fe_3O_4$ [93] was detected. In a recent Raman study [101] $Fe_3O_4$ was detected at all potentials in anodic and cathodic scans and α-FeOOH at certain potentials. It was concluded that the passive film was based on $Fe_3O_4$ and formed a 3-D structure, with the inner part remaining $Fe_3O_4$ - like at all potentials while the outer part was oxidized and reduced depending on the electrode potential.

Using EQCM (Electrochemical Quartz Crystal Microbalance), ellipsometry, STM (Scanning Tunnelling Microscopy) and RS (Raman Spectroscopy) [53] the anodic formation of the passive film on iron in neutral borate solution was investigated and the film was found to consist of an inner layer based on $Fe_3O_4$ and outer layer of FeOOH which may be oxidized and reduced.

In a RS study of Fe at pH 12.7 in presence of $Cl^-$ ions, (0.05M + 0.03M NaCl) [18] it was reported that the inner layer was $Fe_3O_4$ and the outer layer which covered the surface and which converted to γ-FeOOH in air was attributed to Green Rust.

Surface Enhanced Raman Spectroscopy (SERS) has been used to effectively increase the band intensities of the iron oxides [13-16,19,41,54,97,102]. Of relevance is a SERS Raman study [97] of AISI 316 stainless steel in an alkaline electrolyte (pH 9) containing $Cl^-$ ions. The iron oxide compounds detected were $Fe_3O_4$, $Fe(OH)_2$ and possibly FeOOH; however, it was not possible to distinguish the FeOOH forms, if present, from one another and from the $Fe_3O_4$.

*In situ* Raman investigations of iron corrosion in air saturated water at a pressure of 25.1 MPa and temperatures from 21 to 573$^o$C have been carried out [103], and upon heating, various combinations of $Fe_3O_4$, α-$Fe_2O_3$, γ-FeOOH, and γ-

$Fe_2O_3$ were detected depending on the location or temperature of the iron sample. On cooling the sample and also with subsequent *ex situ* measurements, the studies identified a two layered structure with an inner corrosion layer consisting of $Fe_3O_4$ and $\alpha$-$Fe_2O_3$, and an outer layer consisting of $\gamma$-$Fe_2O_3$ and $\alpha$-$Fe_2O_3$. SERS, *in situ* Raman and SEM studies of the passive film on iron in water with variable, low $O_2$ concentrations at 288$^oC$ [100] inferred a two layer composition for the film, with faceted particles of $Fe_3O_4$ making up the outer layer and an inner conformal layer of $Fe_3O_4$ forming the inner layer. In another SERS *in situ* study of the surface of iron conducted after many polarization cycles in 1M NaOH [95] it was concluded that the passive layer consisted of an inner layer of $Fe_3O_4$ and an outer layer of either $\alpha$-FeOOH or $\beta$-FeOOH and $\delta$- FeOOH. It needs to be mentioned that *ex situ* studies of the passive layer in 5M KOH by Mössbauer spectroscopy [104] detected the compound $\beta$-FeOOH that was not conclusively found in any of the Raman studies.

All of these studies, while demonstrating the potential of the technique, were not hugely successful in establishing the composition of the passive film. While this has been partly due to the studies being conducted under different experimental conditions which affect the composition, such as pH and electrochemical control parameters, the technique has been limited by very weak Raman spectra resulting from the use of the conventionally used $Ar^+$ ion laser line at 514.5 nm, which provides excitation conditions far from resonance for the iron oxide and oxy-hydroxide compounds under study. In many of these studies repeated oxidation and reduction polarization cycles were performed in an attempt to thicken the layer to improve the spectral intensity. However, detailed potentiostatic studies [23,24] of the passivation of carbon steel in 1 M NaOH have shown that the passive film growth is a complex process and that a number of different mechanisms may be operative at different potentials. It has also been found that the surface changes during increasing number of oxidation and reduction cycles [21] with significant changes in the growth mechanisms occurring over relatively small changes in potential, while the oxidation processes in the film depend to a large extent on what oxides were formed previously [14].

This complexity may account for the different interpretations for the composition of the passive layer reported from the *in situ* Raman spectroscopic

studies, since some of the strongest Raman bands of the different iron oxides and iron oxyhydroxides occur near the same frequency, increasing their assignment uncertainty in the case of weak spectra. For example, $Fe_3O_4$, $\gamma$-$Fe_2O_3$ and the $\alpha$-, $\gamma$- and $\delta$- forms of FeOOH all have bands around 670 $cm^{-1}$ so it has been difficult to distinguish them from one another [18,97].

# CHAPTER 2

# OUTLINE OF THE THEORY OF RAMAN SPECTROSCOPY

## 2.1. INTRODUCTION

The Raman effect concerns the inelastic scattering of electromagnetic radiation (i.e. an incident light beam) incident on matter (solid, liquid or gas). The theory of Raman scattering has been described in an extensive body of literature and a brief discussion is presented here. Most of the scattered light is emitted at the same frequency as the incident light and is thus scattered elastically; this is referred to as Rayleigh scattered light. However, a tiny fraction of the incident light is scattered at a lower frequency than the Rayleigh frequency (Stokes scattering) or a higher frequency (anti-Stokes scattering), these frequency shifts being of the same magnitude. This inelestically scattered light constitutes the Raman effect. Raman scattering may be described in more detail in terms of classical radiation theory [105,106,107] and quantum theory [104,107,108]. Both approaches are considered below.

The present discussion will consider Raman scattering resulting from the vibrations of molecules, this being relevant to the present work and will also include a description of the effects of pre-resonance enhancement.

## 2.2. RAMAN AND RAYLEIGH SCATTERING IN TERMS OF CLASSICAL RADIATION THEORY

The classical theory is based on the concept that the scattered light is created by oscillating electric dipoles induced by the electric field of the exciting light. The treatment closely follows that in reference 108. The induced electric dipole moment vector $\boldsymbol{\mu}$ is linearly related to the electric field vector $\boldsymbol{E}$ for normally encountered electric field strengths in Raman spectroscopy and hence

$$\boldsymbol{\mu} = \alpha \boldsymbol{E}$$

where $\alpha$ is the polarizabilty, being a measure of the ease with which the electrons are displaced under the influence of an electric field.

This relation can be written in the form of three linear equations,

$$\mu_x = \alpha_{xx}E_x + \alpha_{xy}E_y + \alpha_{xz}E_z$$
$$\mu_y = \alpha_{yx}E_x + \alpha_{yy}E_y + \alpha_{yz}E_z$$
$$\mu_z = \alpha_{zx}E_x + \alpha_{zy}E_y + \alpha_{zz}E_z$$

and in the corresponding matrix form as

$$\begin{bmatrix} \mu_x \\ \mu_y \\ \mu_z \end{bmatrix} = \begin{bmatrix} \alpha_{xx} & \alpha_{xy} & \alpha_{xz} \\ \alpha_{yx} & \alpha_{yy} & \alpha_{yz} \\ \alpha_{zx} & \alpha_{zy} & \alpha_{zz} \end{bmatrix} \begin{bmatrix} E_x \\ E_y \\ E_z \end{bmatrix}$$

where the nine coefficients $\alpha_{ij}$ are the components of the polarizability tensor $\boldsymbol{\alpha}$ expressed in matrix form.

The polarizability tensor may be modulated by the normal vibrational coordinates of the molecule. This relationship can be expressed as a Taylor series with respect to these coordinates:

$$\alpha_{ij} = \left(\alpha_{ij}\right)_0 + \sum_k \left(\frac{\partial \alpha_{ij}}{\partial Q_k}\right)_0 Q_k + \frac{1}{2}\sum_{k,l}\left(\frac{\partial^2 \alpha_{ij}}{\partial Q_k \partial Q_l}\right)_0 Q_k Q_l + \cdots\cdots$$

where $\alpha_{ij}$ is a component of the polarizability tensor, with $\left(\alpha_{ij}\right)_0$ being its value at the equilibrium configuration; $Q_k$ is the *k*th normal coordinate associated with the vibration of frequency $\nu_k$; the subscript zeros refer to derivatives taken at the equilibrium configuration. A further simplification is adopted by neglecting the higher order terms and treating the normal vibrations as being harmonic. These simplifications result in the linear dependence of the polarizability on each vibrational coordinate:

$$\boldsymbol{\alpha}_k = \boldsymbol{\alpha}_0 + \left(\frac{\partial \alpha}{\partial Q_k}\right)_0 Q_k \quad \text{and} \quad Q_k = Q_{k_0} \cos 2\pi \nu_k t$$

where $\nu_k$ is the frequency and $Q_{k_0}$ is the amplitude corresponding to the *k*th normal mode of vibration.

The harmonic variation of the electric field intensity of the incident radiation, *E*, oscillating at frequency $\nu_0$, is given by:

$$\boldsymbol{E} = \boldsymbol{E}_0 \cos 2\pi \nu_0 t$$

where $\boldsymbol{E}_0$ is the field amplitude and *t* is the time.

Inserting the above equations for $\boldsymbol{\alpha}_k$, $Q_k$ and $\boldsymbol{E}$ into the equation $\boldsymbol{\mu} = \boldsymbol{\alpha}\boldsymbol{E}$, gives for the $k$th normal mode of vibration,

$$\boldsymbol{\mu} = \boldsymbol{\alpha}_0 \boldsymbol{E}_0 \cos 2\pi\nu_0 t + \left(\frac{\partial\alpha}{\partial Q_k}\right)_0 Q_{k_0} \boldsymbol{E}_0 \cos\left(2\pi\nu_0 t\right)\cos\left(2\pi\nu_k t\right).$$

Using a trigonometric transformation, it follows that

$$\boldsymbol{\mu} = \boldsymbol{\alpha}_0 \boldsymbol{E}_0 \cos 2\pi\nu_0 t + \frac{1}{2}\left(\frac{\partial\alpha}{\partial Q_k}\right)_0 Q_{k_0} \boldsymbol{E}_0 \left[\cos 2\pi\left(\nu_0 - \nu_k\right)t + \cos 2\pi\left(\nu_0 + \nu_k\right)t\right]$$

The induced dipole generates radiation at three different frequencies, associated with the three cosine functions having different arguments. The first term describes Raleigh scattering at frequency $\nu_0$, whereas the second and third account for Stokes Raman and anti-Stokes scattering at $\nu_0 - \nu_k$ and $\nu_0 + \nu_k$, respectively.

The intensity of Rayleigh scattering depends on $\boldsymbol{\alpha}_0$, being the polarizability of the molecule at the equilibrium nuclear configuration. The intensity of Stokes and anti-Stokes Raman scattering depends on the derived polarizability tensor

$$\boldsymbol{\alpha}'_k = \left(\partial\alpha / \partial Q_k\right)_0 .$$

Thus those normal vibrations for which all derived polarizability tensor components are zero, are inactive in Raman scattering. For normal modes resulting in Raman scattering, at least one derived polarizability tensor component must differ from zero, i.e.

$$\left(\alpha'_{ij}\right)_k = \left(\frac{\partial\alpha}{\partial Q_k}\right)_0 \neq 0 .$$

## 2.3. RAMAN AND RAYLEIGH SCATTERING IN TERMS OF QUANTUM THEORY

In quantum mechanical terms, the energy state of the molecule is perturbed by the oscillating dipole of the incident electric field, $E_0$, and passes from an initial vibronic energy state, $m$, into a final vibronic state, $n$, via a short-lived (~$10^{-14}$ s) virtual energy state while emitting Raman scattered light of frequency $\nu_0 \pm \nu_{mn}$, where $\nu_{mn} = \nu_m - \nu_n$. The transitions between the energy levels giving

rise to Raman scattering are represented by solid arrows in Figure 2.1, with $v_0 + v_{mn}$ and $v_0 - v_{mn}$ representing the anti-Stokes (A) and Stokes (S) frequencies, respectively, in the Normal Raman (a) and Resonance Raman (b) effects. The transitions that do not result in any change in energy ($v_{mn} = 0$) are represented by dotted lines and give rise to Rayleigh scattering. The symbols *m* and *n* represent initial and final vibrational energy levels in the electronic ground state, while *g* and *e* in Figure 2.1 are the ground and excited electronic states, respectively. The red dashed lines indicate virtual energy states.

.

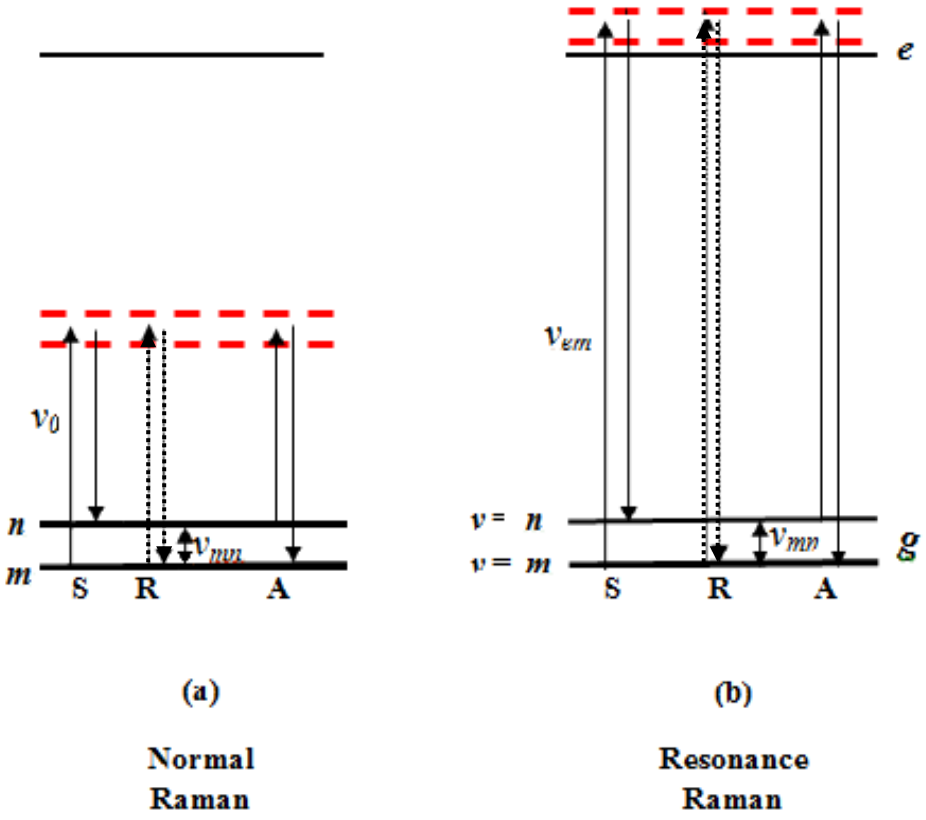


Figure 2.1. Energy level diagram showing Stokes (*S*) and anti-Stokes (*A*) transitions (solid arrows) between initial (*m*) and final (*n*) vibrational energy levels (*v*) in the Normal Raman (a) and Resonance Raman (b) effects. *e* and *g* represent electronic excited and ground states, respectively [109]. The red dashed lines indicate virtual energy states.

According to the quantum mechanical description, and following the treatment in reference 107, the intensity of the Stokes Raman scattered light is given by

$$I_{mn} = \text{constant } I_0(\nu_0 - \nu_{mn})^4 \sum_{p\sigma} \left| \left(\alpha_{\rho\sigma}\right)_{mn} \right|^2 .$$

Here $I_0$ is the intensity of the incident light of frequency $\nu_0$, $m$ and $n$ denote the initial and final states of the electronic ground state g and e (shown in Fig. 2.1) is an electronic excited state involved in Raman scattering. $\left(\alpha_{\rho\sigma}\right)_{mn}$ represents the change in polarizability $\alpha$ as a result of the electronic transitions $m \rightarrow e \rightarrow n$, and $\rho$ and $\sigma$ are $x$, $y$ and $z$ components of the polarizability tensor.

In normal Raman scattering the frequency of the incident light is chosen so that it is much smaller than the frequency of an electronic transition (i.e. $\nu_0 \ll \nu_{em}$) as shown in Figure 2.1(a). In this case the polarizability is independent of the excitation frequency, and the intensity of the Stokes Raman scattered light will be proportional to $(\nu_0 - \nu_{mn})^4$.

As $\nu_0$ approaches $\nu_{em}$, however, the electronic transitions become significant and the term $\left(\alpha_{\rho\sigma}\right)_{mn}$ in the previous equation can be expressed as

$$\left(\alpha_{\rho\sigma}\right)_{mn} = \frac{1}{h} \sum_e \left( \frac{M_{me} M_{en}}{\nu_{em} - \nu_0 + i\Gamma_e} + \frac{M_{me} M_{en}}{\nu_{en} + \nu_0 + i\Gamma_e} \right),$$

where $\nu_{em}$ and $\nu_{en}$ are the frequencies corresponding to the energy differences of the states (as shown in Figure 2.1(b)), $h$ is Planck's constant, $M_{me}$ and $M_{en}$ are electric transition moments, $\Gamma_e$ is the band width of the $e^{\text{th}}$ state and the $i\Gamma_e$ term is the damping constant.

From this equation it can be seen as $\nu_0$ approaches $\nu_{em}$ the denominator of the first term in the brackets diminishes, resulting in an increase in the polarizability and hence the Raman intensity. The enhancement afforded by tuning the excitation frequency $\nu_0$ closer to $\nu_{em}$ is termed pre-resonance enhancement and by appropriate choice of $\nu_0$ this can be exploited to significantly increase the Raman intensity.

When the excitation frequency is very near to or coincides with one of the electronic transitions of the molecule (as in the case of $\nu_0 = \nu_{em}$) a condition of resonance is achieved resulting in an enormous increase in the intensity of the Raman band at $\nu_0 - \nu_{mn}$ and is termed Resonance Raman scattering. In this condition the vibrational modes associated with the particular electronic transition are selectively enhanced and usually overwhelm the Raman signals from all of the other vibrational modes.

As the excitation line is tuned toward the frequency of an electronic absorption, it approaches resonance but does not yet coincide with the electronic absorptions. In this condition the intensity of the Raman bands begin to increase and this condition is described as pre-resonance enhancement. There is no clear dividing line between resonance and pre-resonance enhancement and pre-resonance enhancement does not begin at a sharply defined wavelength. Pre-resonance enhancement of five to ten times may be observed if the exciting laser is even within a few hundred wavenumbers below the electronic transition of a molecule [110].

# CHAPTER 3
# INSTRUMENTAL METHODS AND PROCEDURES

## 3.1. INTRODUCTION

The Raman spectra were recorded using a JY T64000 Raman spectrograph using two different excitation wavelengths: the 514.5nm excitation line of the $Ar^+$ laser and the 636.4 nm excitation line of a tuneable dye laser. Descriptions of these instruments and the theory of their operation are given in Section 3.2. The theory of Raman spectroscopy has been summarized in Chapter 2.

Electrochemical control of the iron surface was achieved using a three electrode cell with a potentiostat. A description of these instruments and the theory of the techniques are given in Section 3.3. The data collected from the different instruments was processed using Labspec 3 spectroscopic software and Origin 6.1 software. Multivariate statistical analysis of the Raman spectra was performed using Multivariate Curve Resolution (MCR) using the MCR-ALS least squares optimization toolbox of MATLAB, which is described in Section 3.4.

## 3.2. RAMAN MICRO-SPECTROSCOPY ANALYSIS

The instrumentation used to measure the Raman spectra was a Jobin Yvon T64000 Raman spectrograph with an Olympus BX40 confocal microscope attachment. The excitation radiation was provided by two sources: the 514.5 nm line of a Coherent Innova 308 Argon ion laser and a Spectra-Physics Model 375/376 dye laser system with R6G dye, providing tuneable radiation between 540 and 650 nm and pumped by a Spectra-Physics model 171 Argon ion laser operated in multiline mode. These will be described in more detail in Section 3.2.2. The confocal microscope attachment is described in more detail in Section 3.2.3.

### 3.2.1. Raman spectrograph

The JY T64000 system contains a double subtractive pre-monochromator (Stages 1 and 2) and a single spectrograph (Stage 3) and is able to work in single spectrograph mode (Stage 1 only) or in triple pass configuration (Stages 1 and 2 +

Stage 3). The single spectrograph stage is used as a disperser and is equipped with a two grating-turret: 1800 gr/mm and 600 gr/mm. When used in single spectrograph configuration, the Rayleigh scattered light is removed by using a holographic notch filter appropriate to the excitation radiation.

In triple pass configuration the grating of the spectrograph disperses the polychromatic radiation selected by the pre-monochromator. The pre-monochromator is a twin monochromator working in subtractive mode and serves as a tuneable filter in the chosen spectral range, and is equipped with an 1800 gr/mm grating. The detector used for acquisition of the spectra was a multichannel detector: a Spectrum One Charge Coupled Device (CCD) detector, mounted in the plane of the exit image and cooled by liquid nitrogen to 140 K. The spectral bands are acquired sequentially and each spectral band is measured for a specific grating position. The width of the spectral bands depends on the wavelength and the grating used (600 gr/mm or 1800 gr/mm) and the entrance slit width. The detector resolution is better than 2 pixels of the CCD and is determined by the grating and the entrance slit width. The single spectrograph configuration was selected for the present study because it has the advantage of greater throughput for the very weak intensities of the spectra recorded *in situ*. The grating and entrance slit width used were 600 gr/mm and 200 μm, respectively, which allowed a resolution of 6 $cm^{-1}$.

A photograph of the instrument is shown in Figure 3.1 and a schematic diagram showing the layout of the major components of the JY T64000 Raman spectrograph [111] is given in Figure 3.2.

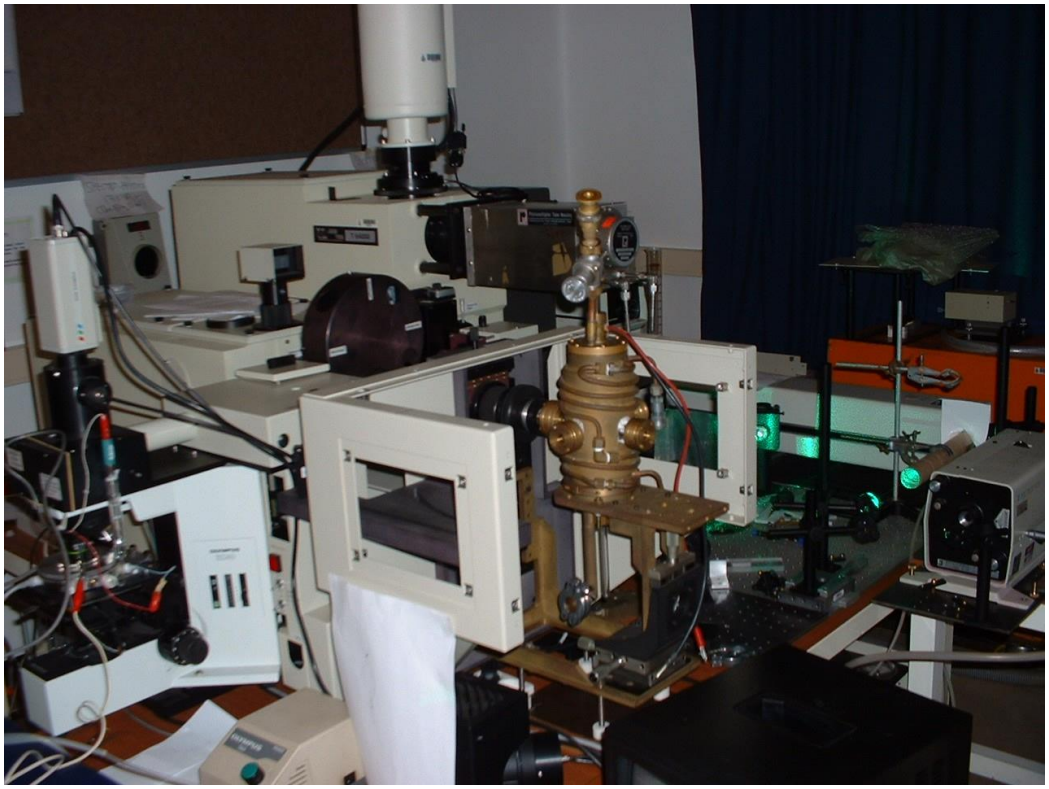

Figure 3.1. Photograph of the JY T64000 Raman Spectrograph and associated equipment used for recording the *in situ* Raman spectra of the Fe surface during electrochemical control by potentiodynamic polarization.

For the experiments used in this study the confocal pinhole diaphragm was 0.1 mm. The samples were analysed using a back-scattering geometry on the microscope stage of the Olympus confocal Raman microscope, using the long working distance 20× objective, with numerical aperture (NA) of 0.4 and focal distance of 12 mm and also the 100x objective, with numerical aperture (NA) of 0.85 and working distance 0.21 mm. For the tuneable dye laser radiation at 636.4 nm, a 632.8 nm holographic notch filter was positioned before the detector entrance to filter out the Rayleigh scattered light, and for the 514 nm $Ar^+$ laser a 514.5 nm holographic notch filter (Kaiser Optics) was used. For both lasers a 514.5 nm interference filter was used to remove the plasma lines from the $Ar^+$ laser.

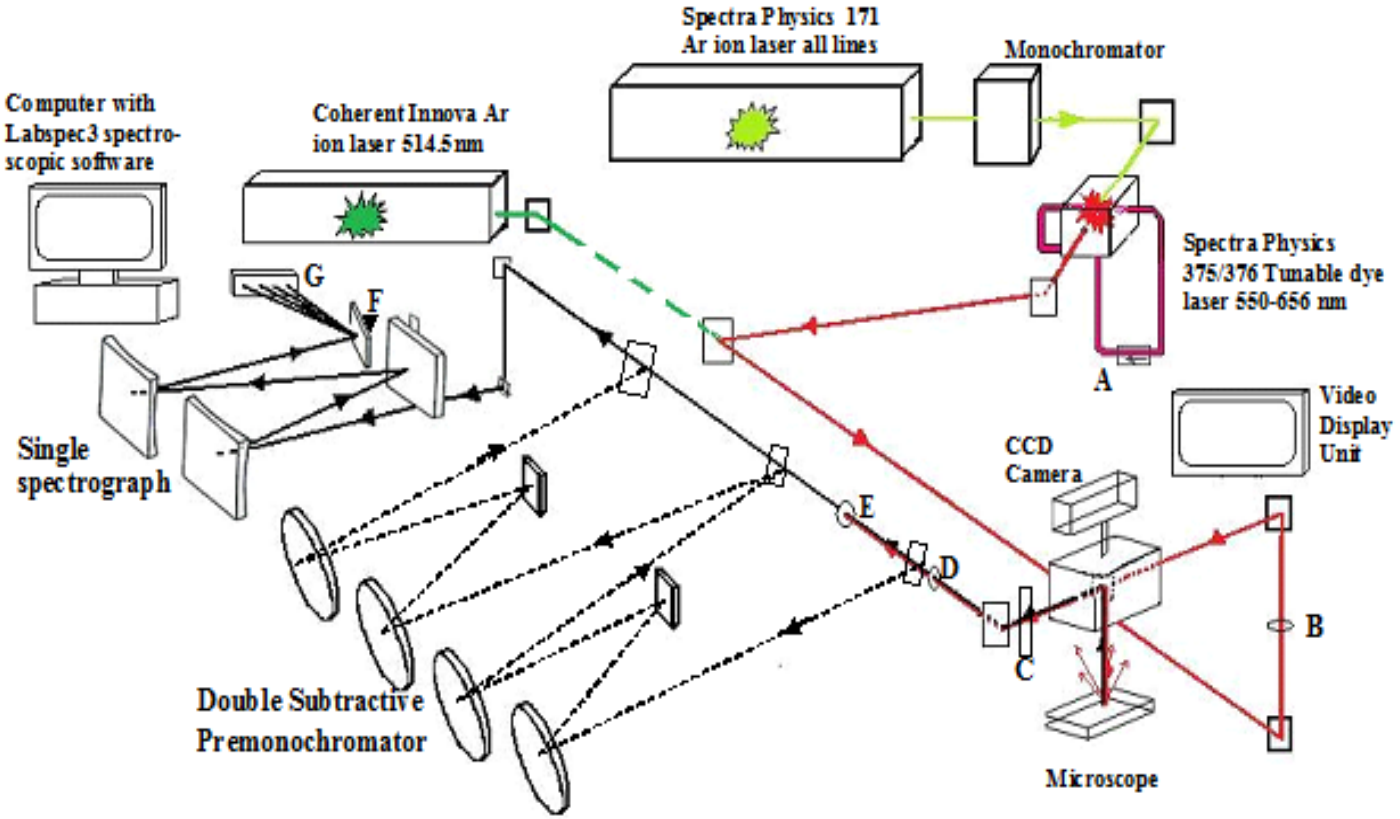


Figure 3.2. Schematic outline of the Jobin Yvon T64000 Raman microscope system [111] showing the major components of the system used (not drawn to scale) and the laser optical path. A = Dye circulation system with pump, B = Interference filter, C = Entrance slit, D = Confocal pinhole diaphragm, E = Holographic Notch filter, F = Holographic diffraction. grating (600g/mm) and G = CCD detector.

### 3.2.2 Confocal microscope

A schematic diagram showing the basic concept of the confocal microscope is given in Figure 3.3. The confocal microscope system enables control of the depth of analysis by controlling the depth of focus.

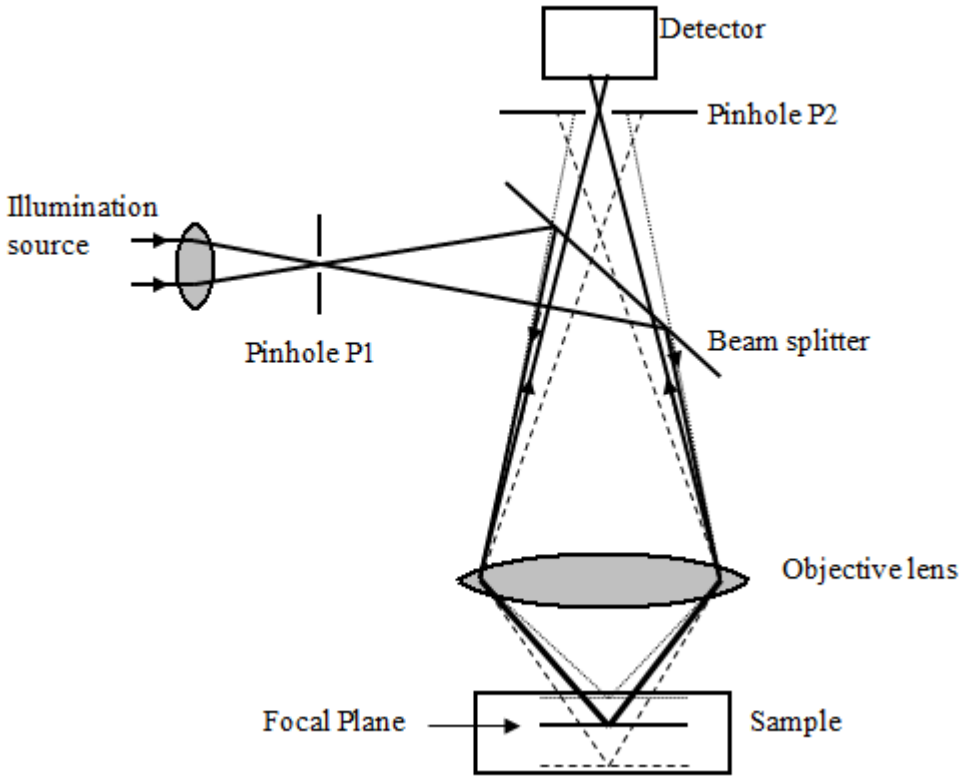


Figure 3.3. Schematic diagram showing the collection optics of the confocal system of a scanning microscope showing the basic principle of confocal microscopy [112] (the solid line represents that part of the light at the focal plane and the dashed and dotted lines represents the light filtered out by confocal pinholes $P_1$ and $P_2$).

The confocal system is defined by a confocal diaphragm which consists of two pinholes, $P_1$ and $P_2$, which are conjugated with the focal point in the object plane. The first pinhole serves to spatially filter the incident laser to remove unwanted rings and produce a cleaner point source; this is imaged onto the sample by the objective at the focal plane. The scattered light is directed to an adjustable pinhole $P_2$ which partially attenuates the beams coming from the upper and lower

planes. By adjusting the $P_2$ diameter one can control the volume of sample collected and hence the location of the region of the sample to be analysed [112].

### 3.2.2. EXCITATION RADIATION

***Argon ion laser***

A schematic diagram showing the basic components of an $Ar^+$ ion gas laser [107] is given in Figure 3.4.

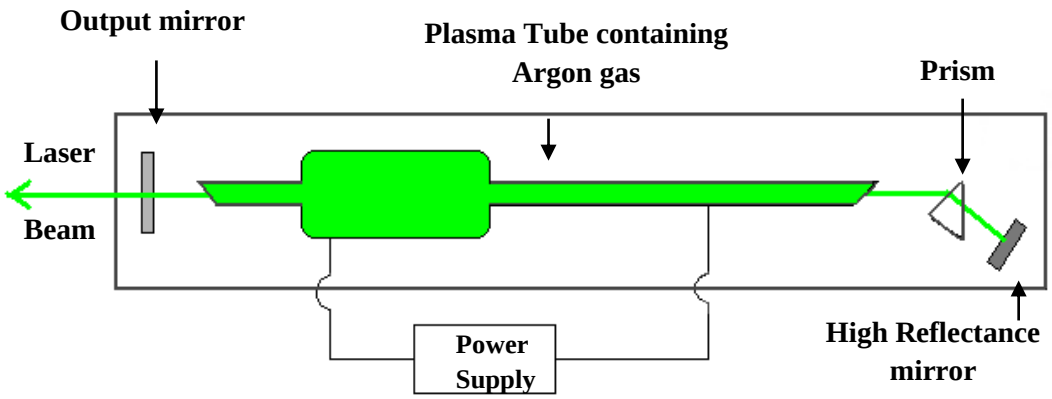


Figure 3.4. Schematic diagram showing the basic components of an $Ar^+$ ion gas laser [107].

The argon gas is contained in the plasma tube which is cooled by a water jacket with continuous flow. The resonant cavity is defined by the two mirrors, a high reflectance mirror and the semi-transparent output mirror at the exit end of the laser. Both mirrors are coated to reflect the light of interest while transmitting all other light. Two quartz Brewster windows seal each end of the tube positioned at an angle $\theta$ such that $\tan \theta = n$, where n is the refractive index of the window material. At Brewster's angle the output beam is almost completely polarized in a fixed direction. A prism is inserted between the mirrors in front of the high reflectance mirror for single line operation and can be removed for multiline operation [113].

To operate the laser, a very high current discharge is passed through the argon gas which ionizes the gas and creates a large collection of $Ar^+$ and $Ar^{2+}$ ions in excited states which undergo transitions to a lower state. On returning to the lower energy states they emit photons at specific wavelengths that depend on the energy difference between the excited state and the lower energy states. There are many lower energy states and hence many emission lines but the two strongest ones from $Ar^+$ ions are at 488 nm and 514.5 nm. They then revert to their ground states by emitting hard UV radiation at 72 nm and are then neutralized by a series of electrodes in the laser cavity [107]. The photons reflect off the mirrors to travel back and forth through the argon gas. The prism in front of the back mirror allows through only photons of a specific wavelength, depending on the angle of position. If a photon possessing a certain wavelength and phase encounters another atom that has an electron in the same excited state, it can stimulate the other atom to emit a photon with the same frequency and phase as the incoming photon. The photons, with a very specific wavelength and phase, reflect off the two mirrors to travel back and forth through the argon gas and in the process they stimulate further emission from other excited state atoms. A cascade effect occurs, producing many photons of equal wavelength, phase and direction, and this process continues until equilibrium is reached between excitation and emission. The semi-transparent output mirror reflects the photons but allows a fraction through, which becomes the output beam of the laser and which is coherent in terms of in terms of wavelength, phase and polarization [113]. If the prism is removed the laser will resonate simultaneously on a number of transitions, (in multiline mode) and this provides the highest output power which is suitable for exciting a dye laser.

***Tuneable dye laser***

A tuneable dye laser was used for the experiments because it can provide a Continuous Wave (CW) laser beam over a broader spectral range than the $Ar^+$ ion laser and also because it enables the excitation wavelength to be tuned continuously to any desired wavelength within a specified range. It thus provided the option of being able to enhance the band intensities by varying the excitation to approach the resonance frequency, and thus produce optimum enhancement of

the Raman bands. The Spectra-Physics Model 375/376 dye laser system was used, which consists of the model 375 dye laser with model 376 circulator, and was pumped by a Spectra-Physics model 171 Argon ion laser operated in multiline mode. Basically, the dye laser optical system comprises a stream of organic dye, which is the gain medium, flowing through a cavity, with various mirrors and tuning elements. A schematic diagram of the optical system for the Spectra-Physics Model 375/376 dye laser is given in Figure 3.5 [114] below:

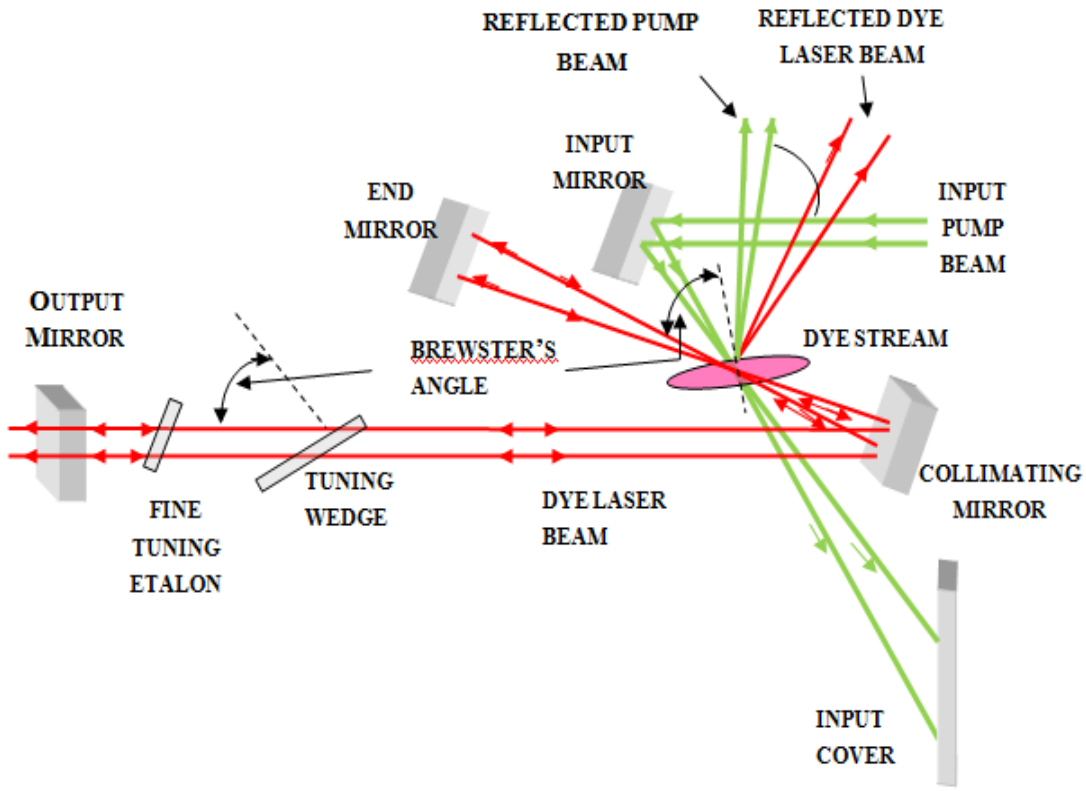


Figure 3.5. Optical system of the Spectra-Physics Model 375/376 dye laser [114]

Rhodamine 6G (R6G) is a large organic molecule which absorbs strongly in the region 480 nm to 530 nm due to $\pi \rightarrow \pi^*$ transitions [113] and provides laser gain from 566 nm to 656 nm. The energy level typical for the R6G dye solution is given in Figure 3.6 [113]. The dye molecules absorb the pump laser radiation to undergo transitions from $S_0$ ($v = 0$) $\rightarrow S_{v'}$ ($v' = 0, 1, 2, 3\ldots$) and these transitions are broad and continuous because each electronic level is accompanied by collisional and rotational broadening by the solvent. The molecules are excited to

various sublevels in $S_1$ and then fall to the ν' = 0 energy state via radiationless transitions, then drop to $S_0$ (ν = 0, 1, 2, 3…) states to emit a broad fluorescent band of radiation at longer wavelengths. The emitted light is passed back and forth through the dye stream by the mirrors which form the optical cavity of the dye laser and the laser action is provided by stimulation of the previously excited dye molecules to emit light at a broad range of fluorescence wavelengths as they pass through the dye stream. The tuning wedge is a Fabry-Pérot etalon with a large free spectral range (110 nm) and tunes the resonant cavity to any required point within the fluorescence bandwidth. The Fine Tuning Etalon is a thin (110 μm) uncoated piece of glass and acts as a transmission filter, narrowing the output line width and enabling finer control of the output wavelength, with free spectral range of 1.0 nm [114].

An output power of 7 W from the Spectra-Physics 171 Ar ion laser operated in multiline mode was able to produce a dye laser output power of about 120 mW at 636 nm. The dye solution was prepared as a 2 mM solution in ethylene glycol by dissolving 719 mg of R6G powder in 15 ml methanol and then adding 750 ml of ethylene glycol.

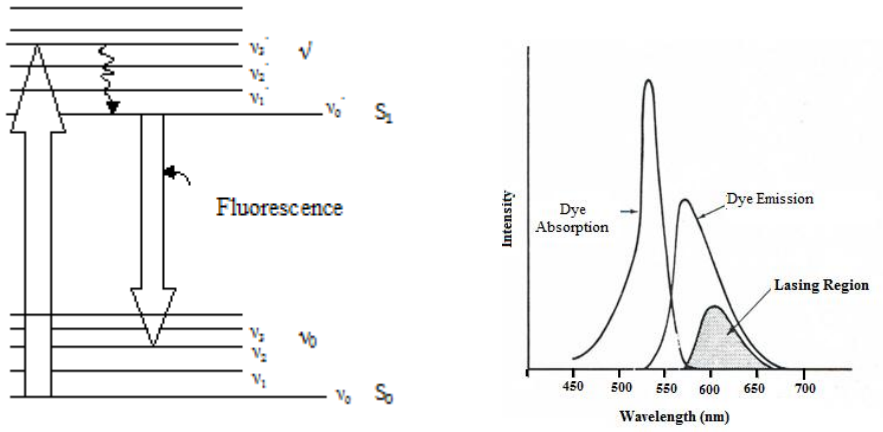


Figure 3.6. Rhodamine 6G dye characteristics showing the energy levels [113] and absorption and emission profiles [114].

## 3.3. ELECTROCHEMICAL CONTROL OF THE IRON SURFACE

### 3.3.1. Potentiodynamic Polarization

When the iron surface comes into contact with the 0.05 M NaOH solution, oxidation of the iron will occur spontaneously with simultaneous reduction of oxygen to produce $OH^-$. The oxidation reactions slow down to an almost negligible rate, i.e., the surface passivates, because initially the surface becomes covered with $Fe(OH)_2(s)$ (which is only slightly soluble and thus limits the rate at which $O_2(g)$ can reach the surface) and then further oxidizes to $Fe_3O_4$ and hydrated $Fe_2O_3$ [2]. The passive film thus behaves as a potential barrier between the iron surface and the electrolyte, and could be compared to a dielectric between two plates of a capacitor. The potential across the film would be given by the rest potential. From the Pourbaix diagrams [115] for the Fe-$H_2O$ system, the product expected to be stable at the rest potential at pH 12.7 which is -0.12 V vs. SHE (Standard Hydrogen Electrode) is $Fe_2O_3$.

For a controlled study of the passive film on iron it is necessary to carefully control the passivation process and this is achieved using a potentiostat. This enables the electrode potential to be carefully controlled to remain at a constant value (potentiostatic polarization) or to vary linearly with time (potentiodynamic polarization), while at the same time monitoring the current resulting from reactions occurring at the electrode surface. Thus the behaviour of the metal surface can be reliably and reproducibly studied in different electrolytes. In order to start the passive film growth on bare metal, the surface is initially subjected to cathodic polarization at a very negative potential to reduce any oxides formed on the surface on exposure to air and the solution. Thereafter the potential is increased at a fixed rate to more positive potentials, causing anodic (or oxidation) reactions to occur on the surface which produce significant current changes. The sweep direction of the potential can be reversed again to negative potentials, producing cathodic (or reduction) reactions at the surface. These events can be recorded in a polarization curve which is a plot of current (or current density) vs. applied potential.

Figure 3.7 shows the polarization curves for seven successive cycles of anodic and cathodic sweeps at 10 mV/s for iron in 0.05 M NaOH, between -1.4 V

and +0.6 V vs. Ag/AgCl in 3M KCl (or -1.2 V and +0.8 V vs. SHE). The current peaks on the top and bottom sweeps represent the anodic and cathodic reactions occurring on the surface, respectively; these occur between -1.4 V and about -0.5 V and represent the active region of the polarization curve. The passive region occurs between about -0.5 V and +0.6 V, when the current drops to negligible values and the surface passivates. This region is of particular interest for pitting studies because the onset of stable pitting occurs at a specific potential in this region and is indicated by a dramatic rise in current. Potentiodynamic polarization is used to empirically determine this potential which is referred to as the critical pitting potential, represented by $E_c$ or $E_p$.

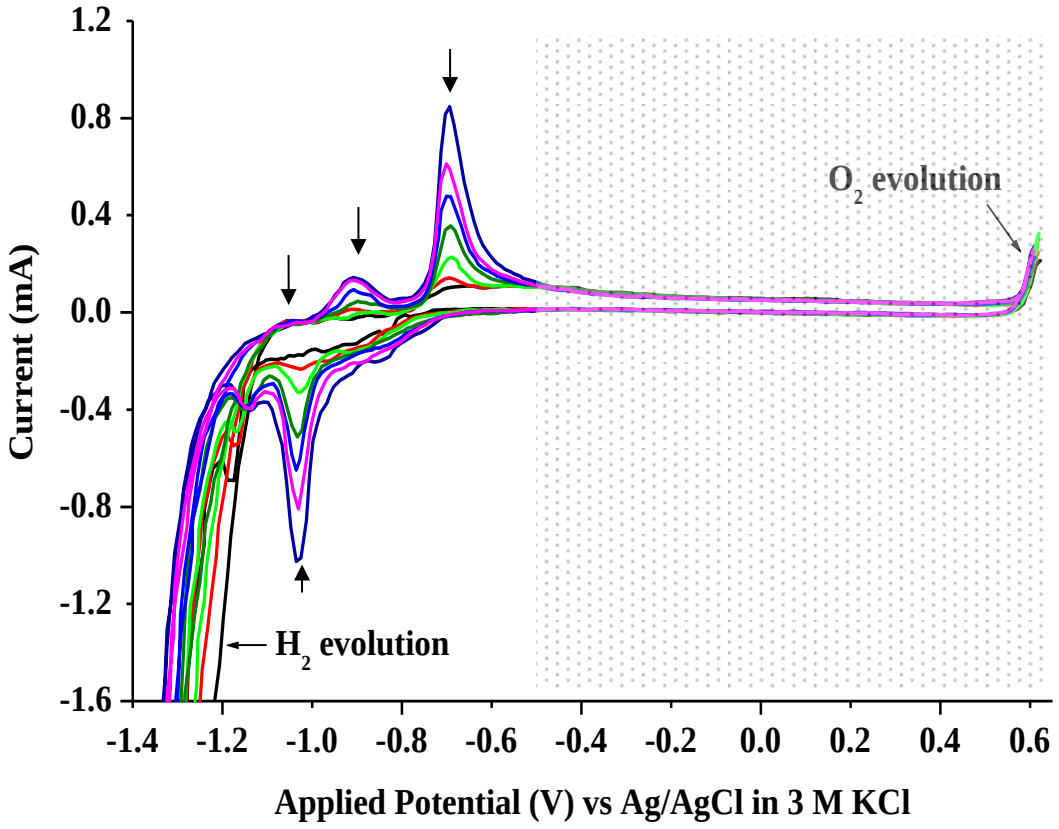


Figure 3.7. Seven polarization cycles between -1.4 V and +0.6 V vs. Ag/AgCl in 3 M KCl (-1.2 V and +0.8 V vs. SHE) in 0.05 M NaOH. Current Peaks are indicated on the anodic (top) and cathodic (bottom) sweeps, representing oxidation and reduction reactions of the surface film, respectively. The potentials at which the film becomes passive are indicated by the shaded area.

With increased cycling the current peaks increase in intensity, indicating that film growth occurs on the surface. The current (or current density) at any potential is a measure of the maximum rate at which the electrode reaction can occur. Often the net current density observed in the polarization curve is the superposition of several partial processes occurring at the electrode simultaneously at the same potential because they are all thermodynamically favourable. This can be determined from [113]:

$$\Delta G = - nFE$$

where n = number of electrons transferred, F = Faraday constant and $E$ is the half cell potential. However, not all the reactions that are thermodynamically favourable might occur at the same rate.

The potentials at which the current peaks occur correspond to the electrode potential for that reaction, which can be identified with the help of Pourbaix diagrams [115] calculated from the Nernst equation and solubility data for the various metal compounds [113]:

$$E = E^{o} - 2.3\frac{RT}{nF}\log\frac{a_{red}}{a_{oxi}}$$

where $E$ = the half cell potential, $E^{o}$ is the standard electrode potential and $a_{red}$ and $a_{oxi}$ = activities (or concentrations) of the reductants and oxidants, respectively.

The Pourbaix diagrams show which species are the most stable for a particular pH value and potential. The Pourbaix diagrams for the iron-water system [115] are given in Figure 3.8 considering as solid substances only Fe, $Fe_3O_4$ and $Fe_2O_3$, and in Figure 3.9 considering as solid substances only Fe, $Fe(OH)_2$ and $Fe(OH)_3$. In each figure the blue dashed lines indicate evolution of $H_2$ and $O_2$, and the red dashed line indicates the pH for the 0.05 M NaOH electrolyte which is 12.7.

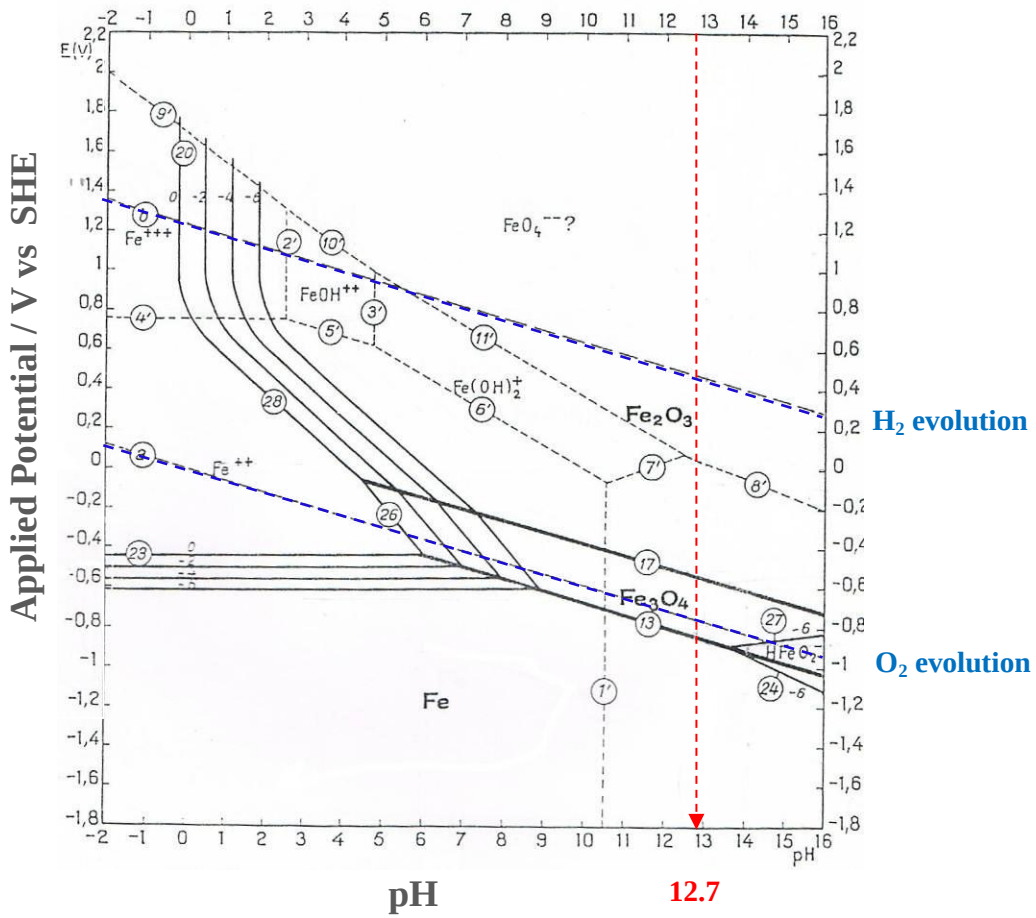


Figure 3.8. Pourbaix diagram [115] of the oxidation state of the surface of iron at different potentials (in V vs, SHE) in solutions of different pH values, considering as solid substances only Fe, $Fe_3O_4$ and $Fe_2O_3$.

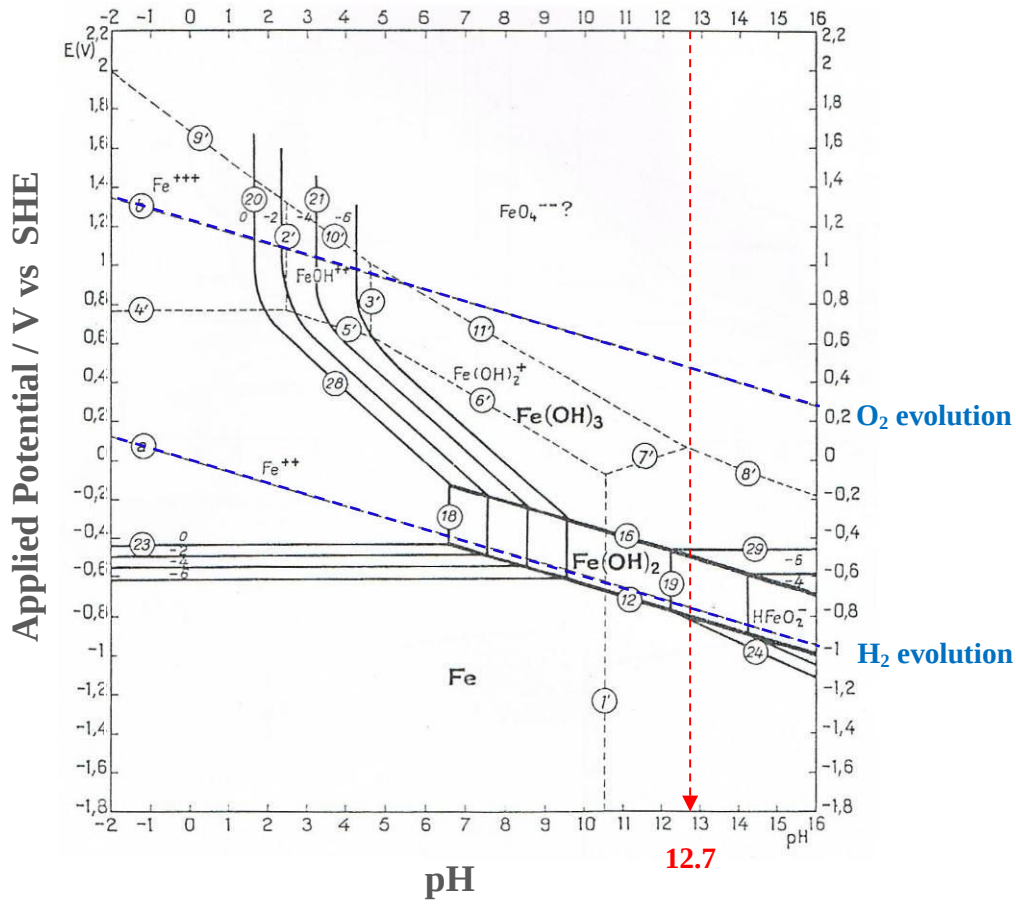


Figure 3.9 Pourbaix diagram [115] of the oxidation state of the surface of iron at different potentials (in V vs SHE) in solutions of different pH values, considering as solid substances only Fe, $Fe(OH)_2$ and $Fe(OH)_3$.

It can be seen from the Pourbaix diagrams that polarizing the iron surface in 0.05 M NaOH (pH 12.7) to -1.2 V (-1.4 V vs. Ag/AgCl in 3 M KCl) would allow reduction of any surface oxides back to Fe; at the same potential the sharp increase in (negative) current seen in Figure 3.7 is due to reduction of water to $H_2$. As the potential is increased oxidation occurs on the surface and the thermodynamically stable compounds are $Fe_3O_4$ and $Fe(OH)_2$. As the potential is increased still further the stable compounds are $Fe_2O_3$ and $Fe(OH)_3$, the latter transforming with time to $Fe_2O_3.nH_2O$ or FeOOH. At +0.8V (+0.6 V vs. Ag/AgCl in 3 M KCl) the current increases sharply due to oxidation of water to $O_2$.

### 3.3.2. Three-electrode electrochemical cell and potentiostat

The instrumentation used for the potentiodynamic polarization consisted of a potentiostat and a three-electrode electrochemical cell. The three electrodes were:

· pure iron as the working electrode (**WE)**

· Ag/AgCl in 3 M KCl as the reference electrode, (**RE)**, and

· a Pt ring electrode as the counter electrode, (**CE).**

The cell comprises both resistive and capacitative components but for simplicity only the resistive components are shown in the basic diagram in Figure 3.10 [116] with the equivalent circuit below. The series resistance, $R_S$, simulates the effective series resistance produced by the CE and the cell electrolyte, whilst the potential developed across the resistance $R_C$, due to the flow of current between the WE and CE, simulates the controlled potential of the WE with respect to the RE [116].

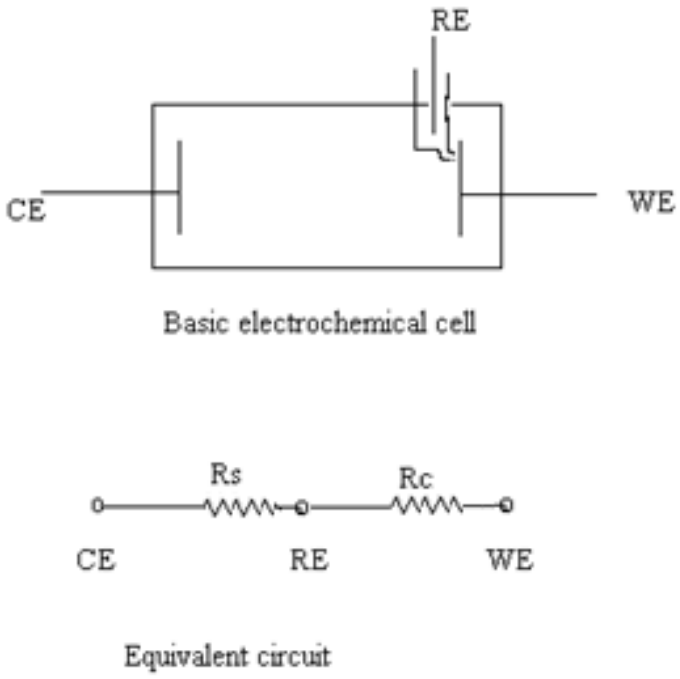


Figure 3.10. Schematic diagram of the three electrode cell (top), with equivalent circuit (bottom) [116].

The three electrodes are connected to a potentiostat which consists of a direct current power supply, a reference potential potentiometer, a high gain

voltage pre-amplifier and a power amplifier. Basically, the potentiostat maintains the metal working electrode at a preset potential, which is set at the reference potential potentiometer, by passing necessary current between the WE and the CE. If the current flow between the WE and the CE changes because of surface reactions at the WE, the pre-amplifier very quickly switches the Power Amplifier on to change the output potential of the power amplifier at the CE so that current will flow and adjust the potential between the WE and RE; in this way it is always maintained to the set potential. Any changes in current that were necessary to maintain the voltage will be measured as the current output of the potentiometer [116].

A three-electrode cell was designed and built to fit on the microscope stage of the Jobin-Yvon T64000 Raman spectrometer. The cell was designed so that temperature and flow rate of the electrolyte, as well as the type of metal to be corroded could be varied. The body and lid of the cell were made from A316 stainless steel and the window in the lid was made of quartz.

The WE was made from a polished disk of 99.98% pure single crystal iron. A 2 mm thick disc was cut from a 10 mm diameter rod of the iron using a diamond rotary blade. It was then polished with 1200 grit SiC and washed with distilled water and acetone. An iron wire (OD 0.5 mm) was connected to the disk by drilling a small hole in the side of the disk of a diameter just large enough to allow the wire to fit snugly. The wire was encased in a Teflon sleeve and the iron disk was then glued with Pratley Quickset Epoxy resin into a specially made cavity in a Teflon holder; care was taken to seal off the edges of the disk with glue so that only a 7 mm diameter of the face was exposed, as shown in Figure 3.11.

A glass Luggin probe with tip of inner diameter 0.5 mm was made for the Ag/AgCl RE in 3 M KCl (Metrohm AG) and a Pt ring counter electrode was made from a Pt wire of OD 1 mm (Johnson Matthey Noble Metals) which had been formed into a ring and pressed flat to thickness 500 μm with OD 9 mm and ID 5 mm. The connecting wire of the Pt ring electrode was sealed in a Teflon sleeve with Silicone Marine Sealant and inserted into the CE port of the cell.

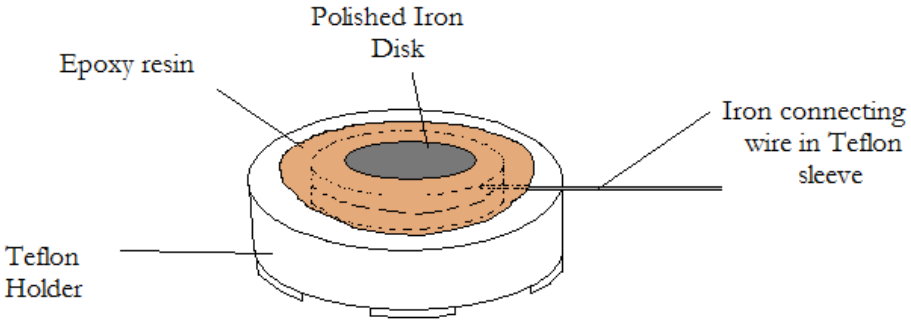


Figure 3.11. Schematic diagram of the iron disk glued into the Teflon holder as the WE.

The Pt ring CE was positioned in the cell 2 mm above and parallel with the surface of the iron WE (Figure 3.12) and the tip of the Ag/AgCl Luggin probe RE was positioned between the Pt ring CE and the surface of the WE to minimize separation between the reference and working electrodes for optimum potential control [117] while at the same time allowing *in situ* measurement of Raman spectra.

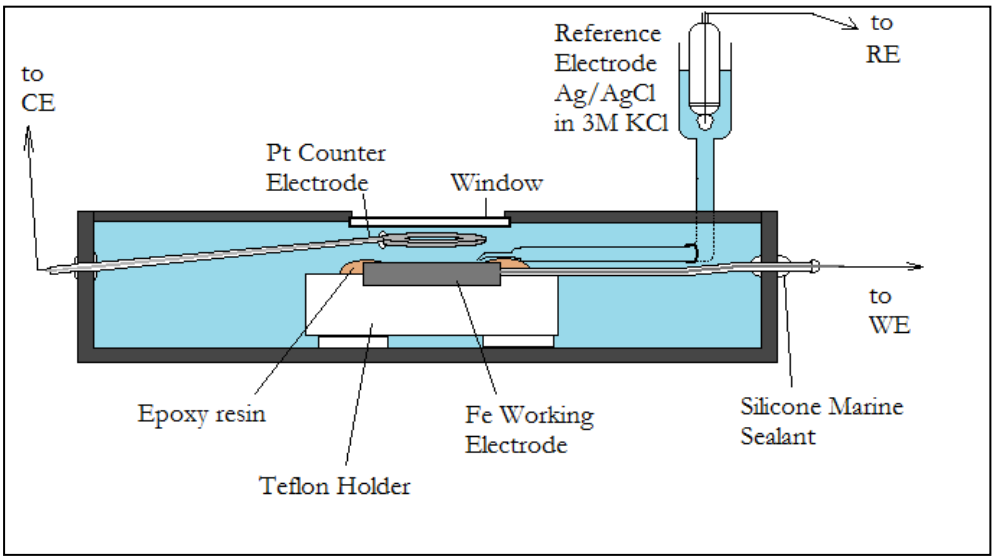


Figure 3.12. Schematic diagram of the assembled cell showing connection setup of the three electrodes between the cell and the potentiostat. The figure is not drawn to scale.

The layout of the cell showing the circulation ports is shown in the schematic diagram in Figure 3.13. The silicone tubing of OD 5 mm, ID 3 mm was inserted into two ports in the sides of the cell and connected to two glass tubes

which were inserted into a sealed 1l volumetric flask through a rubber stopper. The pipe was connected to a peristaltic pump (Ismatec MS-1 Reglo 6-160) to enable constant flow of electrolyte through the cell. A flattened glass spout (ID 4 mm × 1 mm) was made to fit onto the end of the silicon tubing feeding the electrolyte into the cell and was positioned onto an indent made on the side of the Teflon holder to allow the electrolyte to flow evenly over the surface. Once the lid was assembled the Pt ring counter electrode was positioned 2-3 mm from the iron surface. All external ports to the cell were sealed with Silicone Marine Sealant.

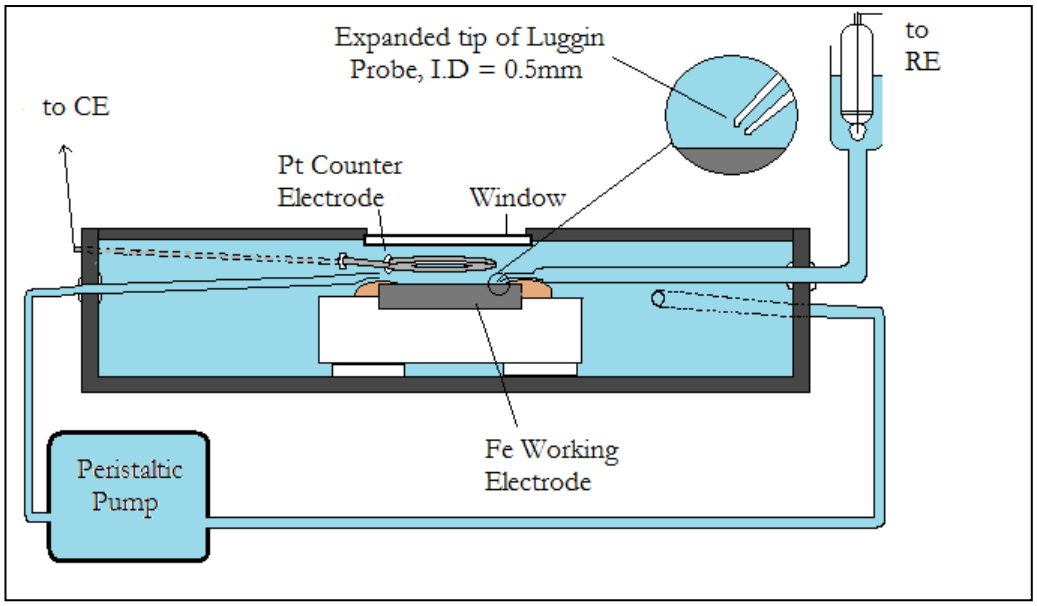


Figure 3.13. Schematic diagram of the assembled cell, rotated 90° relative to Figure 3.12 to show the connections on the sides for the circulating electrolyte. Also shown in the inset is an expanded view of the Luggin probe tip, which was positioned 1mm above the iron WE surface. The figure is not drawn to scale.

### 3.3.3. *In situ* Experimental Setup

For the *in situ* Raman measurement of the passive film during growth in 0.05 M NaOH, the three electrodes in the cell were connected to a BAS CV-27 integrating potentiostat (Bioanalytical Systems) which was connected to a computer; the analogue output of the potentiostat was connected to an OSIRIS Computerboard card (PIO-DAS-PHG) and collection of the data was performed using the Labtech Notebook software. For the *in situ* Raman measurement of the passive film during pitting conditions, the three electrode cell was connected to a Schlumberger SI1286 potentiostat (Schlumberger Technologies). A schematic

diagram is given in Figure 3.14 for the experimental setup for potentiodynamic polarization with the potentiostat and 3-electrode cell for the *in situ* Raman spectroscopic analysis. A photograph showing the three electrode cell positioned on the Olympus microscope stage of the JY T64000 Raman spectrograph is shown in Figure 3.15.

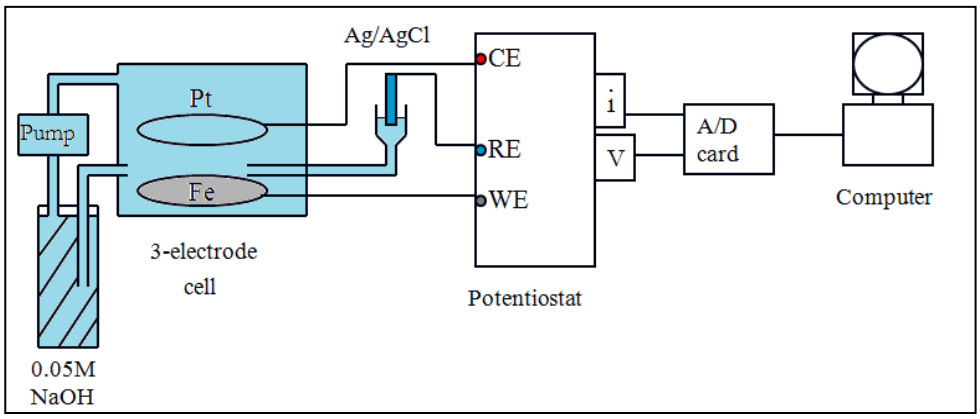


Figure 3.14. Schematic diagram of the experimental setup for potentiodynamic polarization with the potentiostat and 3-electrode cell.

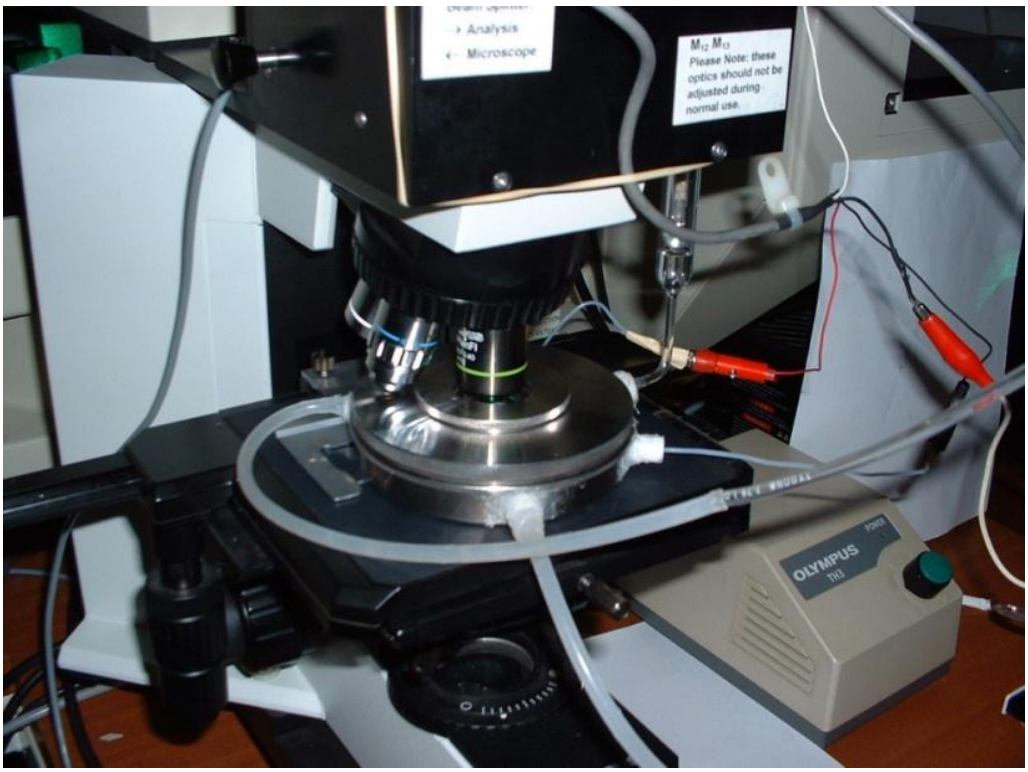


Figure 3.15. Position of the electrochemical cell during *in situ* recording of Raman spectra using the 514.5 nm laser beam focused onto the Fe surface through the quartz window using the 20× long-distance working objective of the Olympus confocal microscope attachment of the JY T64000 Raman spectrograph.

## 3.4. MULTIVARIATE CURVE RESOLUTION

Multivariate Curve Resolution is a Least Squares regression method used here to resolve multi-component spectra into the individual component spectra. This method was applied to resolve the *in situ* Raman spectra of the passive film into the individual spectra of a number of different iron oxide and oxyhydroxide compounds. The MCR-ALS (Multivariate Curve Resolution with Alternating Least Squares) toolbox of MATLAB [118] was used, in which iterative optimization of the resolved concentration and spectral profiles was performed to fit the spectra, subject to selected constraints. The MCR-ALS algorithm performs a bilinear decomposition of the data matrix, *D,* into the pure spectral response files associated with the variation of each contribution in the row and column directions, represented by matrices *C* and $S^T$ respectively, which are responsible for the observed data variance [118]:

$$D = CS^T + E,$$

where *D* is the data matrix consisting of rows of *in situ* spectra, $S^T$ is a matrix consisting of columns of the pure component spectra, *C* is a row matrix representing the contributions of the columns of the pure component spectra in $S^T$, and *E* is an error matrix which consists of the residuals not explained by the model. An overview of the process is given in a schematic flow diagram [118] in Figure 3.16.

MCR-ALS solves the above equation iteratively by an alternating least squares algorithm which is able to calculate the *C* and $S^T$ matrices that optimally fit the experimental data matrix *D*. If the spectra of the pure components are available, the spectral profiles in the $S^T$ matrix can be constrained to remain invariant during the optimization so that only their concentrations, or relative amounts, are optimized [118].

The *in situ* spectra were entered as rows into a data matrix, D, with the dimensions of the matrix being n × p, where n was the number of *in situ* spectra and p the wavenumbers of the set of spectra between 270 and 950 $cm^{-1}$. The spectra of the individual iron oxide compounds which had been recorded under the same conditions were entered into the matrix of pure spectral responses, S. During the optimization the spectral and concentration matrices were constrained

to remain non negative and the pure component spectra were constrained not to vary.

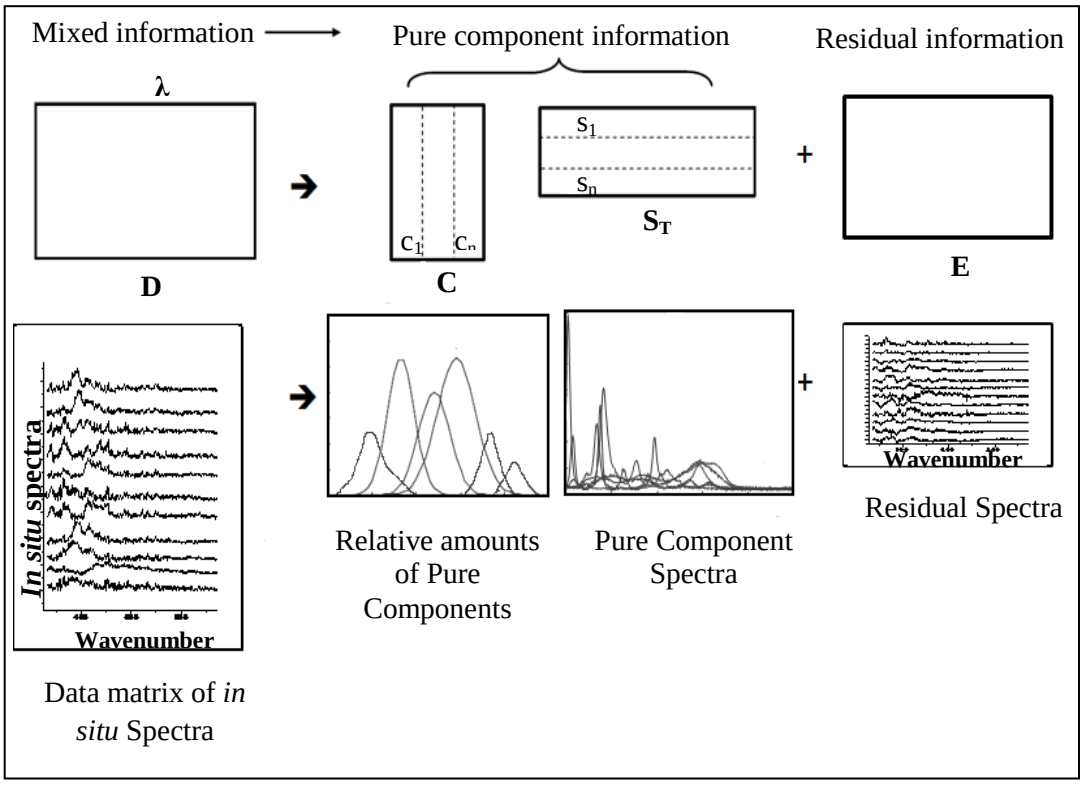


Figure 3.16. Summary of the data and component matrices in the MCR-ALS optimization [118].

The optimal percent lack of fit in relative standard deviation units is given by [118]:

$$\% \text{ lack of fit} = 100 \times \sqrt{\frac{\sum_{i,j} e_{ij}^2}{\sum_{i,j} d_{ij}^2}}$$

and two values are calculated for this:

1) where $e_{ij}$ are the residuals obtained between the raw data set and the reproduced data set using the optimized concentration and spectra profiles, and $d_{ij}$ are the elements of the raw data set, and

2) where $e_{ij}$ are the residuals obtained between the data set reproduced from PCA (Principal Component Analysis) and the data set reproduced using the optimized concentration and spectra profiles, and $d_{ij}$ are the elements of the

dataset reproduced from PCA (using the same number of components as the raw data set).

The two values should be similar for low noise systems where all possible contributions can be described with a bilinear model [118].

# CHAPTER 4

# THE GROWTH OF THE PASSIVE FILM ON IRON IN 0.05 M NaOH STUDIED *IN SITU* BY RAMAN MICROSCOPY AND ELECTROCHEMICAL POLARIZATION PART I: PRE-RESONANCE ENHANCEMENT OF THE RAMAN SPECTRA OF IRON OXIDE AND OXYHYDROXIDE COMPOUNDS

*(Content published in Journal of Raman Spectroscopy [119])*

## 4.1. INTRODUCTION

As already outlined in Chapter 1, the composition, structure and mechanism of formation of the passive film on iron formed in alkaline solutions have not yet been clearly established. From Raman [10-12,18,40,54], XPS [55], Mössbauer [30], ellipsometry [21,24,30,56], and SIMS [30,57] studies, iron oxide compounds such as hematite ($\alpha$-$Fe_2O_3$), maghemite ($\gamma$-$Fe_2O_3$), magnetite ($Fe_3O_4$), goethite ($\alpha$-FeOOH), akaganeite ($\beta$-FeOOH), lepidocrocite ($\gamma$-FeOOH) and feroxyhyte ($\delta$-FeOOH) have been reported to be present in the passive film on the surface of iron.

The study in this Chapter, which forms Part I of the investigation into the composition of the passive film on iron during the its growth by electrochemical polarization in 0.05M NaOH, is concerned with the optimization of the intensity of the Raman spectra of the iron oxides and oxyhydroxides listed above. As discussed below the optimized intensities have allowed the creation of improved standard Raman spectra of these compounds. The following Chapter (Chapter 5) forms Part II of this investigation, in which Raman spectra are recorded *in situ* of the passive film during its growth by potentiodynamic polarization. The resulting complex spectra, consisting of multiple components that changed in composition and whose Raman bands overlapped extensively are analysed by Multivariate Curve Resolution with Alternating Least Squares analysis (MCR-ALS) making use of the optimized Raman standard spectra reported here.

The He-Ne laser operating at 632.8 nm has been used previously to record (i) Raman spectra of some of the relevant iron oxides and oxyhydroxides, producing more intense bands than those obtained with the 514.5 nm line of the Argon ion laser and without fluorescence; [120,121,125] and (ii) *in situ* Raman spectra of the iron and steel surfaces [126-128]. However, the maximum beam power output of a conventional He-Ne gas laser is ~ 50 mW. This would be inadequate after passage through the spectrograph optics, filters, electrolyte solution and quartz window of the electrochemical cell used for our *in situ* studies of the initial stages of growth of the passive film, as described in Part II of the investigation in Chapter 5.

The work presented here in Part I demonstrates that significant enhancements of the Raman spectra of the iron oxides and oxyhydroxides discussed above can be achieved using an optimized excitation wavelength of 636.4 nm, providing further improvement over those attained with the 632.8 nm excitation wavelength under similar conditions. Furthermore, by using a tuneable dye laser, higher output powers of up to 130 mW were available, thus also overcoming potential difficulties discussed above in using a He-Ne laser. The optimized experimental methodology has been used to provide standard Raman spectra of a suite of iron oxide and oxyhydroxide powder samples.

## 4.2. EXPERIMENTAL PROCEDURE

The Jobin-Yvon T64000 Raman spectrograph was used in the single spectrograph mode with a holographic dispersive grating of 600 g/mm and a slit width of 200 μm giving a resolution of 6 $cm^{-1}$. The single spectrograph mode was selected since the intensity reduction in the triple subtractive mode was prohibitive in the present experiments; this required the use of holographic notch filters (HNFs) for the rejection of the quasi-elastically scattered light in acquiring satisfactory spectra. The powder samples employed in the present work were placed on the microscope stage of the Olympus confocal Raman microscope attached to the spectrograph. Raman spectra were recorded in a backscattering mode with a 100× objective (focal distance 0.21 mm), giving a laser spot size of ~2 μm. A Spectra-Physics SP375 tuneable dye laser used with R6G dye and pumped by a Spectra-Physics 171 Argon-ion laser operated in the all-lines mode provided the variable

wavelength laser excitation. The wavelength region surrounding that of 632.8 nm was chosen for detailed investigation as discussed above. This permitted the use of a standard 632.8 nm HNF (Kaiser Optics) as well as a 632.8 nm interference filter to reject plasma lines originating from the Argon-ion pump laser and transmitted through the dye laser which would result in fluorescence. Variation in excitation wavelength was thus restricted to the rejection band of the HNF, but in practice this proved adequate to obtain substantial enhancements of the Raman spectra. For comparison purposes, spectra were also recorded using the 514.5 nm line of a Coherent Innova 308 Argon-ion laser.

In a test experiment, the results of which were used to illustrate the advantages of the optimized excitation wavelength, a long focal length (12 mm) 20× microscope objective lens (with 0.4 NA) was used. Excitation wavelengths of 636.4 and 632.8 nm were provided by the tuneable dye laser at 19 mW (0.43 mW at the sample), 647.1 nm by a Spectra-Physics 165 Krypton-ion laser at 97 mW (1.27 mW at the sample) and 514.5 nm by the Argon-ion laser discussed above, at 50 mW (0.40 mW at the sample). A 647.1 nm HNF and 647.1 nm interference filter (both Kaiser Optics) were used with the 647.1 nm excitation line, and a 514.5 nm HNF and 514.5 interference filter (both Kaiser Optics) were used with the 514.5 nm excitation line.

The lepidocrocite (γ-FeOOH) sample in this instance was an existing laboratory sample whose Raman spectrum was similar to that of the standard spectra in the literature [130]. Powdered samples of α-$Fe_2O_3$, γ-$Fe_2O_3$, α-FeOOH, γ-FeOOH, β-FeOOH and δ-FeOOH which were used to record the standard Raman spectra were prepared according to methods of Schwertmann and Cornell [125]. $Fe_3O_4$ powder (99.9 % pure) was obtained from Sigma Aldrich. In order to confirm the structures of the standard samples and the absence of other phases, the iron oxide and oxyhydroxide powders were verified by X-ray diffraction using a Rigaku Mini-Flex II X-Ray diffractometer with monochromator at 30 kV, 15 mA and Cu radiation, 1°/min and a 2θ step size of 0.02. The results show excellent agreement with the standards given in the PDFMaintEx database (Figures 4.1 – 4.7). The origin of the extra band in the XRD pattern for feroxyhyte (Figure 4.4) at approximately 18° 2θ is most probably due to the plastic holder which was used for the powder sample: a smaller powder sample holder made of

plastic had to be used for this powder sample as there was only a small amount of sample available.

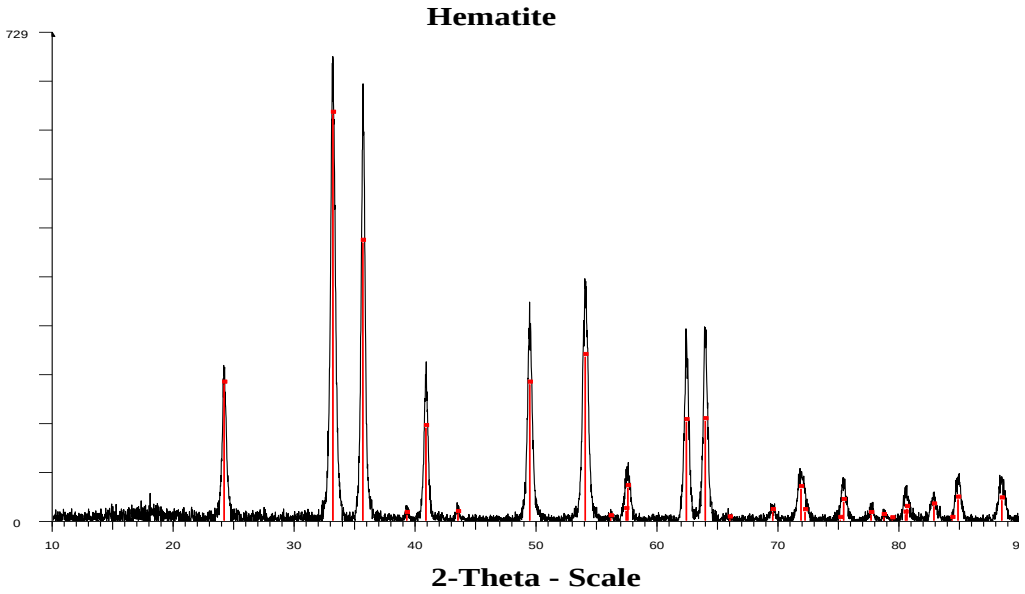


■ 01-087-1164(C)-alpha-$Fe_2O_3$-Hexagonal (Rh)-Primitive-R-3c (167)

Figure 4.1. XRD pattern of Hematite powder (black trace) with the best matching pattern from the PDFMaintEx database matched using the DIFFRACplus Evaluation package.

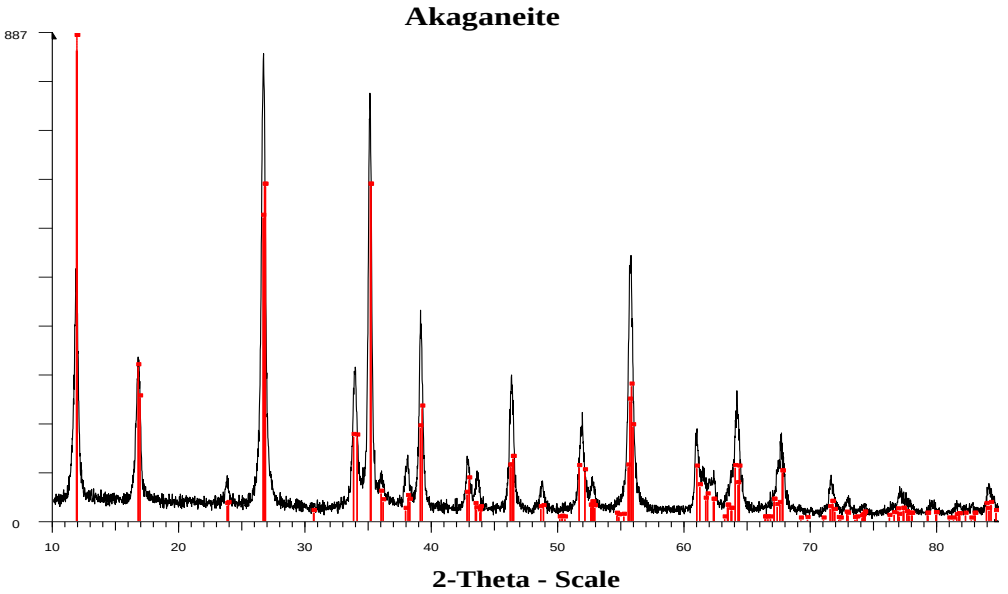


■ 01-080-1770 (C) - $Fe_8O_8(OH)_8Cl_{1.35}$ – WL: 1.54056 - Monoclinic - Body-centred-I2/m (12)

Figure 4.2. XRD pattern of Akaganeite powder (black trace) with the best matching pattern from the PDFMaintEx database matched using the DIFFRACplus Evaluation package.

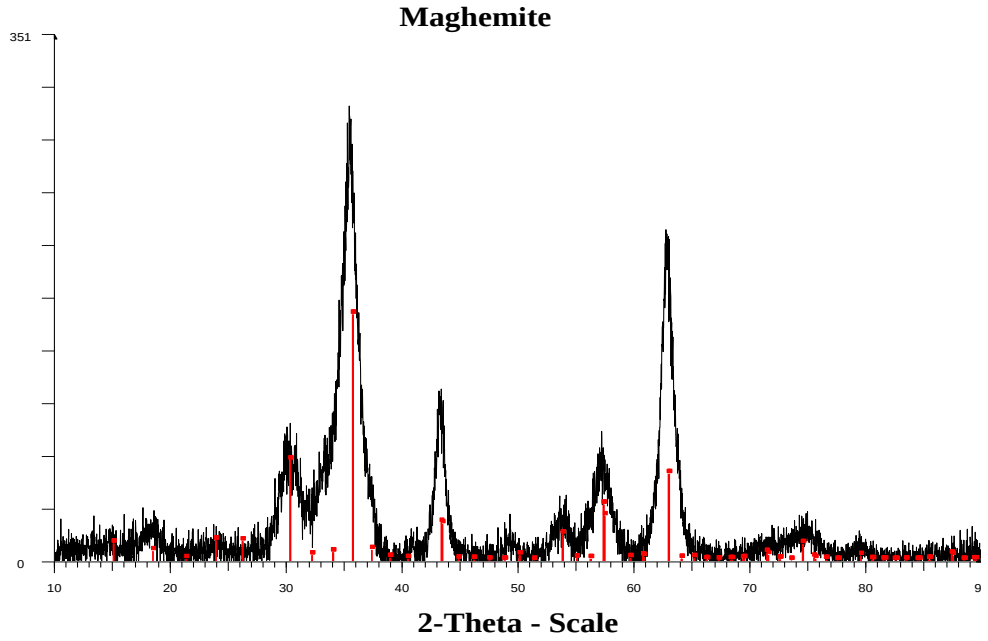


■ 00-004-0755(D)-gamma-$Fe_2O_3$ – WL: 1.54056 - Cubic – F24

Figure 4.3. XRD pattern of Maghemite powder (black trace) with the best matching pattern from the PDFMaintEx database matched using the DIFFRACplus Evaluation package.

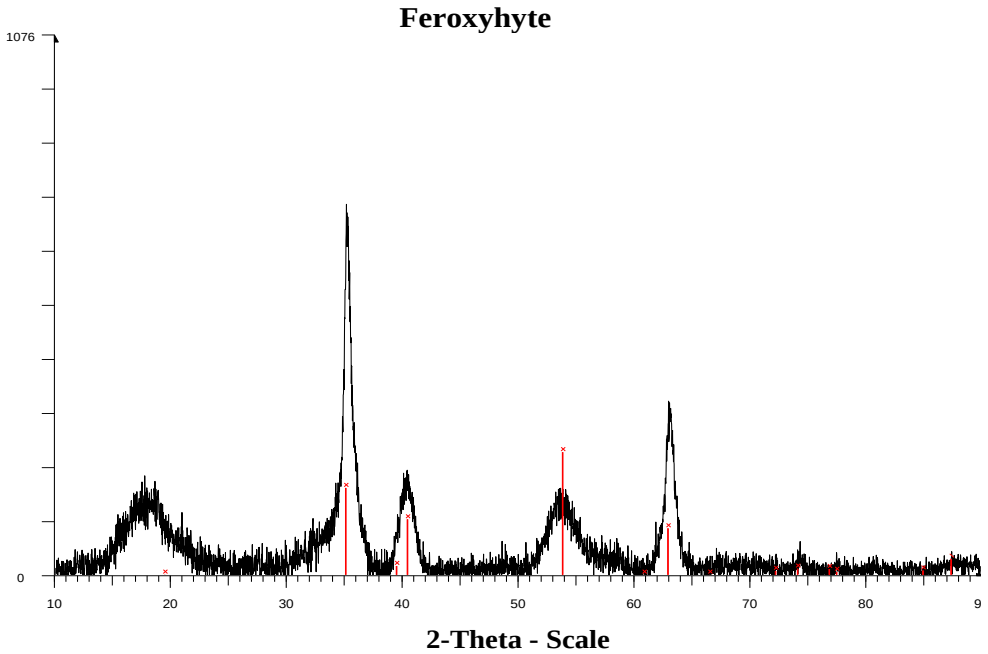


■ 01-077-0247 (C)- delta-FeOOH – WL:1.54056 - Hexagonal – Primitive – P-3m1(164)

Figure 4.4. XRD pattern of Feroxyhyte powder (black trace) with the best matching pattern from the PDFMaintEx database matched using the DIFFRACplus Evaluation package.

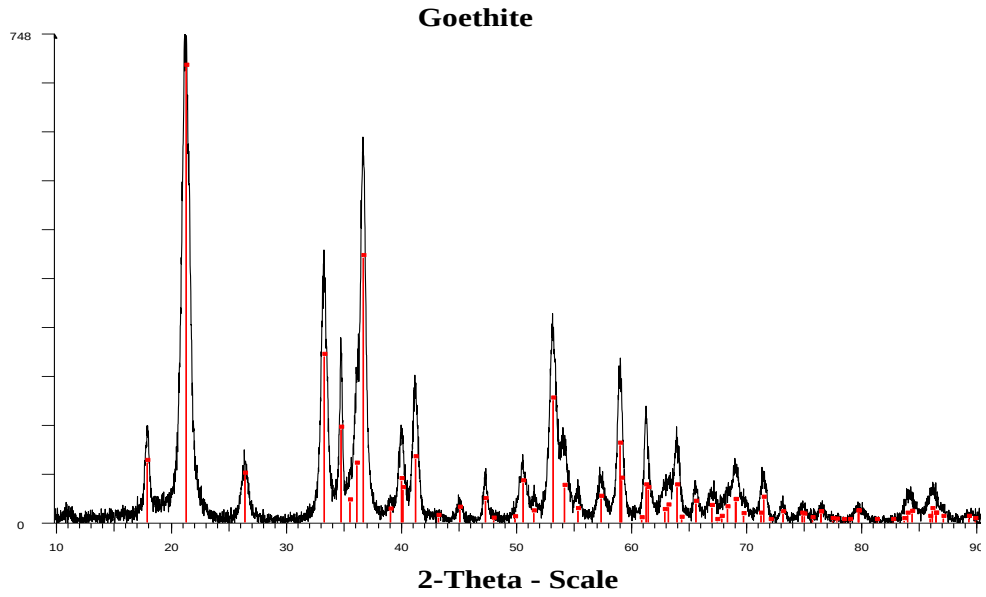


■ 01-081-0463(C) –Goethite, syn – FeO(OH) –WL: 1.54056 - Orthorhombic – Primitive – Pbnm (62)

Figure 4.5. XRD pattern of Goethite powder (black trace) with the best matching pattern from the PDFMaintEx database matched using the DIFFRACplus Evaluation package.

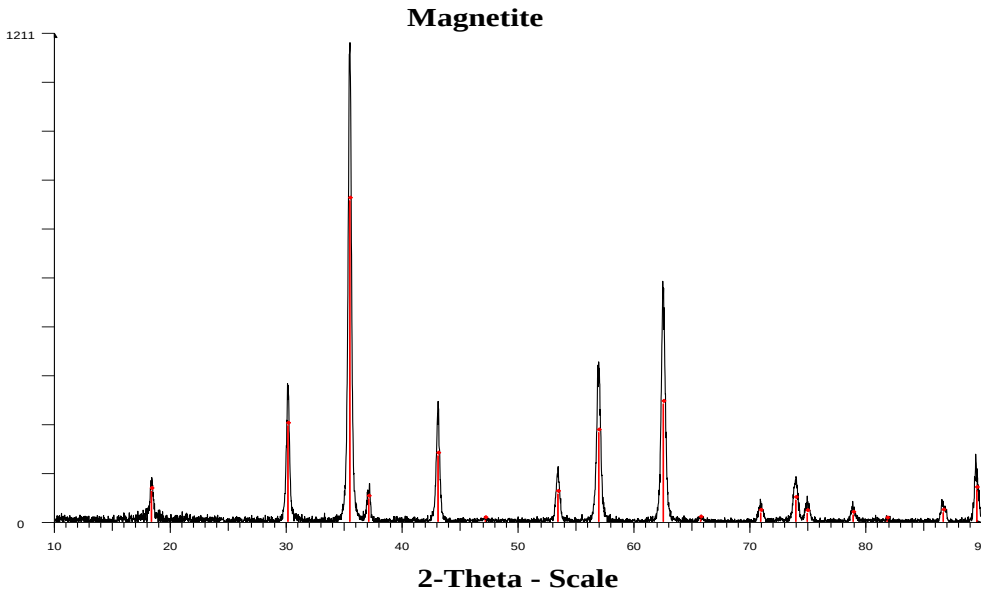


■ 01-087-0245 (C) –Magnetite– $Fe_{2.9}O_4$– L:1.54056 - Cubic–FCC-Fd-3m (227)

Figure 4.6. XRD pattern of Magnetite powder (black trace) with the best matching pattern from the PDFMaintEx database matched using the DIFFRACplus Evaluation package.

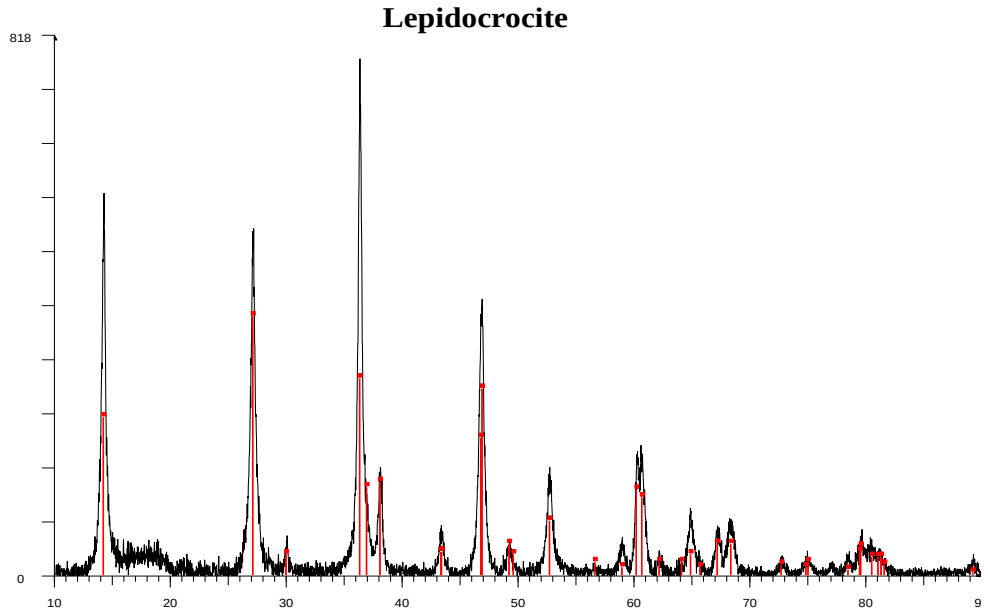


■ 00-044-1415 – Lepidocrocite $Fe^{+3}O(OH)$– WL: 1.54056 - Orthorhombic -Base Centred-Bbmm (63)

Figure 4.7. XRD pattern of Lepidocrocite powder (black trace) with the best matching pattern from the PDFMaintEx database matched using the DIFFRACplus Evaluation package.

## 4.3. RESULTS AND DISCUSSION

As an exploratory experiment, Raman spectra of the iron oxyhydroxide, lepidocrocite (γ-FeOOH), were obtained using various excitation wavelengths (Figure 4.8). It is evident that significantly enhanced band intensities are obtained with the 636.4 nm excitation (dye laser) compared with the other laser excitations, namely at 632.8 nm (dye laser, but equivalent to the wavelength of a He-Ne laser), at 647.1 nm (Krypton-ion laser) and at 514.5 nm (Argon-ion laser). It is to be noted that the beam powers and integration times for the Krypton- and Argon-ion laser excitations were significantly greater than those for the 632.8 and 636.4 nm excitations, further emphasising the scale of the spectral intensity enhancement. Indeed, the Argon-ion laser excitation at 514.5 nm produced a spectrum of particularly low intensity, this being consistent with the reported difficulties expressed in the Introduction in using this wavelength for Raman studies of the compounds of interest.

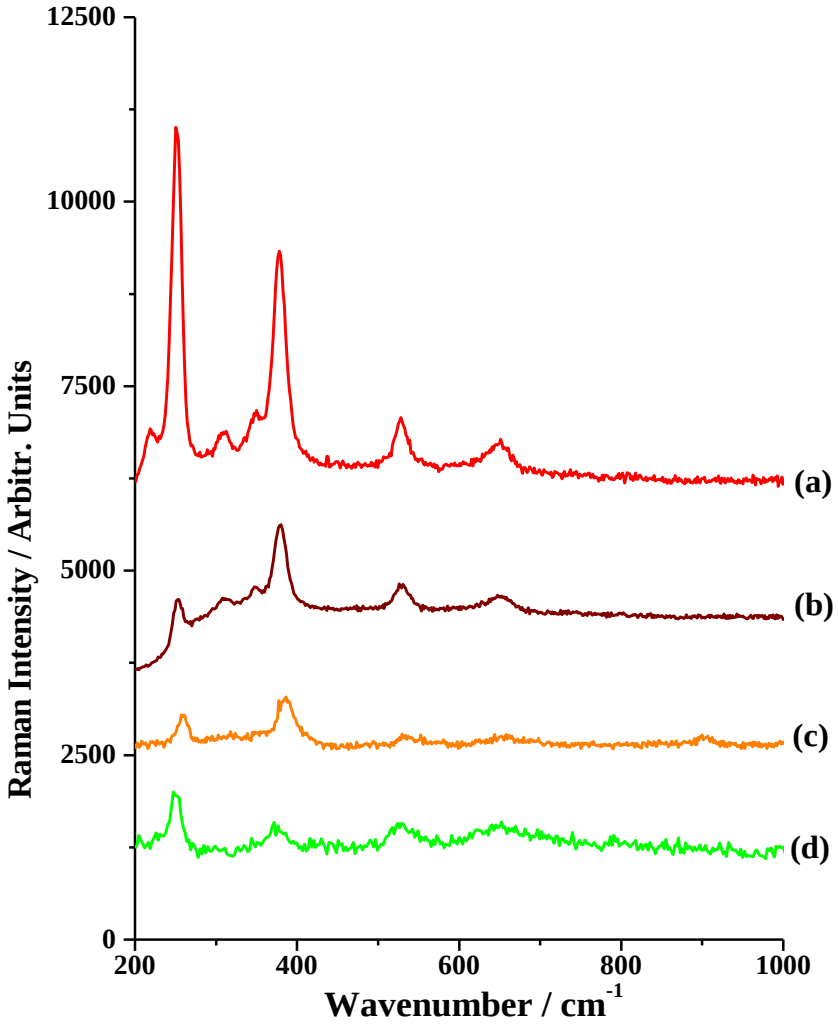


Figure 4.8. Variation of intensity of the γ-FeOOH (lepidocrocite) spectrum with different excitation wavelengths: (a) 636.4 nm at 19 mW, 20 s; (b) 632.8 nm at 19 mW, 20 s; (c) 647.1 nm at 97 mW, 30 s; (d) 514.5 nm at 50 mW, 240 s. The laser powers quoted refer to output power.

The spectrum of lepidocrocite using the 647.1 nm line of the Krypton-ion laser with a beam power of 97 mW and an integration time of 30 s has significant intensity. While the spectrum is undoubtedly weaker than that recorded using the 636.4 nm dye laser line at 19 mW for 20 s, it is probable that the true optimal excitation wavelength for the current suite of samples is in the range between 632.8 and 647.1 nm. Further study is necessary in order to clarify this issue.

In the spectrum of lepidocrocite shown in Figure 4.8, it is noted that as the excitation wavelength increases toward 640 nm, a greater increase in intensity is observed in the bands below about 400 $cm^{-1}$ relative to those at 527 and 648 $cm^{-1}$. The different degree of enhancement observed is most probably due to differences in the symmetries of the respective vibrational modes. There will be different enhancements of the various Raman active modes for a certain iron oxide compound under resonance (and pre-resonance) conditions using a particular excitation wavelength. There will also be different enhancements of the various Raman active modes if a different excitation wavelength is used under these conditions. The reasons for the effects are explained in the literature in some detail [107] and a brief account is given here.

The change in polarizability $\alpha$ as a result of the electronic transitions can be expressed in terms of two terms:

$$\left(\alpha_{\rho\sigma}\right)_{mn} \cong A + B$$

The terms *A* and *B*, if active, result in enhancements of the Raman modes, but under different conditions. It is shown that A-term enhancement is observed only for totally symmetric modes. Among the totally symmetric modes, the mode that leads to the excited state configuration is most strongly resonance enhanced. The *B*-term provides a mechanism for resonance enhancement of non-totally symmetric vibrations. The greater enhancement observed for the lower energy modes below 400 $cm^{-1}$, particularly that at 252 $cm^{-1}$, relative to those of higher energy may be due to differences in their symmetries.

The inset of Figure 4.9 shows an example of a triplet of bands occurring at higher wavenumber shifts of which the most intense is at 1562 $cm^{-1}$. These three peaks which were present in the Raman spectra of the iron oxide samples were also consistently observed in spectra from surfaces such as a reflecting mirror and the Pt ring surface in the cell. For this reason they were assigned as independent instrumental peaks. Their wavenumber shift is a linear function of excitation wavelength in the red region of the spectrum as shown in Figure 4.9.

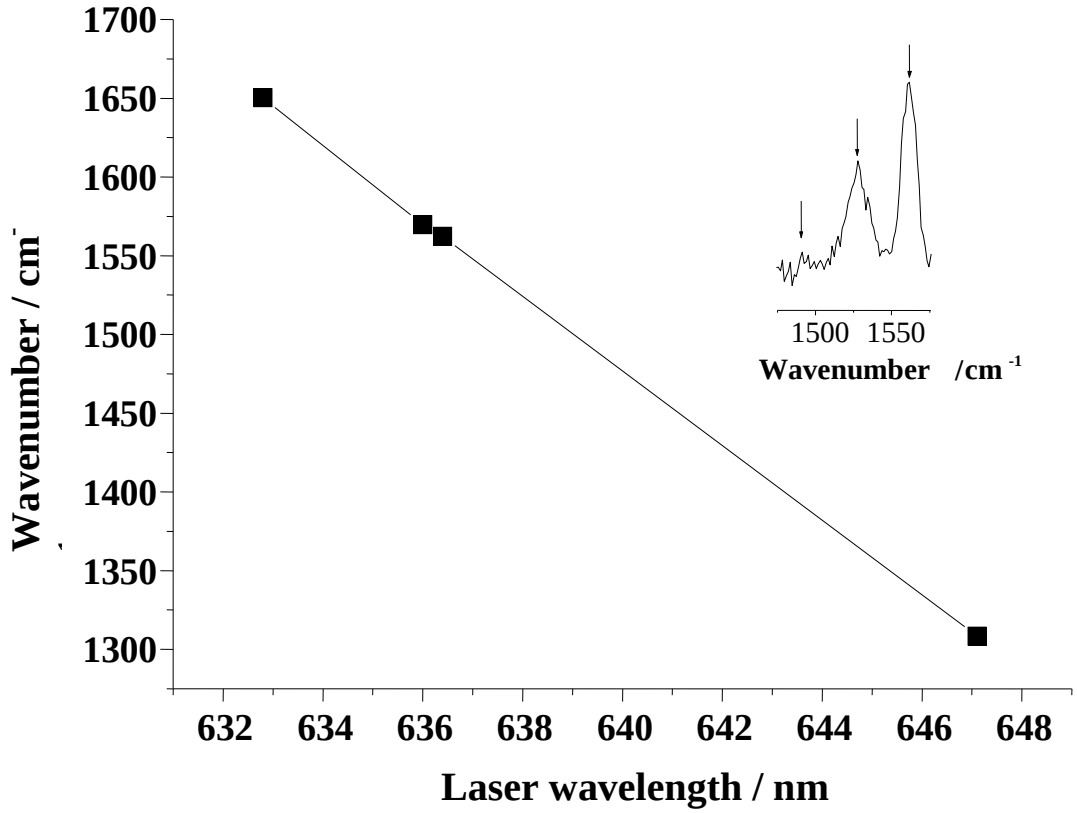


Figure 4.9. Variation in the wavenumber shift with excitation wavelength for the largest of the three instrumental peaks observed in spectra of the iron oxide compounds recorded with red excitation lines. The inset shows an example of the three instrumental peaks observed with a laser excitation wavelength 636.4 nm. The most intense peak is at 1562 $cm^{-1}$.

Since they do not overlap the iron oxide and oxyhydroxide spectral features, it proved advantageous to use the strongest of these instrumentally introduced bands at 1562 $cm^{-1}$ (observed with 636.4 nm excitation) to calibrate the band positions of the different iron oxide compounds. This was necessary because the incident wavelength from the dye laser was subject to minor shifts with time. The excitation wavelength was checked for shifts before and after recording each *in situ* spectrum and the dye laser was then re-tuned if necessary spectrum to ensure accuracy of the incident wavelength.

As discussed in the Introduction of this Chapter, Raman spectra of the respective iron oxide and oxyhydroxide powders were recorded to provide standard spectra for the Multivariate Curve Resolution with Alternating Least Squares analysis applied to the Raman spectra arising from the passive layer on iron recorded *in situ*. These standard spectra were all obtained using the excitation wavelength of 636.4 nm under exactly the same conditions: a dye laser power of 15 mW and an integration time of 240 s. The spectra were recorded in a backscattering mode with a 100× objective, giving a laser spot size of ~2 μm. At the sample surface the laser power was 0.340 mW after passing through the filters and microscope optics; the use of the low power was precautionary preventing possible sample heating, in particular of the $Fe_3O_4$ which would otherwise convert to α-$Fe_2O_3$. As an added precaution the magnitude of the 1562 $cm^{-1}$ instrumental band discussed above was used to normalize the intensities of the respective spectra of the iron oxide and oxyhydroxide samples obtained with the 636.4 nm excitation. These procedures produced the suite of normalized standard spectra shown in Figures 4.10 – 4.16. The wavenumber range shown is 200 – 1000 $cm^{-1}$ for consistency with Part II in Chapter 5. In each case a comparison is made between the spectra obtained with the respective 636.4 and 514.5 nm excitations with the same integration time and laser power at the sample (0.340 mW). In the case of the Argon-ion laser an output power of 50 mW was used. It is noted that with the 514.5 nm excitation, the spectra were not normalized because an equivalent instrumental band to that used for the 636.4 nm excitation was not available in the spectra.

The standard spectra recorded with the 636.4 nm excitation line are shown in Figures 4.10 – 4.16 for hematite (α-$Fe_2O_3$), lepidocrocite (γ- FeOOH), goethite (α-FeOOH), feroxyhyte (δ-FeOOH), magnetite ($Fe_3O_4$), maghemite (γ-$Fe_2O_3$) and akaganeite (β-FeOOH) along with those recorded using the 514.5 nm excitation.

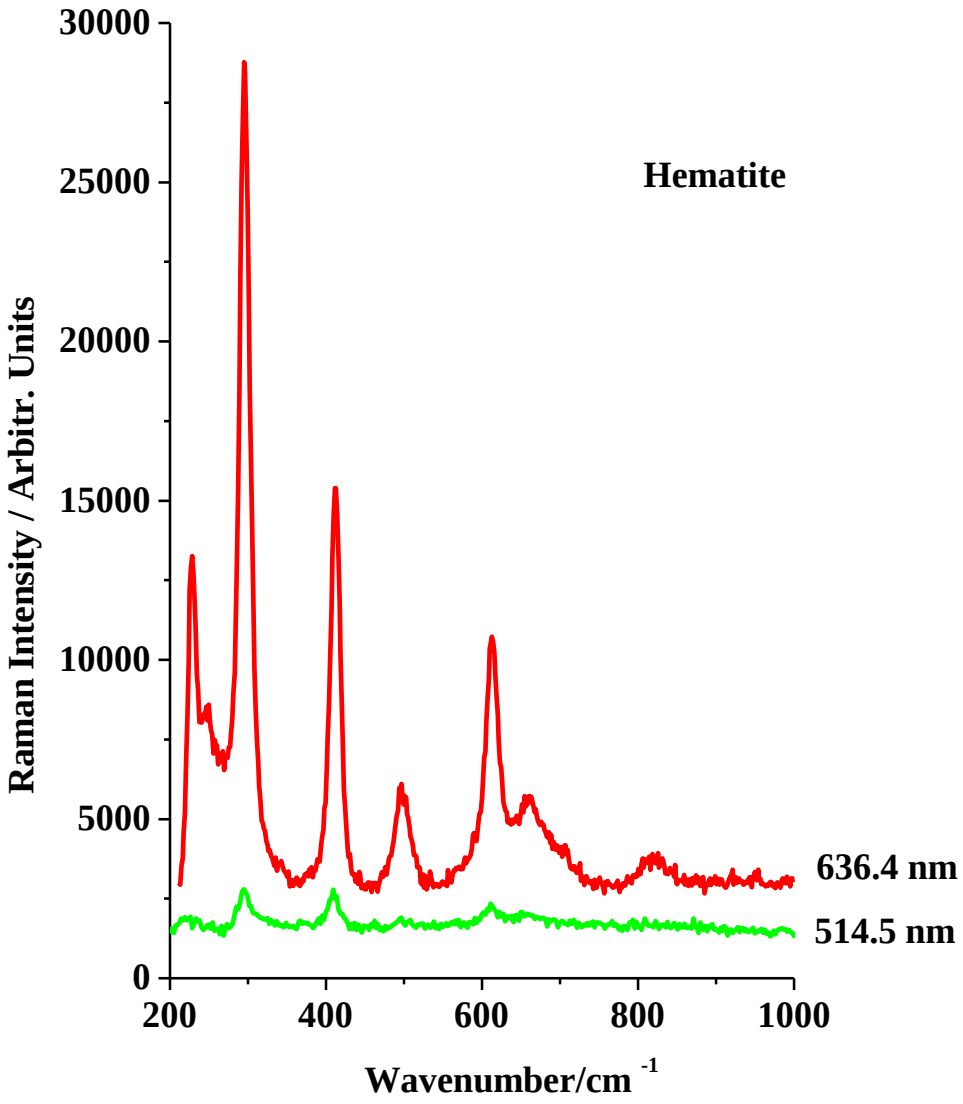


Figure 4.10. Standard Raman spectra of $\alpha$-$Fe_2O_3$ (hematite) showing the variation in intensity with different excitation wavelengths: 636.4 nm at 15 mW (0.340 mW at the sample) and 240 s integration time, and 514.5 nm at 50 mW (0.340 mW at the sample) and 240 s integration time.

Significantly improved intensities of the Raman spectra were obtained with the 636.4 nm excitation as compared with those using 514.5 nm for all the iron oxides and oxyhydroxides in powder sample form, with the greatest enhancements observed for $\gamma$-FeOOH, $\alpha$-$Fe_2O_3$ and $\alpha$-FeOOH.

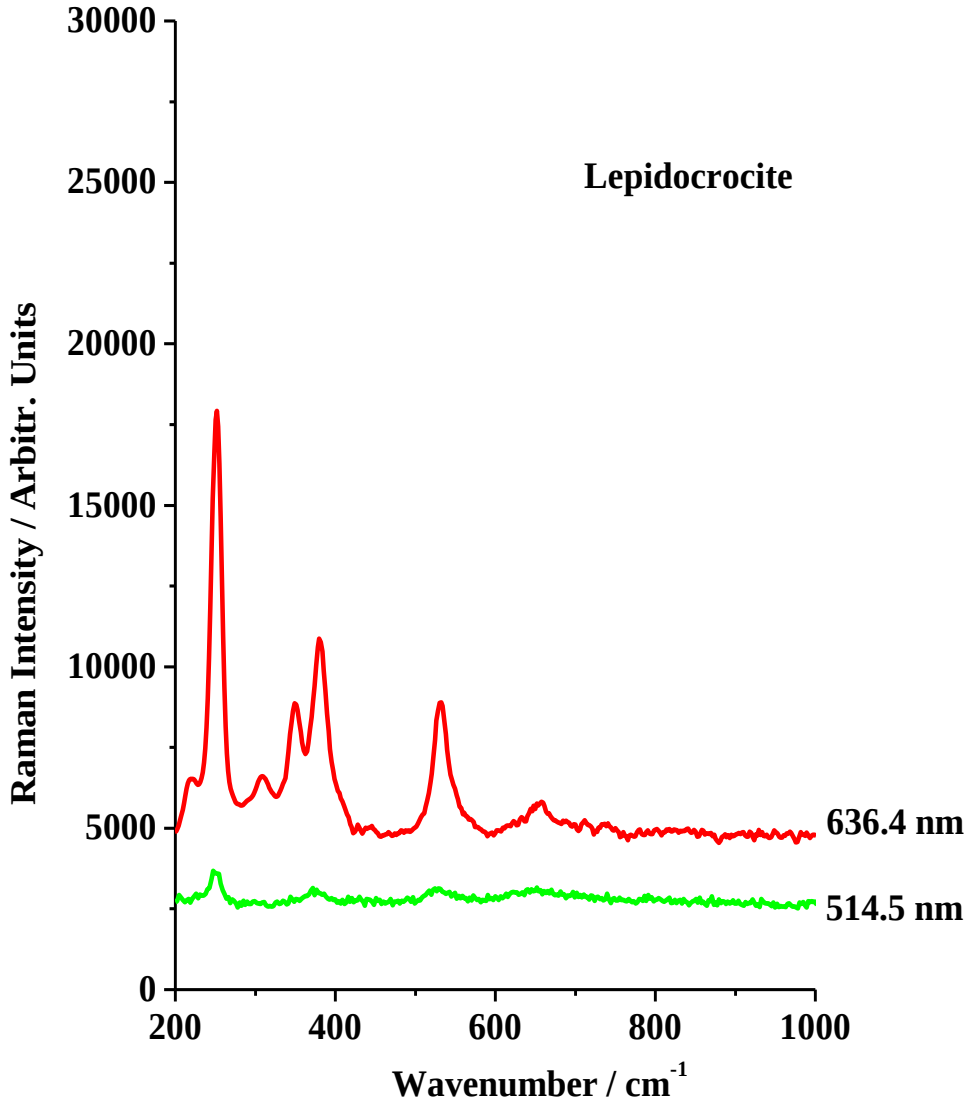


Figure 4.11. Standard Raman spectra of γ-FeOOH (lepidocrocite) showing the variation in intensity with different excitation wavelengths: 636.4 nm at 15 mW (0.340 mW at the sample) and 240 s integration time, and 514.5 nm at 50 mW (0.340 mW at the sample) and 240 s integration time.

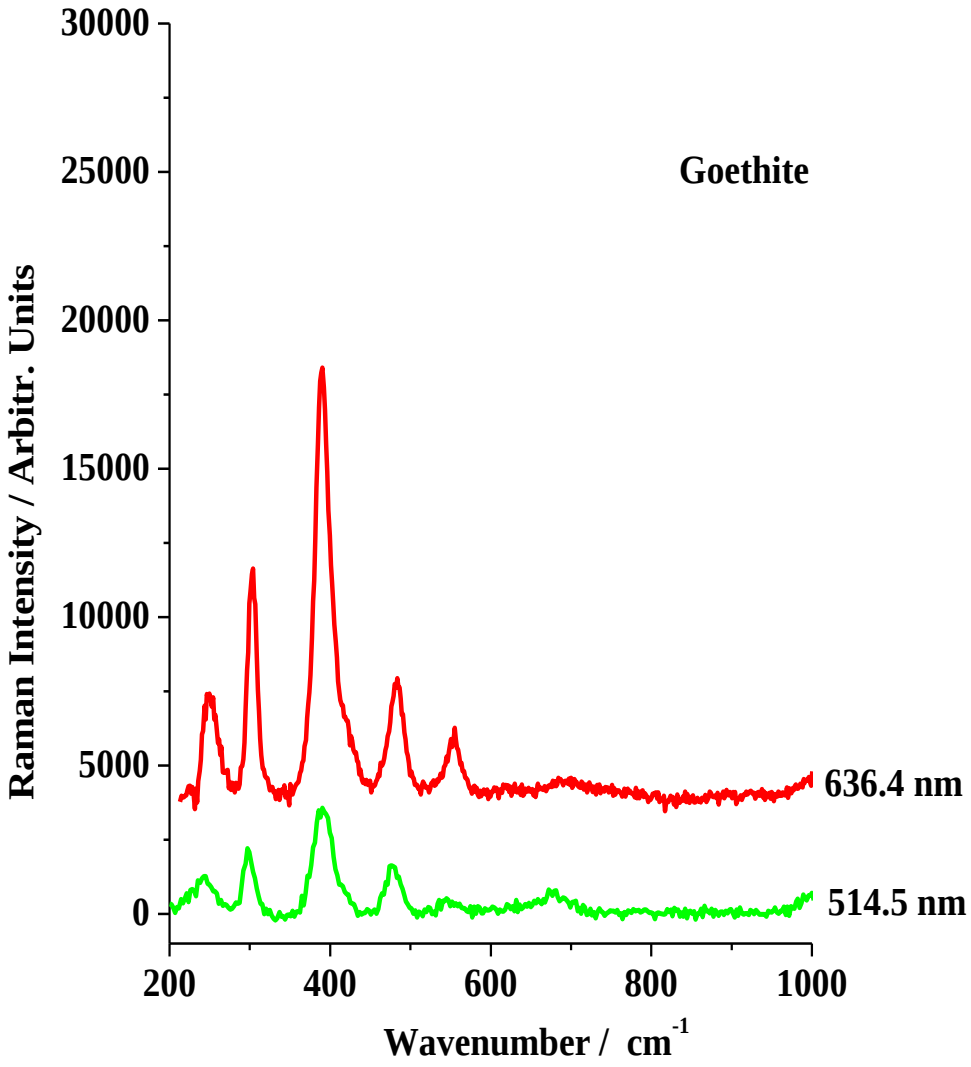


Figure 4.12. Standard Raman spectra of α-FeOOH (goethite) showing the variation in intensity with different excitation wavelengths: 636.4 nm at 15 mW (0.340 mW at the sample) and 240 s integration time, and 514.5 nm at 50 mW (0.340 mW at the sample) and 240 s integration time.

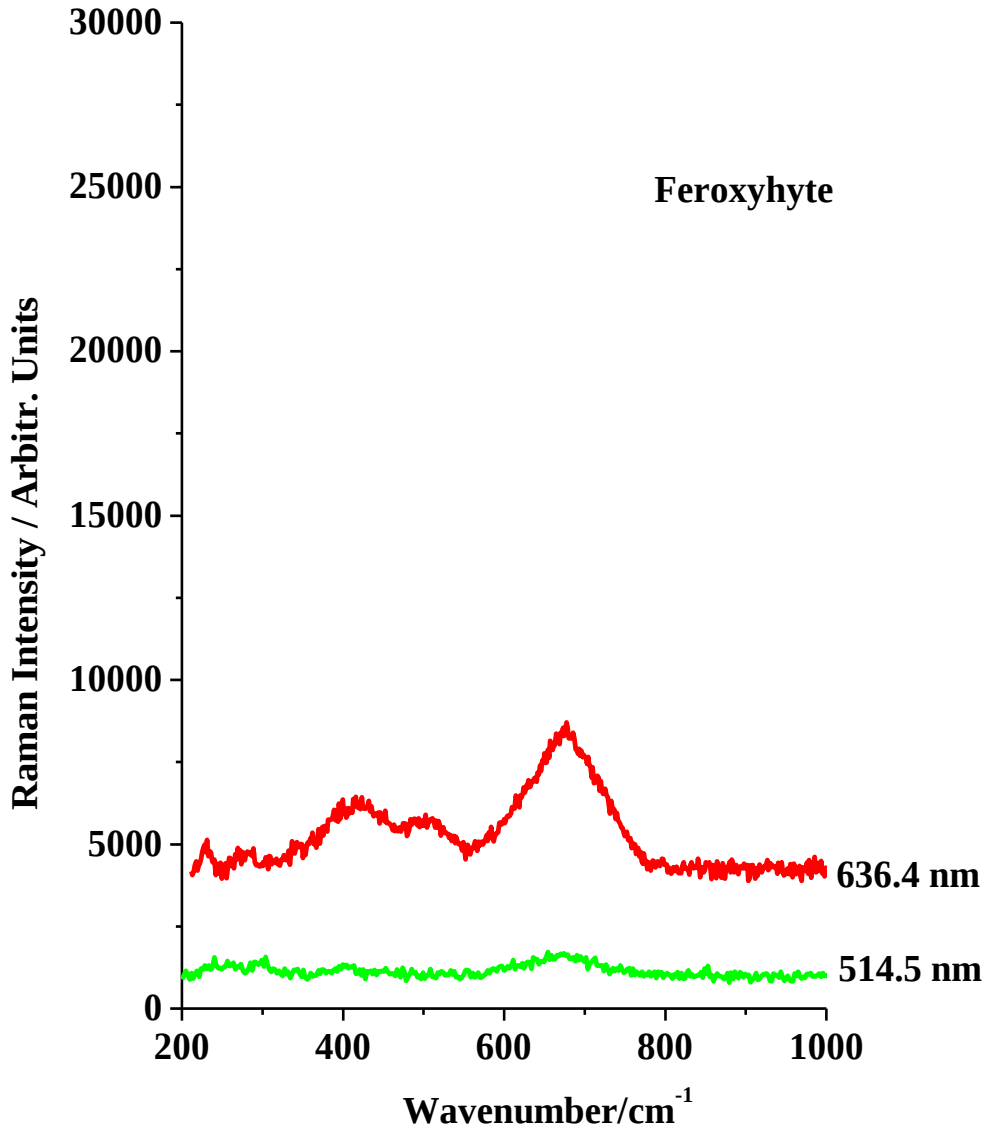


Figure 4.13. Standard Raman spectra of δ-FeOOH (feroxyhyte) showing the variation in intensity with different excitation wavelengths: 636.4 nm at 15 mW (0.340 mW at the sample) and 240 s integration time, and 514.5 nm at 50 mW (0.340 mW at the sample) and 240 s integration time.

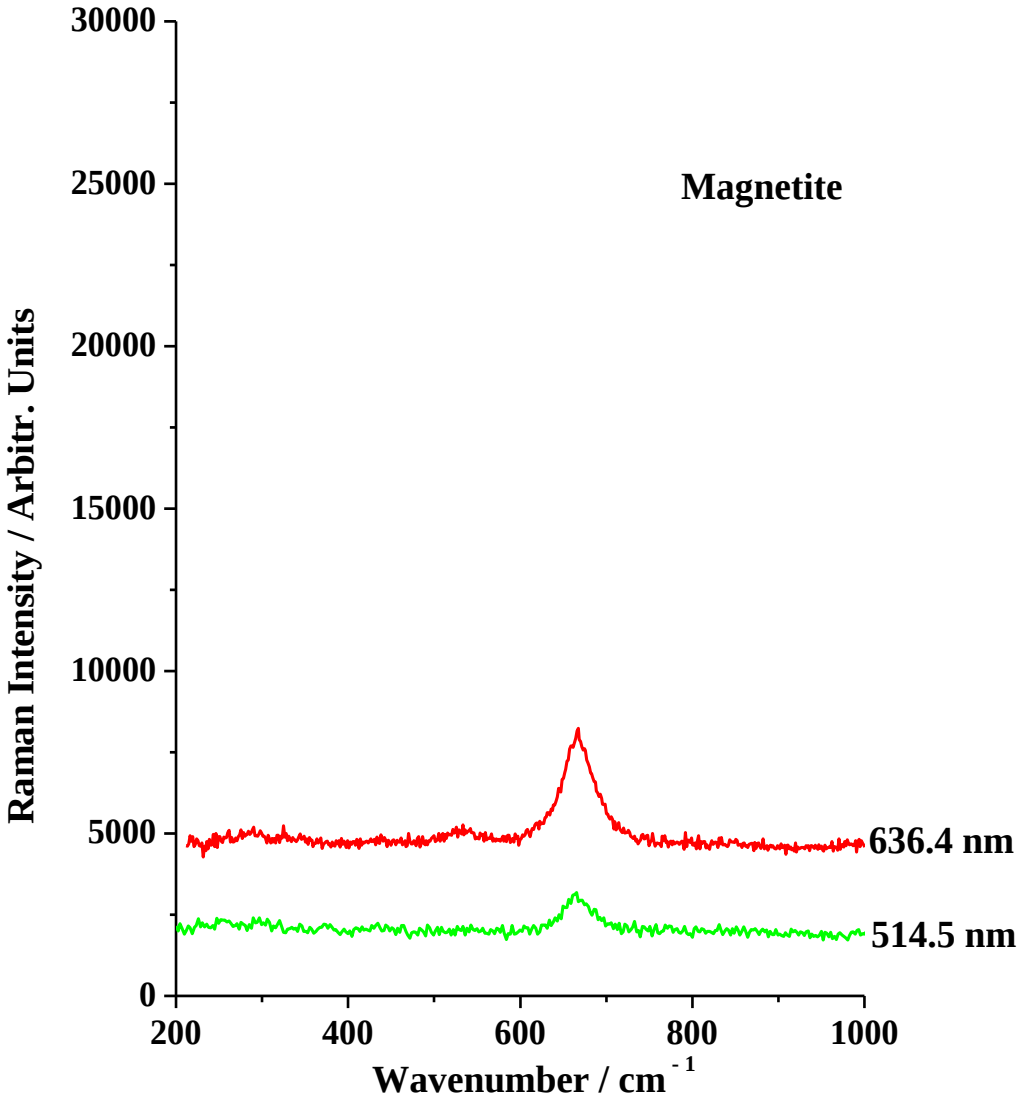


Figure 4.14. Standard Raman spectra of $Fe_3O_4$ (magnetite) showing the variation in intensity with different excitation wavelengths: 636.4 nm at 15 mW (0.340 mW at the sample) and 240 s integration time, and 514.5 nm at 50 mW (0.340 mW at the sample) and 240 s integration time.

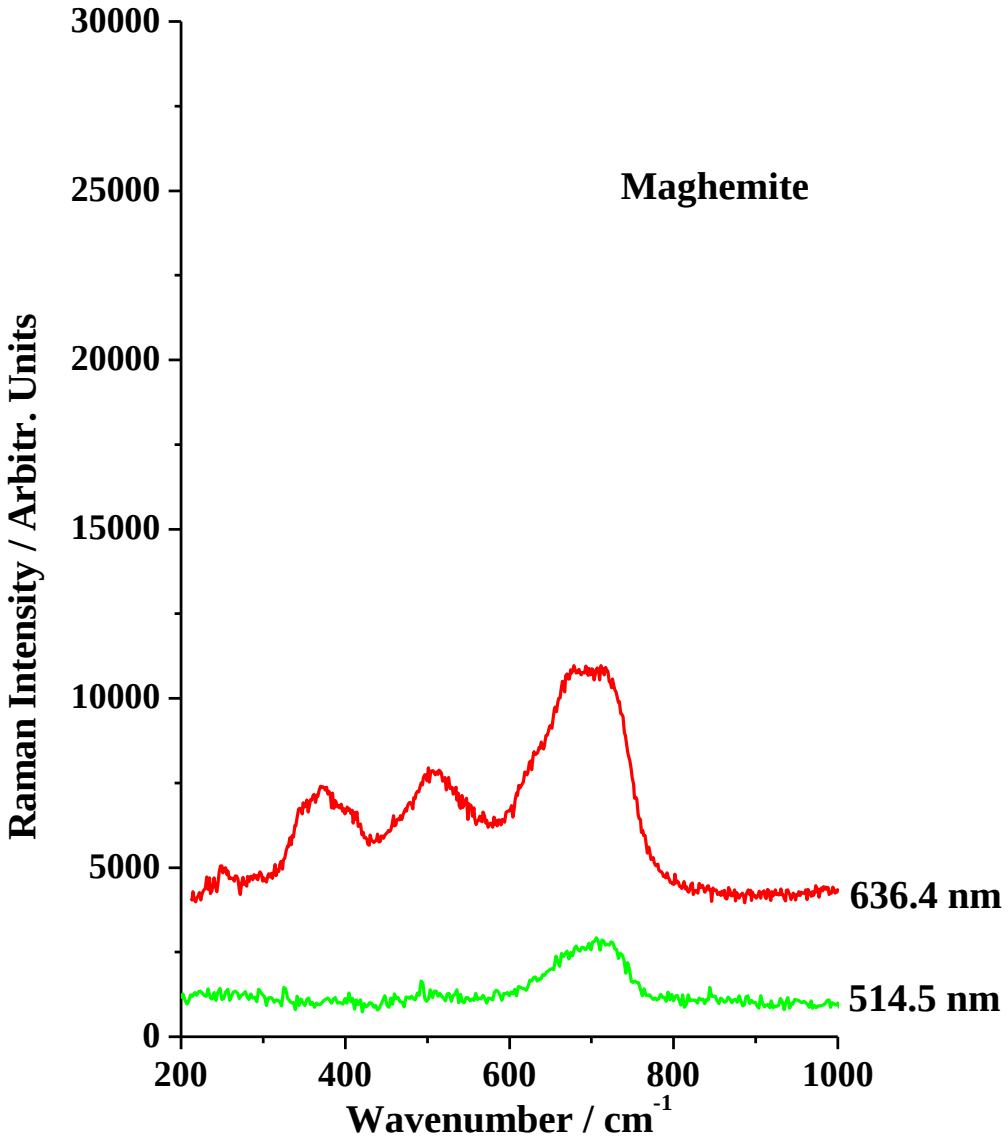


Figure 4.15. Standard Raman spectra of $\gamma$-$Fe_2O_3$ (maghemite) showing the variation in intensity with different excitation wavelengths: 636.4 nm at 15 mW (0.340 mW at the sample) and 240 s integration time, and 514.5 nm at 50 mW (0.340 mW at the sample) and 240 s integration time.

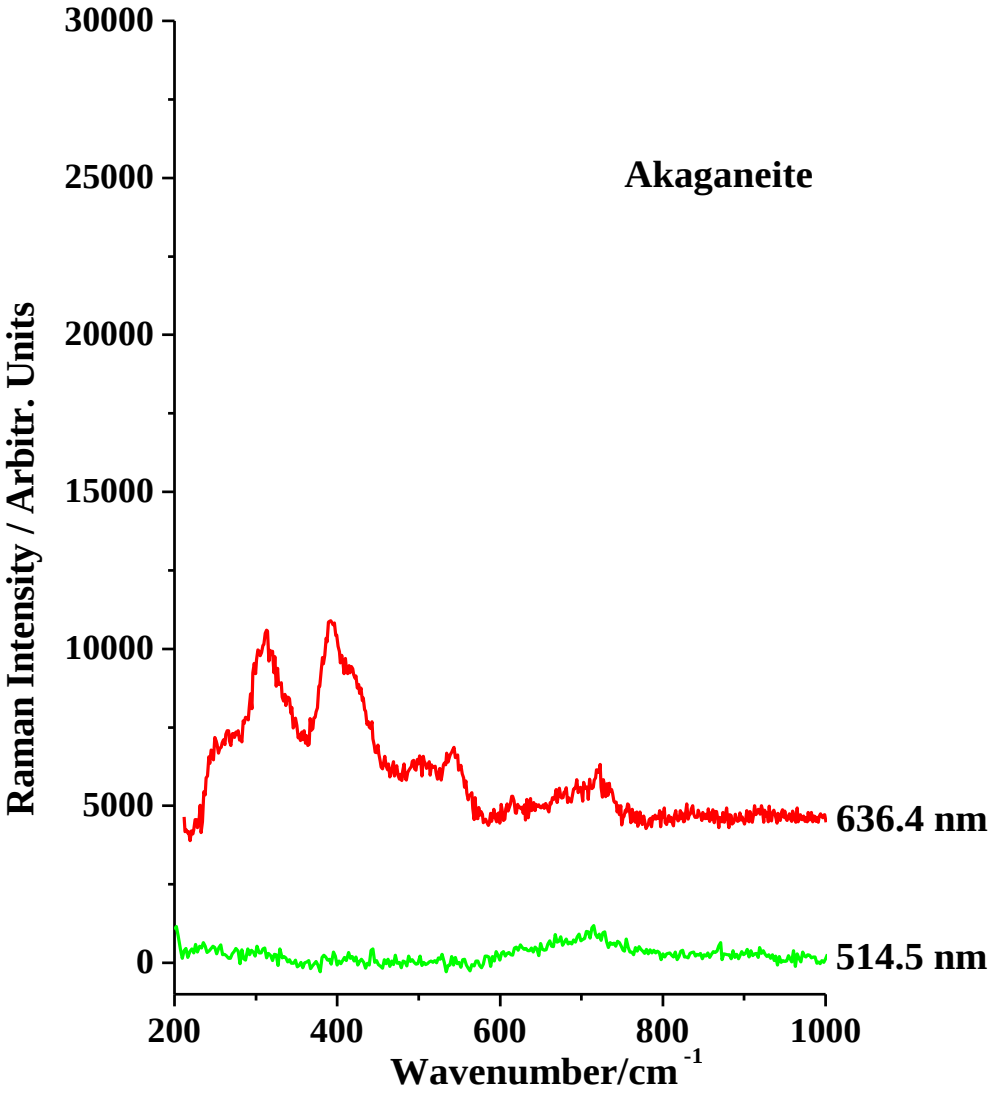


Figure 4.16. Standard Raman spectra of β-FeOOH (akaganeite) showing the variation in intensity with different excitation wavelengths: 636.4 nm at 15 mW (0.340 mW at the sample) and 240 s integration time, and 514.5 nm at 50 mW (0.340 mW at the sample) and 240 s integration time.

The peak positions of the major features displayed in the respective standard spectra (Figures 4.10 – 4.16) obtained with the 636.4 nm excitation are given in Table 4.1 and are in satisfactory agreement with results reported previously in the literature.

Table 4.1. Raman band positions and shoulders (sh) of iron oxide and oxyhydroxide standards in the region 200 – 1000 $cm^{-1}$ recorded with 636.4 nm excitation. Results obtained from work published in the literature have been included for comparison. The intense bands in spectrum are shown with their respective wavenumbers underlined.

| **Compound** | **Band positions / $cm^{-1}$** | **Reference** |
|---|---|---|
| α-FeOOH | *243, 300, 388, 417(sh), 482, 553* | *this study* |
| | 205, 247, 300, 386, 418, 481, 549 | 125 |
| | 205, 245, 300, 390, 415, 480, 550, 685 | 131 |
| β-FeOOH | *311, 390, 415, 537, 614, 717* | *this study* |
| | 310, 385, 415, 480, 535, 615, 675, 725 | 132 |
| | 310, 390, 535, 610, 720 | 130 |
| | 310, 390, 493, 538, 611, 718 | 133 |
| γ-FeOOH | *220, 250, 309, 350, 377, 527, 648* | *this study* |
| | 219, 252, 311, 349, 379, 528, 648 | 125 |
| | 214, 245, 301, 345, 373, 521, 644 | 134 |
| δ-FeOOH | *268, 401, 424,503, 676* | *this study* |
| | 400, 677 | 135 |
| | 296, 400, 678 | 136 |
| γ-$Fe_2O_3$ | *377, 510, 670 , 715* | *this study* |
| | 380, 460, 510, 670, 720 | 130 |
| | 381, 486 670, 718 | 125 |
| α-$Fe_2O_3$ | *228, 244, 296, 413, 497, 611, 659, 819* | *this study* |
| | 226, 245, 292, 411, 497, 612 | 120 |
| | 223, 240, 292, 412, 496, 610, 810 | 134 |
| $Fe_3O_4$ | *288, 532, 667* | *this study* |
| | 310, 540, 670 | 130 |
| | 297, 535, 661 | 134 |

The relative intensities of some of the peaks recorded with the 636.4 nm line are greater than those recorded with the 632.8 nm and 514.5 nm lines given in the literature. The observed spectral intensity increases are attributed to pre-resonance Raman enhancement being greatest in the present study with the 636.4 nm excitation. Absorption spectra have been recorded of the $Fe^{3+}$ iron oxide compounds γ-FeOOH, α-$Fe_2O_3$, γ-$Fe_2O_3$ and α–FeOOH [137] and a prominent absorption band was observed near 640 nm for these compounds, particularly for γ-FeOOH, α-$Fe_2O_3$ and α–FeOOH. This absorption band results from the $^6A_1(^6S) \rightarrow {}^4T_2(^4G)$ ligand field transitions of octahedrally coordinated $Fe^{3+}$, which are allowed and in fact strongly intensified by magnetic coupling of adjacent $Fe^{3+}$ cations in the crystal structures of these compounds [137]. However, for γ-$Fe_2O_3$ the band is poorly resolved and this is due to interference from $^6A_1(^6S) \rightarrow {}^4T_1(^4G)$ transitions of tetrahedrally coordinated $Fe^{3+}$ which also occur at this wavelength [137], and this may explain why a smaller enhancement is observed for γ-$Fe_2O_3$. The enhancement also occurs to a lesser extent for δ-FeOOH and β-FeOOH, even though the $Fe^{3+}$ ions are octahedrally coordinated. This may be due to a reduced magnetic coupling of $Fe^{3+}$ ions as a result of the packing arrangement of $Fe^{3+}$ in these compounds, or due to interference from $^6A_1(^6S) \rightarrow {}^4T_1(^4G)$ transitions of the tetrahedrally coordinated $Fe^{3+}$, as is the case for γ-$Fe_2O_3$.

## 4.4. CONCLUSIONS

The results presented emphasise the advantages and potential of near resonance Raman spectroscopy in radically improving the measurement sensitivity to the presence of a number of iron oxides and oxyhydroxides. The systematic variation of the excitation wavelength shows that within the constraints of the holographic notch filter used, a wavelength of 636.4 nm provides optimal enhancement of the scattering cross section. In most cases intense and well defined Raman peaks are produced, in stark contrast to the weak and indistinct spectra produced with the commonly used 514.5 nm excitation. In the context of *in situ* studies, the near resonance Raman technique with the resulting substantially enhanced spectral features reported in the present work offers a new opportunity to revisit the challenging problem of the passive layer composition formed on iron.

Part II of the investigation in Chapter 5 describes a micro-Raman investigation of the growth and composition of the passive film on iron at various stages during its growth by cyclic polarisation in a 0.05 M NaOH solution. Considerably higher laser powers at the wavelength of 636.4 nm could be used as compared with the present studies performed in air, since the heating effects of the laser beam were dissipated by the electrolyte flowing over the surface of the samples within a specially designed electrochemical cell. The results have permitted a re-evaluation of the sequence and relative concentrations of compounds forming the passive layer on iron.

# CHAPTER 5

# THE GROWTH OF THE PASSIVE FILM ON IRON IN 0.05 M NaOH STUDIED *IN SITU* BY RAMAN MICRO-SPECTROSCOPY AND ELECTROCHEMICAL POLARIZATION PART II: RAMAN SPECTRA OF THE PASSIVE FILM SURFACE DURING GROWTH BY ELECTROCHEMICAL POLARIZATION

*(Content published in Journal of Raman Spectroscopy [138])*

## 5.1. INTRODUCTION

This Chapter forms Part II of the investigation into the composition of the passive film on iron during its growth by electrochemical polarization in 0.05M NaOH. The study is primarily aimed at a better understanding of the composition of the passive film on iron, especially during its initial stages of growth by cyclic potentiodynamic polarization and particularly in the passive region.

In Part I in Chapter 4 it was shown that the intensity of Raman spectra for certain iron compounds, specifically α-$Fe_2O_3$ (hematite), γ-$Fe_2O_3$ (maghemite), α-FeOOH (goethite), β-FeOOH (akaganeite), δ-FeOOH (feroxyhyte), γ-FeOOH (lepidocrocite), and $Fe_3O_4$ (magnetite) can be significantly increased, particularly in the lower wavenumber region (<1000 $cm^{-1}$), by using the 636.4 nm excitation line produced by a tuneable dye laser. In the present study this excitation line has been used to record Raman spectra of the iron surface *in situ* at different potentials during the early stages of controlled growth of the passive film by potentiodynamic polarization in 0.05 M NaOH. The composition of the passive film was analysed in terms of the relative amounts of different iron oxide compounds determined by MCR-ALS (Multivariate Curve Resolution with Alternating Least Squares) This method has been described in detail in Section 3.4 of Chapter 3.

## 5.2. EXPERIMENTAL PROCEDURE

### 5.2.1. Potentiodynamic polarization

The three-electrode cell containing the polished iron surface as the Working Electrode was connected to a Bioanalytical Systems CV27 potentiostat, and positioned on the stage of the Olympus confocal microscope of the JY T64000 Raman spectrograph. The experimental details of the cell and potentiostat are described in Chapter 3.

For the *in situ* Raman study with electrochemical polarisation, 18 cycles of anodic and cathodic sweeps were applied to the iron surface at a scan rate of 10 mV/s between –1.20 and +0.67 V relative to the reference electrode. Prior to these cycles, the surface was polarized at –1.40 V for 20 minutes in 0.05 M NaOH to reduce the oxides formed on the iron surface in air and in solution. The electrolyte was not de-aerated. During the $1^{st}$, $2^{nd}$, $5^{th}$, $6^{th}$, $8^{th}$ and $15^{th}$ cycles the scan was interrupted at various selected potentials while Raman spectra of the iron surface were recorded. Due to the length of time required to record the *in situ* spectra, at the end of the $2^{nd}$, $10^{th}$ and $14^{th}$ cycles the iron electrode was removed, rinsed with de-ionised water and dried. Before resuming measurements the following day with *in situ* measurements the surface was once again polarized at –1.40 V for 20 minutes. No visible change was observed to occur on the surface on exposure to air overnight between these cycles, and any iron oxide compounds formed by exposure to air would be reduced by the cathodic polarisation at –1.40 V.

### 5.2.2. Raman microscopy

The operating parameters of the Jobin-Yvon T64000 Raman spectrograph, the Spectra-Physics (S-P) 171 argon ion pump laser, S-P 375/376 dye laser using R6G dye, holographic and interference filters used for the present studies were described in Chapter 3 and are identical to those for Chapter 4, except for the microscope objective and laser power. The surface of the iron sample within the electrochemical cell was analysed using a back-scattering geometry on the microscope stage of the Olympus confocal Raman microscope using a long working distance 20× objective. The laser power measured at the quartz window

surface of the electrochemical cell was 2 mW at the optimized wavelength of 636.4 nm, after passing through the external spectrograph and confocal microscope optics as well the 632.8 nm interference filter. The output beam power of the dye laser was 100-105 mW and was produced by a pump laser power of 7 W. The laser beam was focused to a spot size of 5 μm onto the surface of the iron sample in the cell. Refocusing of the laser beam on the surface was found to be necessary for each spectrum as the thickness of the passive film changed during each cycle and with increasing number of cycles. Heating of the iron surface was prevented by the cooling effect of the electrolyte continuously flowing over the surface. The spectral integration time was 130 s and two spectra were averaged for each measurement. A confocal pinhole of 0.1 mm was used to minimize Raman bands of the electrolyte and reflection from the surface of the sample.

The amount of water incorporated in the film during potentiodynamic polarization cycles in 0.05 M NaOH was determined from a separate experiment in which the iron surface was subjected to repeated polarization cycles under the same conditions of electrolyte, surface roughness and sweep rate. *In situ* spectra of the O-H stretch region were recorded during anodic polarization between 4300 and 2600 $cm^{-1}$ using the 514.5 nm excitation line of the Innova 308 Coherent Argon-ion laser. The laser output power was 800 mW and a 120s integration time was used. A 514.5 nm HNF filter was used to remove the Rayleigh scattered light and a 514.5 nm interference filter was used to remove unwanted laser plasma lines. The 514.5 nm excitation wavelength was found to afford better intensities for the O-H stretch modes than the 636.4 nm excitation line. Laser-induced heating of the surface was prevented by the continuous flow of electrolyte over the surface.

### 5.2.3. Multivariate Curve Resolution with Alternating Least Squares (MCR-ALS)

Determination of the relative amounts of iron compounds in the Raman spectra recorded during cycles 1, 8 and 15 was performed using the MCR-ALS toolbox of MATLAB [118]. These cycles represent initial, midway and final stages of the cyclic polarization, and contained spectra recorded at similar potentials in

the anodic region. The spectra recorded *in situ* were entered in a single data matrix *D*. The spectra of the six iron oxide and oxy-hydroxide powder samples were entered as pure component spectra profiles in a single matrix, $S^T$. These spectra were also included in the data matrix. The intensities of the spectra in both matrices *D* and $S^T$ had been adjusted to the same height for the 1562 $cm^{-1}$ peak and then truncated to the region 270 $cm^{-1}$ to 950 $cm^{-1}$. The $S^T$ matrix was constrained to remain invariant during the optimization. A further constraint which was applied was non-negativity for both concentration and spectra using the non-negative least squares option. No constraints of closure or normalization were applied.

## 5.3. RESULTS

### 5.3.1. Polarization curves of iron in 0.05 M NaOH

The polarization curves shown in Figure 5.1 are obtained from a selection from 12 repeated anodic and cathodic potential sweeps, namely the $1^{st}$ to $4^{th}$ , $6^{th}$, $8^{th}$, $10^{th}$ and $12^{th}$ cycles applied to the cell between –1.40 and +0.67 V in 0.05 M NaOH at a sweep rate of 10 mV/s.

The anodic sweep can be divided into two distinct regions: an active region between –1.40 and –0.55 V in which the current increases with potential and three current peaks (Peak I at –1.02 V, Peak II at –0.88 V and Peak III at –0.63 V with a shoulder, Peak III', at –0.55 V) are observed, and a passive region between –0.55 and +0.67 V during which the current initially falls sharply and remains at a very low value. At potentials more positive than +0.67 V, $O_2$(g) evolution occurs which accounts for the increase in current. In the return cathodic sweep, the surface remains passive between +0.67 and –0.60 V, but becomes active again at more negative potentials yielding Peak IV at –1.04 V with a shoulder Peak IV' at –0.88 V, and Peak V at –1.24 V.

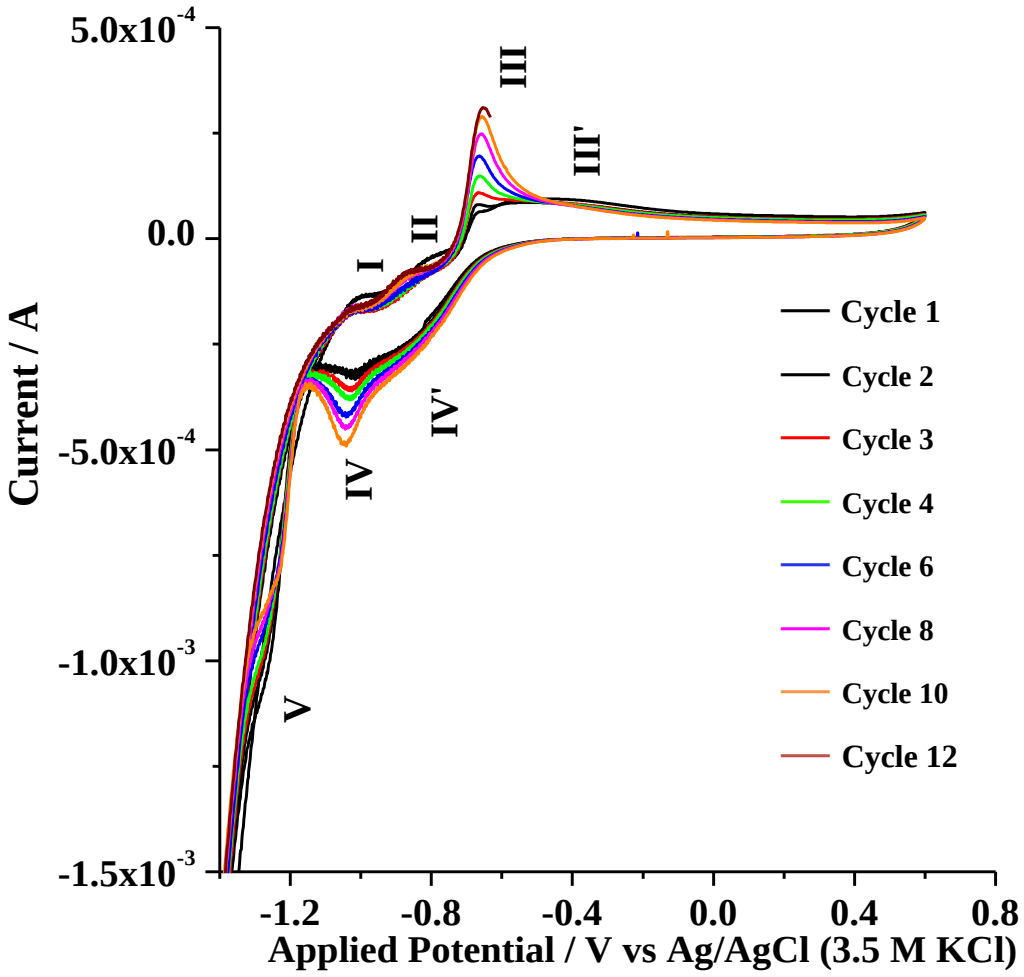


Figure 5.1. The 1st – 4th, 6th, 8th, 10th and 12th cycle of a series of 12 successive anodic and cathodic sweeps applied to the cell at 10 mV/s in 0.05 M NaOH between –1.4 V and +0.64 V. For processes assigned to the anodic and cathodic peaks see the text.

With increased cycling, Peaks II, III, IV and IV' were observed to increase, whereas Peak V decreased and shifted to more positive potentials. No increase occurred in Peak I, but the potentials of Peaks I and II were observed to shift to higher values after the first cycle. Growth in the surface layer with increased cycling was indicated by increases in the peak intensities. After about five cycles the surface became visibly darker, starting at a potential just after Peak III' and throughout the passive region of the anodic and cathodic sweeps. The surface

returned to a lighter and shiny appearance again above the Peak IV potential on the cathodic sweeps as the surface layer was reduced.

From potentiodynamic studies of iron in alkaline solutions [16,23,24,40,94,123,124] the following reactions have been proposed to occur at the peaks in the anodic sweep.

**Peak I:**

$Fe \rightarrow Fe(OH)_2$ [22,24,40,94] via $[Fe(OH)]_{ad}$ and $[Fe(OH)]_{ad}^{+}$ as intermediates, [22] and $Fe \rightarrow Fe_3O_4$ [16,24,40,123,124] via either $3Fe + 8OH^{-} \rightarrow Fe_3O_4 + 4H_2O + 8e^{-}$, [123] or $Fe^{2+} + 2FeOOH \rightarrow Fe_3O_4 + 4H^{+}$ [124].

**Peak II:**

$Fe \rightarrow FeOOH$ and $Fe(OH)_2 \rightarrow FeOOH$ [24]

$Fe(OH)_2 \rightarrow \alpha\text{-}FeOOH$ [40]

$Fe(OH)_2 \rightarrow Fe_3O_4$ [40,94]

$Fe_3O_4 \rightarrow FeOOH$ [40]

$Fe \rightarrow Fe(OH)_2$ [22,24,40] via $Fe_s\{Fe(OH)_2\} \rightarrow 2Fe(OH)_2$.oxide phase [22] (where $Fe_s$ = Fe substrate atom; these are both intermediate phases and may undergo dehydration to $HFeO_2^{-}$ and $HFeO_2^{2-}$).

**Peaks III and III':**

$Fe(OH)_2 \rightarrow \delta\text{-}FeOOH$ [40]

$Fe(OH)_2 \rightarrow FeOOH$ [16,22,94] via $Fe(OH)_2 + OH^{-} \rightarrow FeOOH + H_2O + e^{-}$ and $FeOOH + FeOOH \rightarrow Fe_2O_3 \cdot H_2O$ [22]

Also, $Fe(OH)_2 \rightarrow Fe_3O_4$, [40] $Fe_3O_4 \rightarrow FeOOH$ [94] and $Fe \rightarrow FeOOH$ [24].

**Passive region**: On further increasing the anodic potential into the passive region, starting from –0.52 V, no further peaks are visible and the steady, low background current has been attributed to the formation of FeOOH from $Fe_3O_4$ [24] and finally ageing of FeOOH to $Fe_3O_4$ [22] (possibly involving reactions such as conversion of δ-FeOOH to α-FeOOH and α-FeOOH to $Fe_3O_4$) and to hydrated $Fe_2O_3$ [22]. α-, or δ- and β- forms of FeOOH have been detected in this region [94].

The following reactions have been proposed for the cathodic sweep:

**Peaks IV and IV'**: the reverse reactions of those occurring at Peaks III and III'.

**Peak V:** $Fe_3O_4 \rightarrow Fe(OH)_2$ [40,94] and electro-reduction of species containing $Fe(OH)_2$ [22] occurs. Reduction of $Fe(OH)_2$ to Fe is also possible [40]; however, it is

believed that after the first cycle the surface is not completely reduced back to Fe, but covered with a residual oxide or hydroxide layer [16] or a thin adherent layer of $Fe_3O_4$ [24].

From sweep reversal studies [22] it was shown that the product formed at peaks I and II are reduced at Peak V and the product formed at peak III is reduced at Peak IV. From the change in ratio of the currents at Peak II / Peak III with increasing sweep rate it was also shown that the above reactions do not follow a strictly sequential mechanism; instead a sequential/parallel reaction path was suggested [22].

The complex and inter-related nature of the proposed reactions above corresponding to the characteristic current peaks formed during the anodic and cathodic sweeps demonstrates the need to obtain corroborative Raman spectra not only over a single potentiodynamic cycle, but over a significant number of cycles in order to obtain a comprehensive picture of the compositional changes in the near-surface region.

### 5.3.2. Polarization of iron in 0.05 M NaOH with *in situ* Raman spectroscopy

In the *in situ* experiments, 18 cycles of anodic and cathodic sweeps were performed while Raman spectra were recorded at selected potentials during some of these cycles, the respective sweeps being interrupted for the period of each measurement.

The spectra obtained at the different potentials held during the 1$^{st}$ cycle are shown in Figure 5.2.

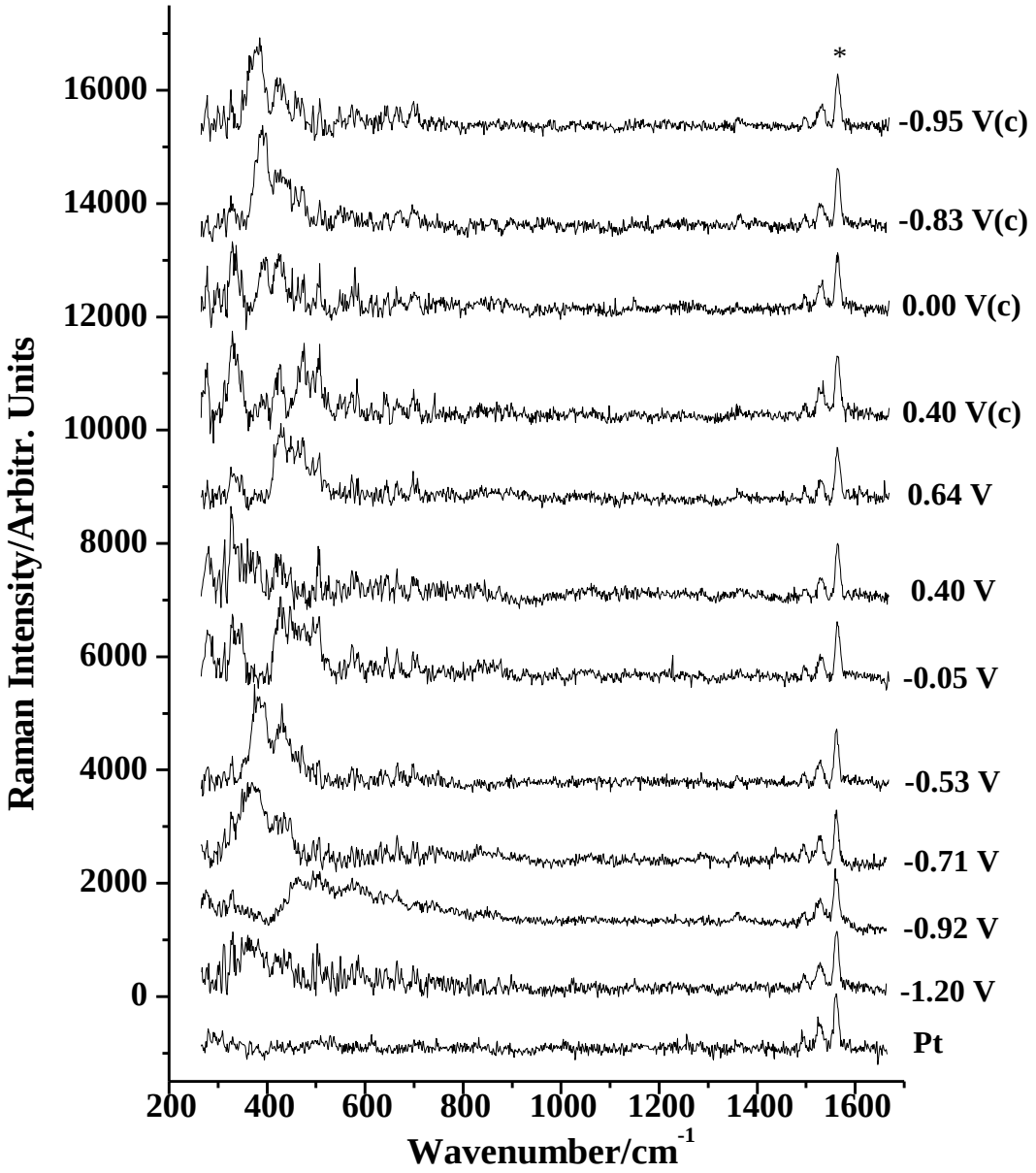


Figure 5.2. *In situ* Raman spectra recorded of the iron surface at various potentials during the 1st anodic and cathodic sweeps (marked with (c)), after adjusting of intensities to the same height for the 1562 $cm^{-1}$ peak (marked with *). A spectrum of the Pt counter electrode (bottom spectrum) is shown in order to check that no significant Raman bands are recorded from the NaOH electrolyte. All the spectra were truncated in the region 270 to 950 $cm^{-1}$ for MCR-ALS optimization. Recorded using 636.4 nm excitation at 105 mW (2 mW at the sample) and 130 s integration time.

A steeply rising baseline was observed in the experimental spectra that arose from reflection by the metal surface, and depended on the angle of the HNF. This baseline was fitted using the polynomial fitting function of the Grams5 spectroscopic software (Galactic Industries) individually for each spectrum and subtracted. A spectrum of the Pt counter electrode surface is included (bottom spectrum) which was recorded in the cell to check for peaks from the NaOH electrolyte; no significant bands are present in the range 250 to 1400 $cm^{-1}$.

Considerable variation in the Raman spectra as a function of the applied potential is observed in the lower wavenumber regions corresponding to the spectral signatures of the respective iron oxides and hydroxides examined in Part I (Chapter 4). The presence of bands in the spectrum recorded at –1.20 V indicates that compounds had already formed on the surface. In this context, it was not possible to record spectra at –1.40 V as the surface was covered with $H_2$(g) bubbles; such was the case for all potentiometric polarization cycles at this potential; for this reason the potential was not reduced to below -1.20 V for any of the different cycles for recording of the *in situ* spectra.

The three instrumentally-induced bands at 1498 $cm^{-1}$, 1530 $cm^{-1}$ and 1562 $cm^{-1}$ whose properties were discussed in Part I (Chapter 4, section 4.3) are observed in all the spectra. Since the dye laser excitation wavelength was observed to shift slightly to lower wavelengths over time, probably due to some gradual heating of the dye by the pump laser, the strongest peak at 1562 $cm^{-1}$ was used for calibrating the spectra. The wavelength stability of the dye laser was sensitively monitored by any variation in the measured wavenumber of the strongest peak, being at 1562 $cm^{-1}$ for excitation at 636.4 nm (see Figure 4.9). Great care was taken to ensure that the wavelength was tuned to exactly 636.4 nm for every spectrum: measurements before and after each spectrum were recorded, as well as the position of the instrumental peak at 1562 $cm^{-1}$. The intensity of the 1562 $cm^{-1}$ peak was also found to be useful as an internal standard: the intensities of the three instrumental peaks were found to increase with integration time and were found to be nearly constant for the same integration time at the same laser power, as given in Figures 5.3 and 5.4.

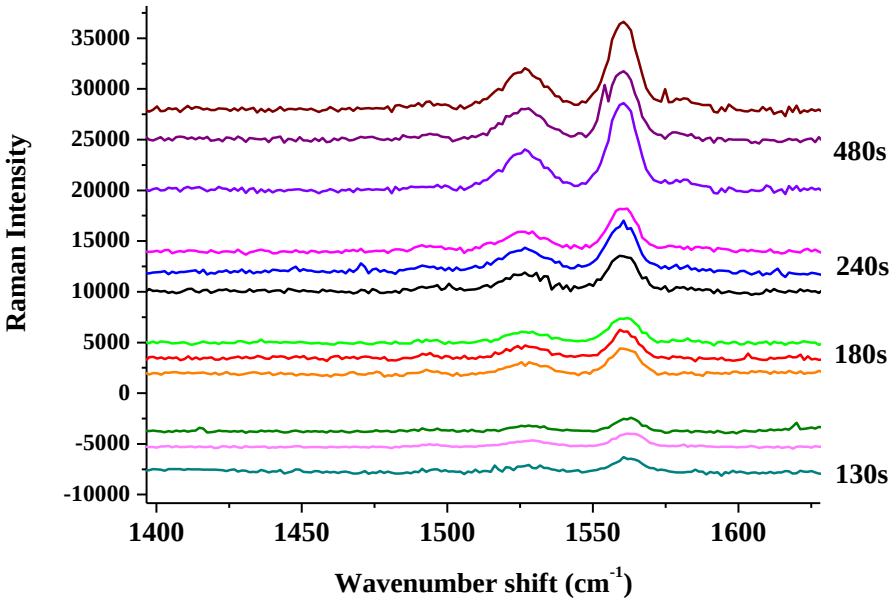


Figure 5.3. Variation of the height of the instrumental peak at 1562 $cm^{-1}$ with integration time. The laser power was 100 – 105 mW, the confocal pinhole had diameter 0.1 mm and the slit width was 200 µm. The data reflect three independent runs. The individual spectra for each time period have been displaced for reasons of clarity.

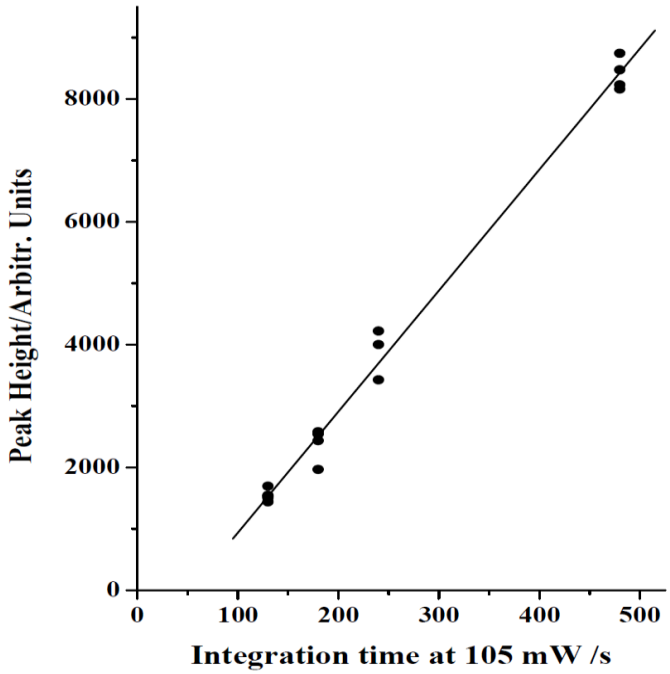


Figure 5.4 Plot of peak height vs integration time of the peak at 1562 $cm^{-1}$ observed in the respective Raman spectra given in Figure 5.3. The 1562 $cm^{-1}$ peak was used as a wavelength and intensity standard.

Since the intensity of the instrumental peaks increased with increasing laser power, they were used to adjust the measured spectral intensities for any variation in laser power which may have occurred in the recording of the different spectra *in situ*. This was achieved by adjusting the spectral intensities of all the spectra so that the 1562 $cm^{-1}$ peak was the same height for each spectrum.

Although the data included the triplet of instrumental peaks used to normalize the spectra as discussed above, they were truncated between 270 and 950 $cm^{-1}$ for the MCR-ALS optimization. It is emphasised that in every Raman spectrum the instrumental bands were present and used. They were not shown in the truncated spectra shown in the thesis in order to advantageously present the Raman peaks from the iron oxides that were actually used after normalisation in the MCR-ALS analysis.

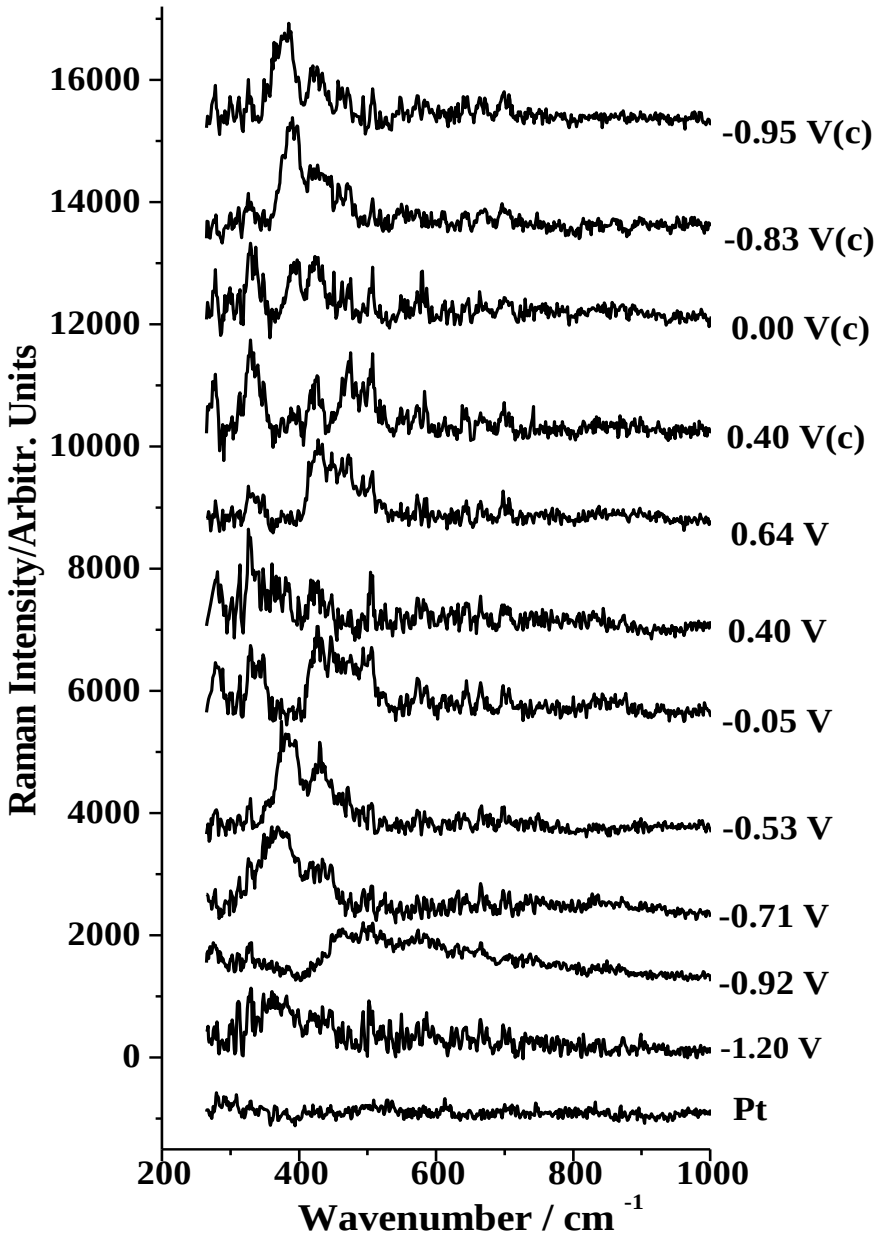


Figure 5.5. *In situ* Raman spectra recorded of the iron surface at various potentials during the 1st anodic and cathodic (c) sweeps. These were truncated in the region 270 to 950 $cm^{-1}$ for MCR-ALS optimization. Recorded using 636.4 nm excitation at 105 mW (2 mW at the sample) and 130 s integration time.

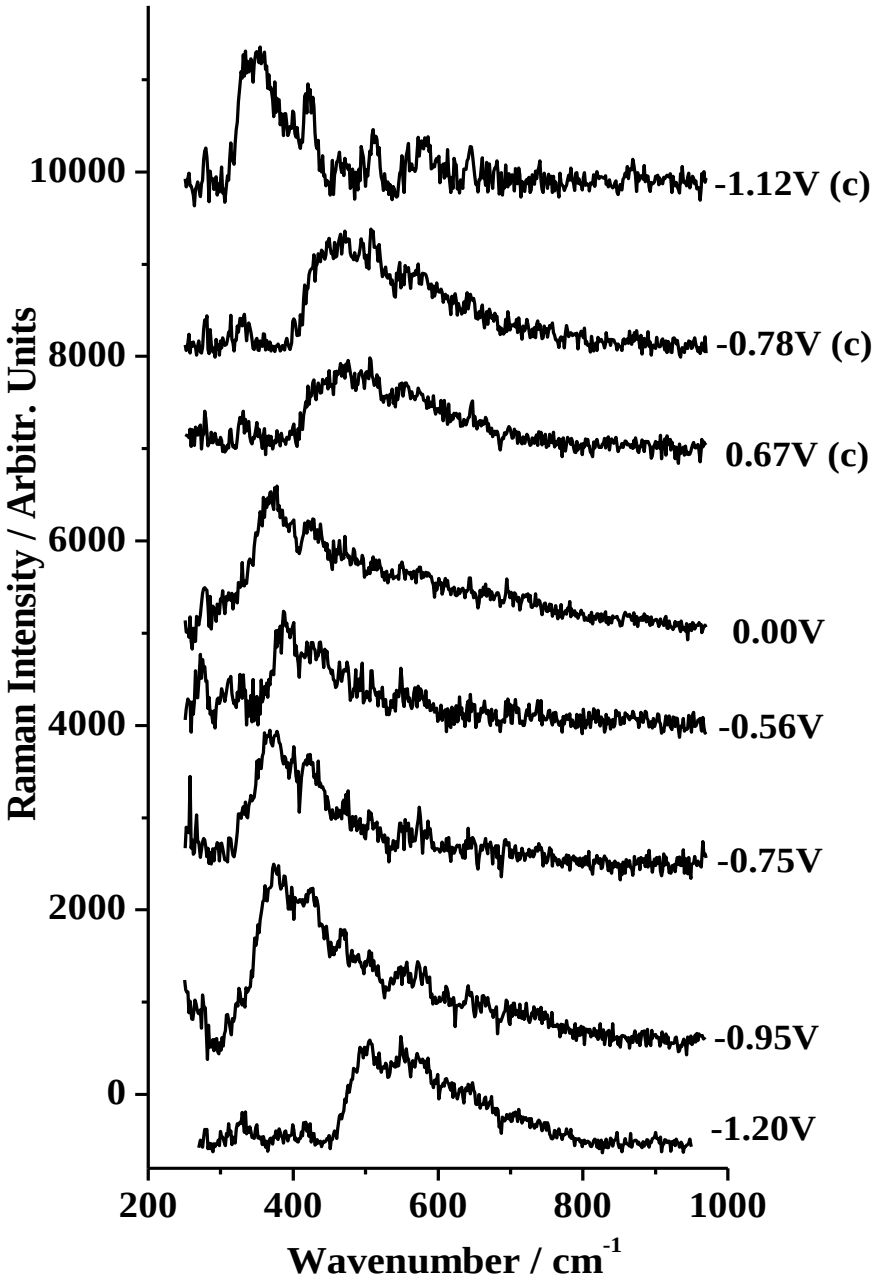


Figure 5.6. *In situ* Raman spectra recorded of the iron surface at various potentials during the 8$^{th}$ anodic and cathodic (c) sweeps. These were truncated in the region 270 to 950 cm$^{-1}$ for MCR-ALS optimization. Recorded using 636.4 nm excitation at 105 mW (2 mW at the sample) and 130 s integration time.

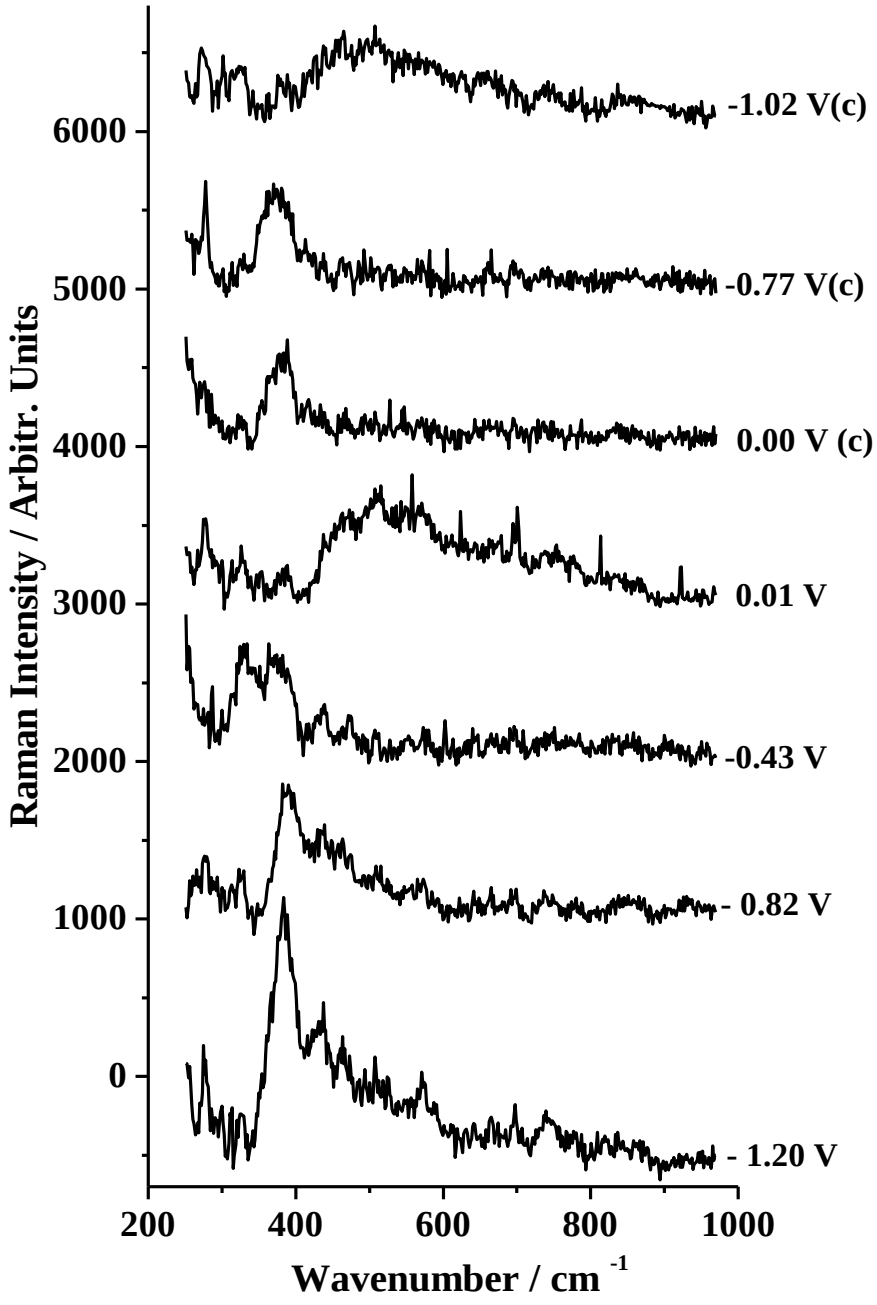


Figure 5.7. *In situ* Raman spectra recorded of the iron surface at various potentials during the 15th anodic and cathodic (c) sweeps. These were truncated in the region 270 to 950 $cm^{-1}$ for MCR-ALS optimization. Recorded using 636.4 nm excitation at 105 mW (2 mW at the sample) and 130 s integration time.

The bands are relatively weak and broad, but it is clear from the spectra that more than one compound is present on the surface. The bands change as the potential is changed, but at similar potentials the spectra also show some differences between cycles, indicating that changes occur in the composition of the surface at different potentials and with increasing number of cycles. The spectra recorded at different potentials during the cathodic and anodic sweeps of the $2^{nd}$, $5^{th}$, $6^{th}$, and $18^{th}$ cycles are given in Figures 5.8 and 5.9.

The spectra of powder samples of iron oxide and oxy-hydroxide previously identified in the passive film on iron in alkaline solutions: α-$Fe_2O_3$ (hematite), γ-FeOOH (lepidocrocite), α-FeOOH (goethite), β-FeOOH (akaganeite), γ-$Fe_2O_3$ (maghemite), δ-FeOOH (feroxyhyte) and $Fe_3O_4$ (magnetite), were used to characterize the compounds present on the surface. β-FeOOH was not included as it is known to form only in the presence of chloride ions [139]. These spectra had been recorded under the spectrometer conditions described in Part 1, Chapter 4.

The intensities of these spectra were adjusted to give the same height for the 1562 $cm^{-1}$ peak and are shown in overlaid format in Figure 5.10 to emphasize how the band intensities for the different oxides differ significantly relative to each other when recorded under the same integration time and laser power, as well as the extent of overlap of the major bands.

The overlaid format also indicates the extensive overlap of the bands of the different oxide compounds, which makes it difficult to distinguish them in a multi-component spectrum. The overlap of the bands also merits the use of MCR-ALS analysis for estimation of the relative amounts of these components from the spectra recorded *in situ*.

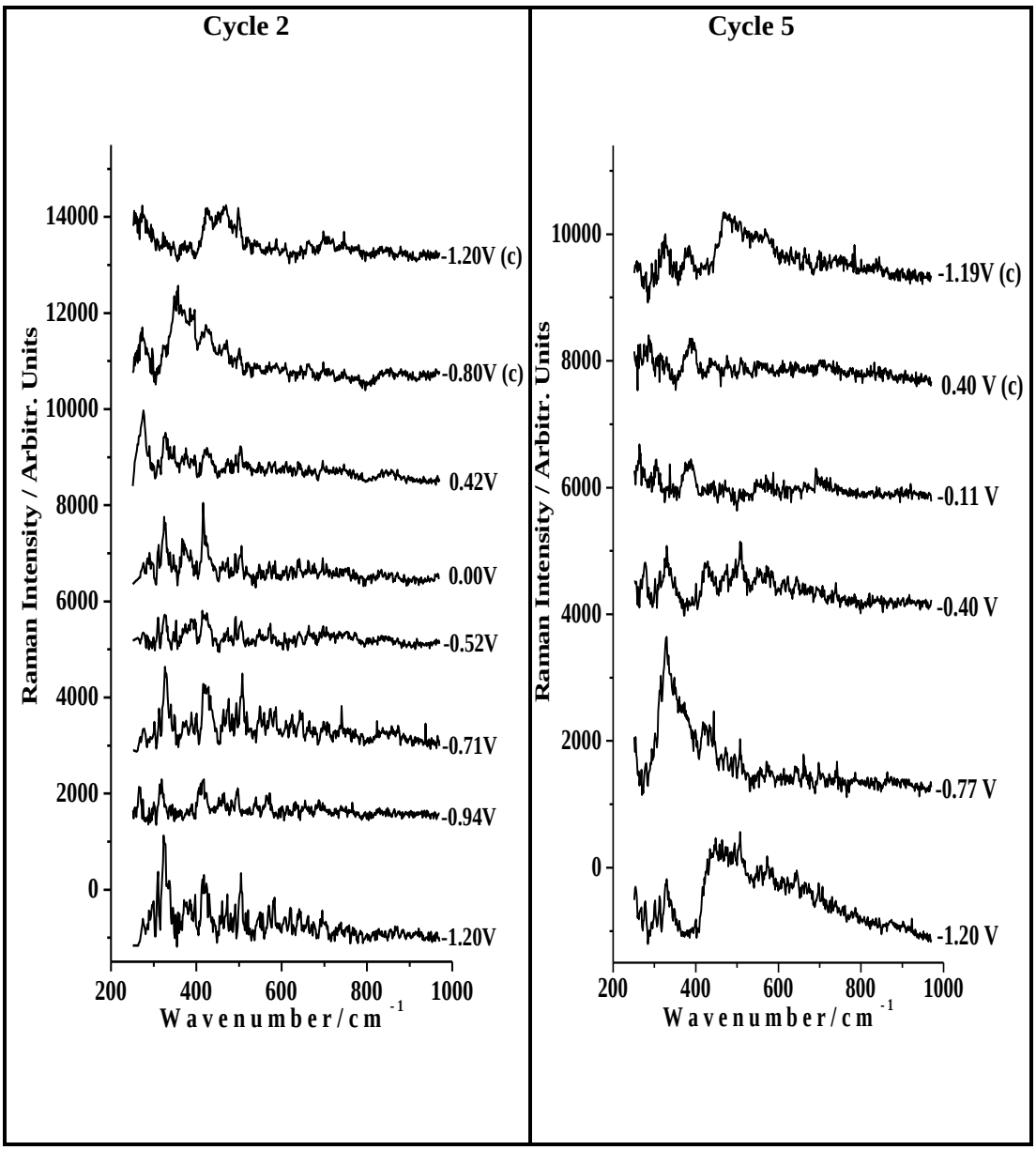


Figure 5.8. *In situ* Raman spectra recorded of the iron surface at various potentials during the 2nd and 5th anodic and cathodic (c) sweeps. These were truncated in the region 270 $cm^{-1}$ to 950 $cm^{-1}$ for MCR-ALS optimization. Recorded using 636.4 nm excitation at 105 mW (2 mW at the sample) and 130 s integration time.

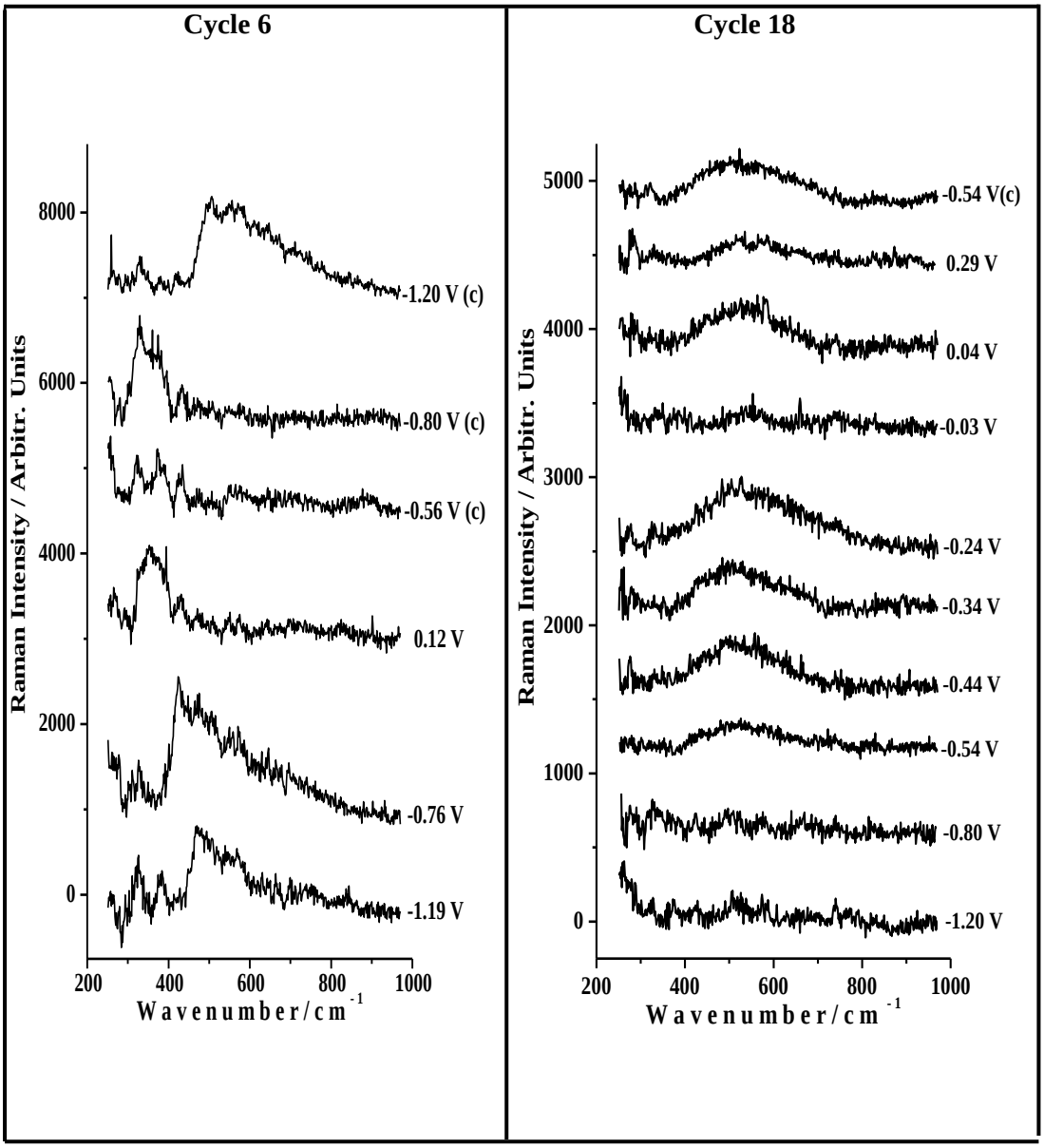


Figure 5.9. *In situ* Raman spectra recorded of the iron surface at various potentials during the 6$^{th}$ and 18$^{th}$ anodic and cathodic (c) sweeps. These were truncated in the region 270 cm$^{-1}$ to 950 cm$^{-1}$ for MCR-ALS optimization. Recorded using 636.4 nm excitation at 105 mW (2 mW at the sample) and 130 s integration time.

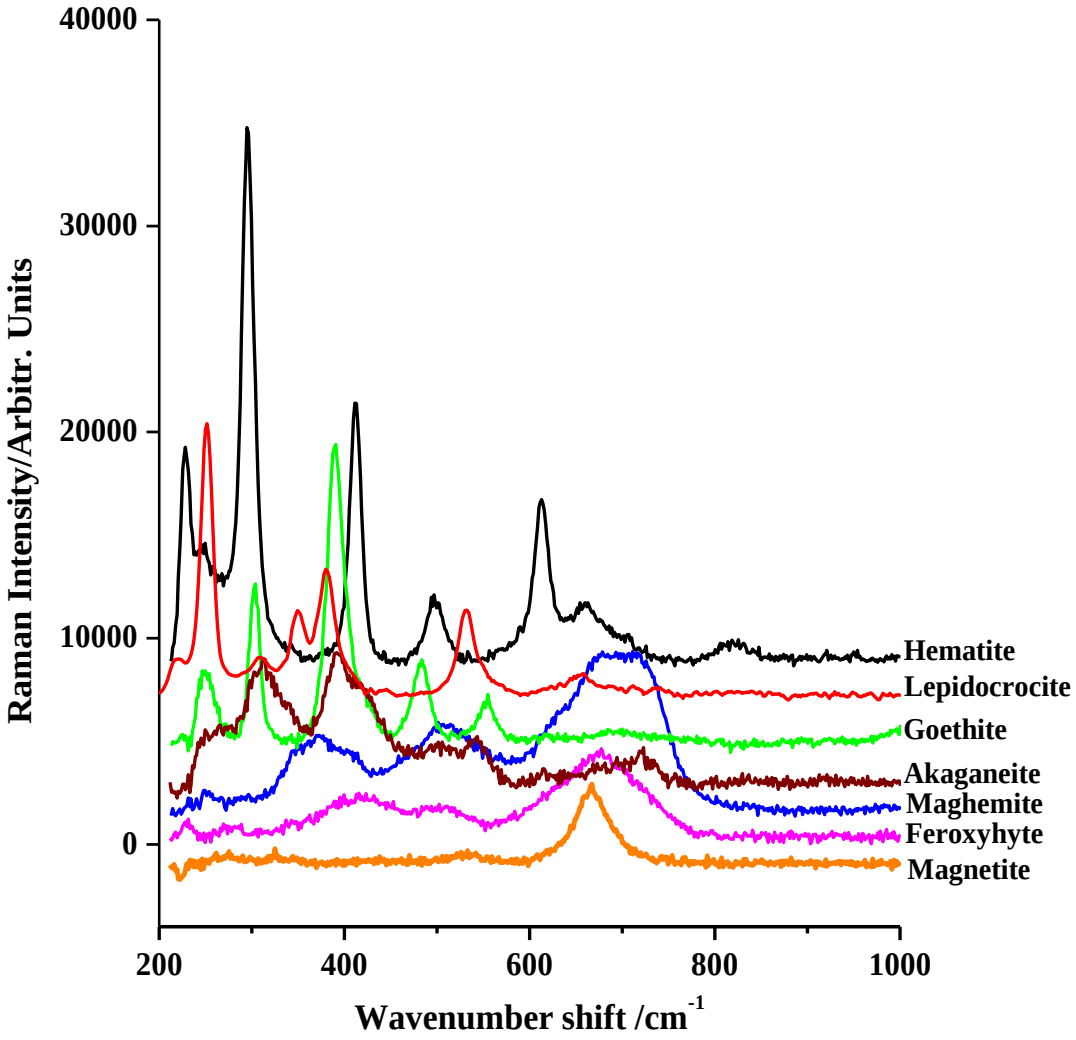


Figure 5.10. Raman spectra of the iron oxides and oxyhydroxides adjusted in intensity to the same height for the 1562 $cm^{-1}$, obtained using an excitation wavelength of 636.4 nm. Recorded using 636.4 nm excitation at 15 mW (0.340 mW at the sample) and 240 s integration time.

The lack of fit obtained for the MCR-ALS optimization was 20 %, which indicates that other components are present in significant amounts besides the set of compounds identified in Part I, Chapter 4, namely $Fe_3O_4$, α-$Fe_2O_3$, γ-$Fe_2O_3$, α-FeOOH, δ-FeOOH and γ-FeOOH used in the analysis. A further contributory factor to the lack of fit would be the relatively low signal-to-noise ratio of the Raman spectra, in spite of the pre-resonance enhancement. Notwithstanding the absence of other probable or possible components in the optimization, valuable

insights into the composition of the passive film can be gained from an estimation of the relative amounts of the six well known iron oxide compounds which were included in the fit, and which have been considered as components of the passive film on iron. The concentration profiles obtained from the optimization are not absolute, but provide the relative amounts of the components in each *in situ* spectrum.

Accordingly comparison of the relative amounts of γ-$Fe_2O_3$, α-FeOOH, δ-FeOOH and γ-FeOOH estimated from the MCR-ALS analysis at different stages during passive film growth are given in Figure 5.11, 5.12 and 5.13, for the 1st, 8th and 15th cycles, respectively. After the 15th cycle the spectra became very weak and broad, as shown for cycle 18 in Figure 5.9. Estimates of the error bars for the concentration plots given in these figures were made by calculating the Lack of Fit (LOF) for each spectrum using the formula for LOF (described in Chapter 3 Section 3.4) and multiplying it by the summed relative amounts of the components for each spectrum (as determined by the Optimized Concentration (COPT) output of the optimization (described in Appendix 2)) in order to convert

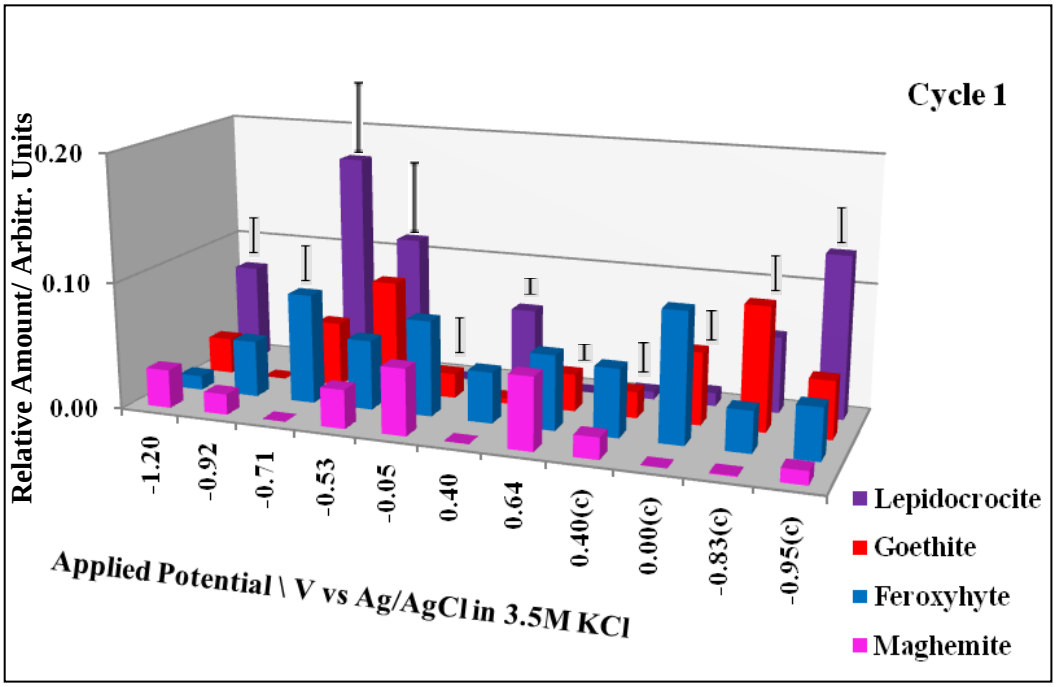


Figure 5.11. Relative amounts of γ-FeOOH (lepidocrocite), α-FeOOH (goethite), δ-FeOOH (feroxyhyte), and γ-$Fe_2O_3$ (maghemite) in the passive film during anodic and cathodic sweeps at the first stage of growth (Cycle 1) determined using MCR-ALS optimization from Raman spectra recorded *in situ*.

the LOF to a concentration value that can be plotted in the figure. This estimate in effect scales the summed amounts of the components (which would be a number less than 1) by the LOF (which gives an indication of the goodness of fit).

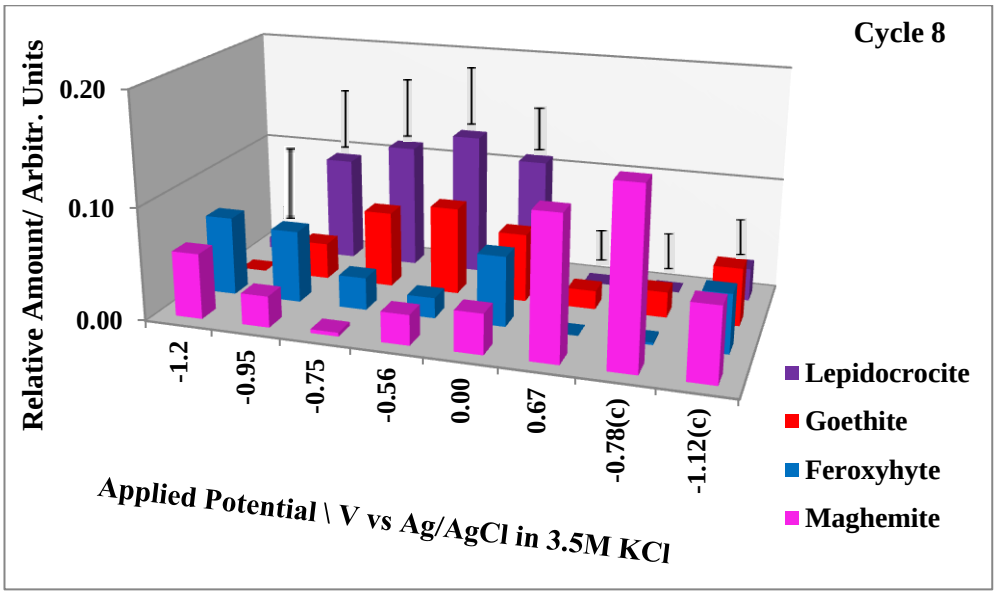


Figure 5.12. Relative amounts of γ -FeOOH (lepidocrocite), α-FeOOH (goethite), δ-FeOOH (feroxyhyte) and γ -$Fe_2O_3$(maghemite) in the passive film in further growth (Cycle 8) determined using MCR-ALS optimization from Raman spectra recorded *in situ*.

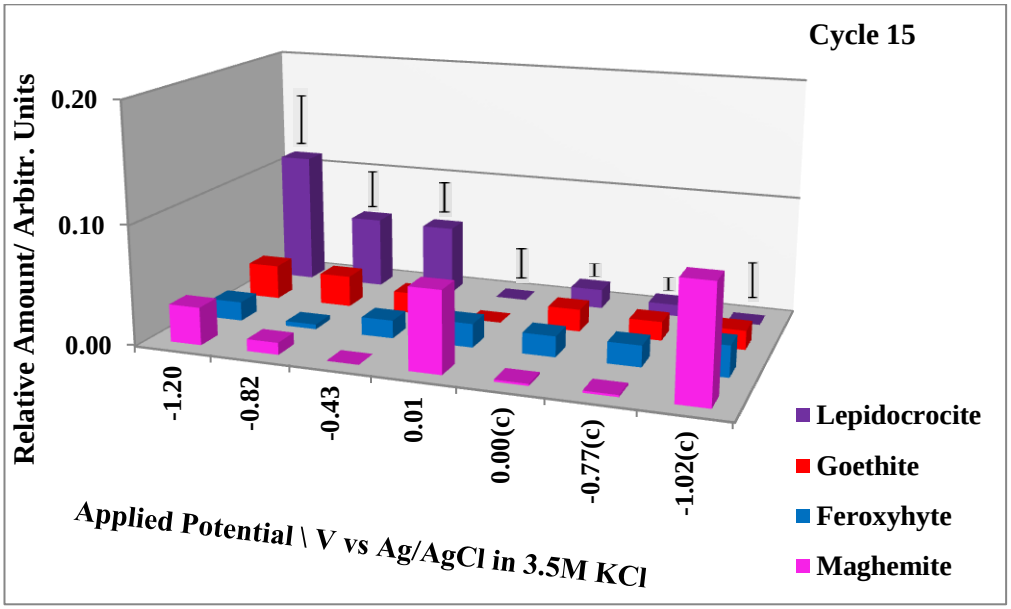


Figure 5.13. Relative amounts of γ-FeOOH (lepidocrocite), α-FeOOH (goethite), δ-FeOOH (feroxyhyte) and γ -$Fe_2O_3$(maghemite) in the passive film at a late stage of growth (Cycle 15) determined using MCR-ALS optimization from Raman spectra recorded *in situ.*

Figure 5.14 shows how the relative amounts of γ-$Fe_2O_3$, α-FeOOH, δ-FeOOH and γ-FeOOH vary for the different cycles at similar potentials: near the start of the anodic sweeps at -1.20 V, at Peaks II and III at -0.70 to -0.80 V, after Peak III' at the start of the anodic passive region at -0.50 V and extending to -0.40 V and well into the passive region at around 0.00 V.

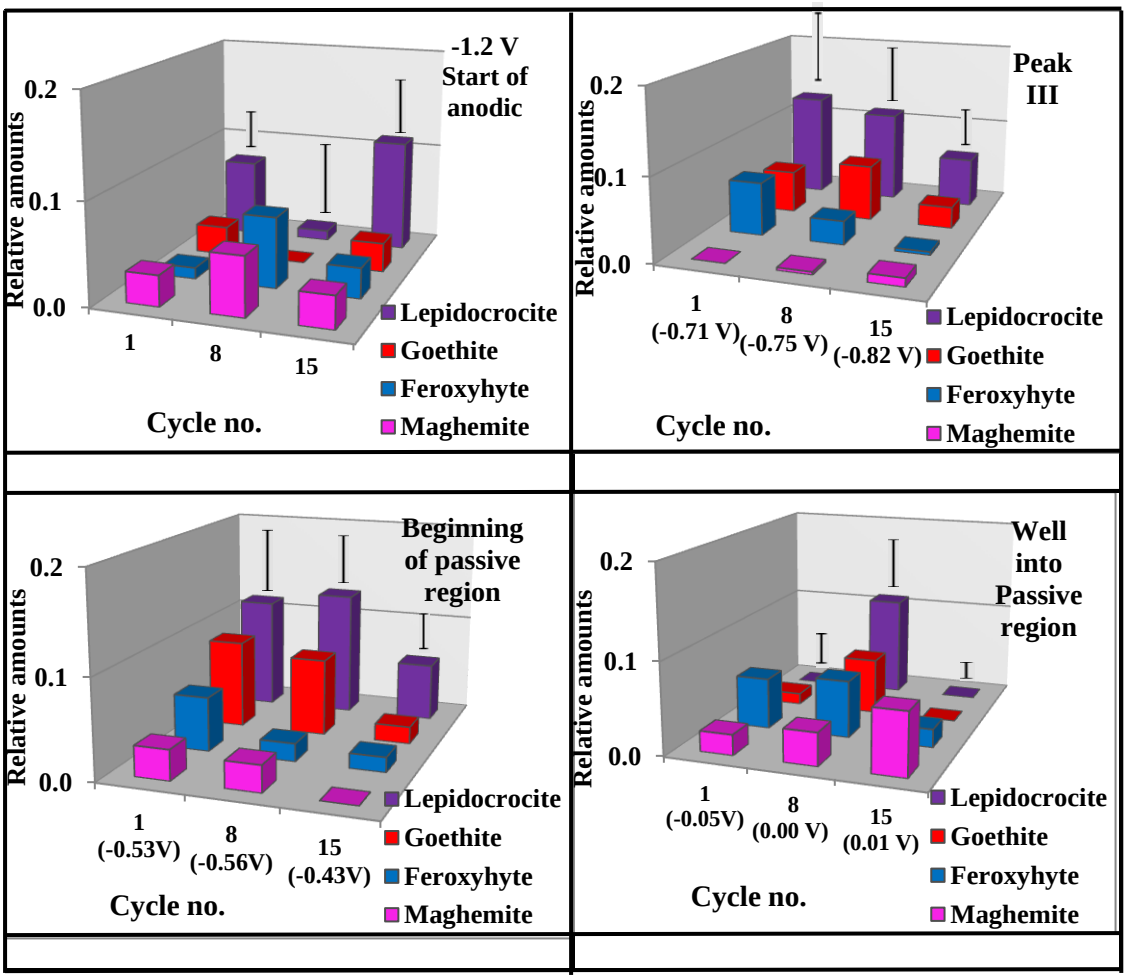


Figure 5.14. Relative amounts of γ -FeOOH (lepidocrocite), α-FeOOH (goethite), δ-FeOOH (feroxyhyte) and γ-$Fe_2O_3$ (maghemite) determined at four different potential regions during the anodic sweep for cycles 1, 8 and 15 using MCR-ALS optimization of the Raman spectra recorded *in situ*.

Examples of *in situ* spectra from cycles 1, 8 and 15 showing the component spectra fitted by the MCR-ALS optimization are given in Figure 5.15, along with their residual spectra.

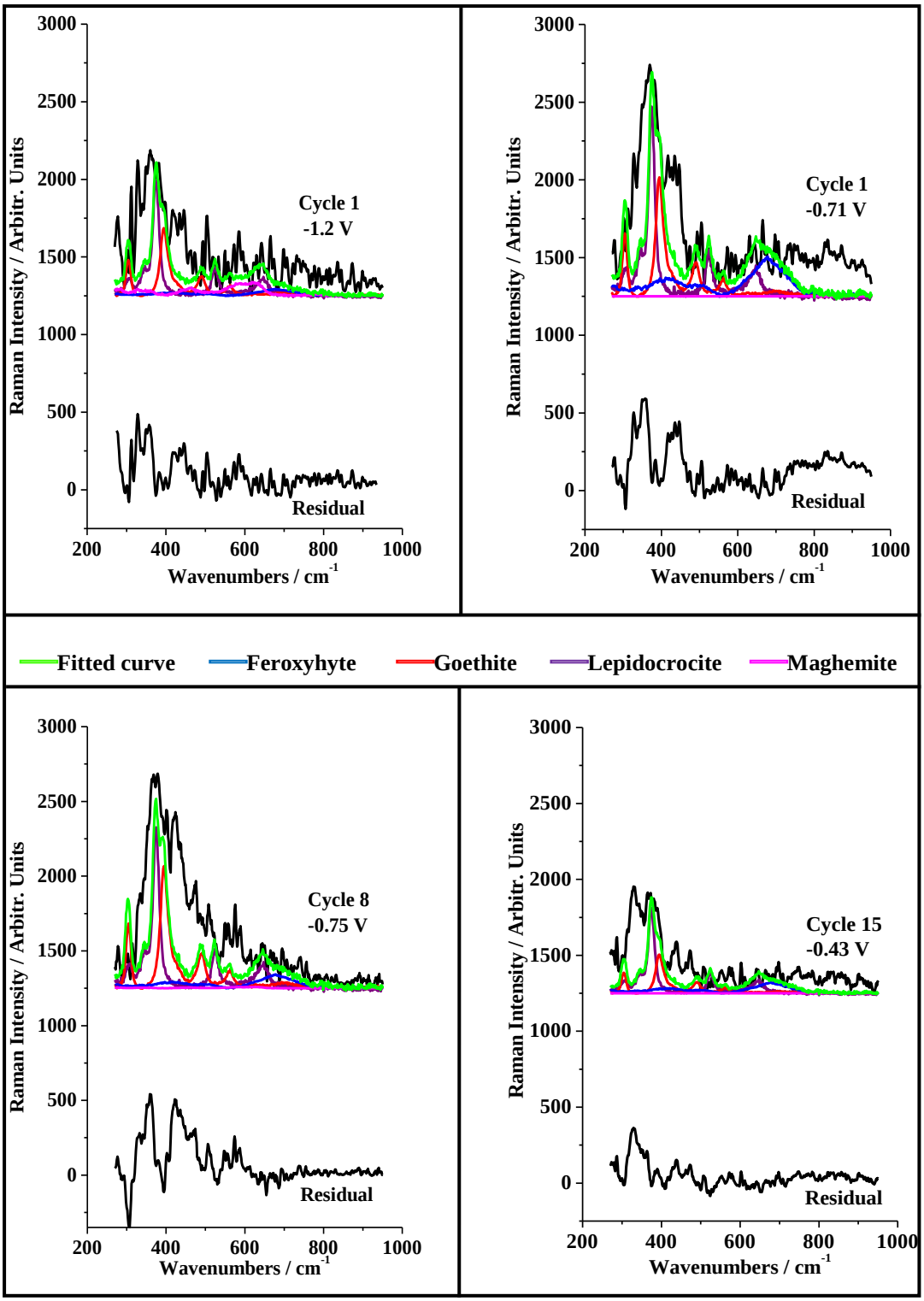


Figure 5.15. Examples of the MCR-ALS optimized fits for spectra recorded *in situ* from cycles 1, 8 and 15, showing the fitted component spectra for γ-FeOOH (lepidocrocite), α-FeOOH (goethite), δ-FeOOH (feroxyhyte) and γ-$Fe_2O_3$ (maghemite), and the residual spectra for each. The green spectra represent the sum of the components.

It is noted that the fitting procedures employed in the MCR-ALS analysis did not reveal $Fe_3O_4$ or $\alpha$-$Fe_2O_3$ being present in significant amounts and these components are not included in these figures, nor in the figures showing the relative amounts of each component at various stages in the cyclic polarization process.

The residual spectra comprise noise and also bands due to any other iron oxide compounds not included in the set of iron oxide components used for the optimization (hematite, lepidocrocite, goethite, akaganeite, feroxyhyte, maghemite and magnetite). The residual spectra provided by the MCR-ALS optimizations given in Figure 5.15 have been given together in Figure 5.16 and all show similar residual bands between 330 - 350, 410 - 470, 510 - 550 and 570 - 580 $cm^{-1}$. The bands between 410 and 470 $cm^{-1}$ and 510 and 550 $cm^{-1}$ in particular suggest that one of the major components in the residual spectra is $Fe(OH)_2$. In its pure form $Fe(OH)_2$ has a characteristic band at 407 $cm^{-1}$ due to the $A_{1g}$ lattice vibration [140], which with partial oxidation in aerated solution would undergo a red shift as has been observed for the $A_{2u}$ IR-active mode [140]. $Fe(OH)_2$ in solution has been reported to have bands at 460 and 550 $cm^{-1}$ [125], 544 $cm^{-1}$ [141] and 550 $cm^{-1}$ [16] and band components visible in the two regions corresponding with these values have been marked on the spectra. The bands between 310 – 350 and 580 – 610 $cm^{-1}$ are unassigned. However, these may be due to other $Fe(OH)_3$ and intermediate complexes which may form as a result of solid state reactions during the slow oxidation of $Fe(OH)_2$ [14,23,45,85]. It is unlikely that the residual bands would contain contributions from $\beta$-FeOOH which has bands at 311, 390, 415, 537 and 614 $cm^{-1}$. It is possible for $\beta$-FeOOH to form when significant diffusion of chloride ions from the Ag/AgCl reference electrode takes place. However, it is not likely in this case because the reference electrode was outside the flow-through cell and was linked with quite a long Luggin tube which was filled with background electrolyte. If any chloride ions had diffused from the Luggin tube into the sample solution they would have been instantly and dramatically diluted by the electrolyte continuously flowing over the surface.

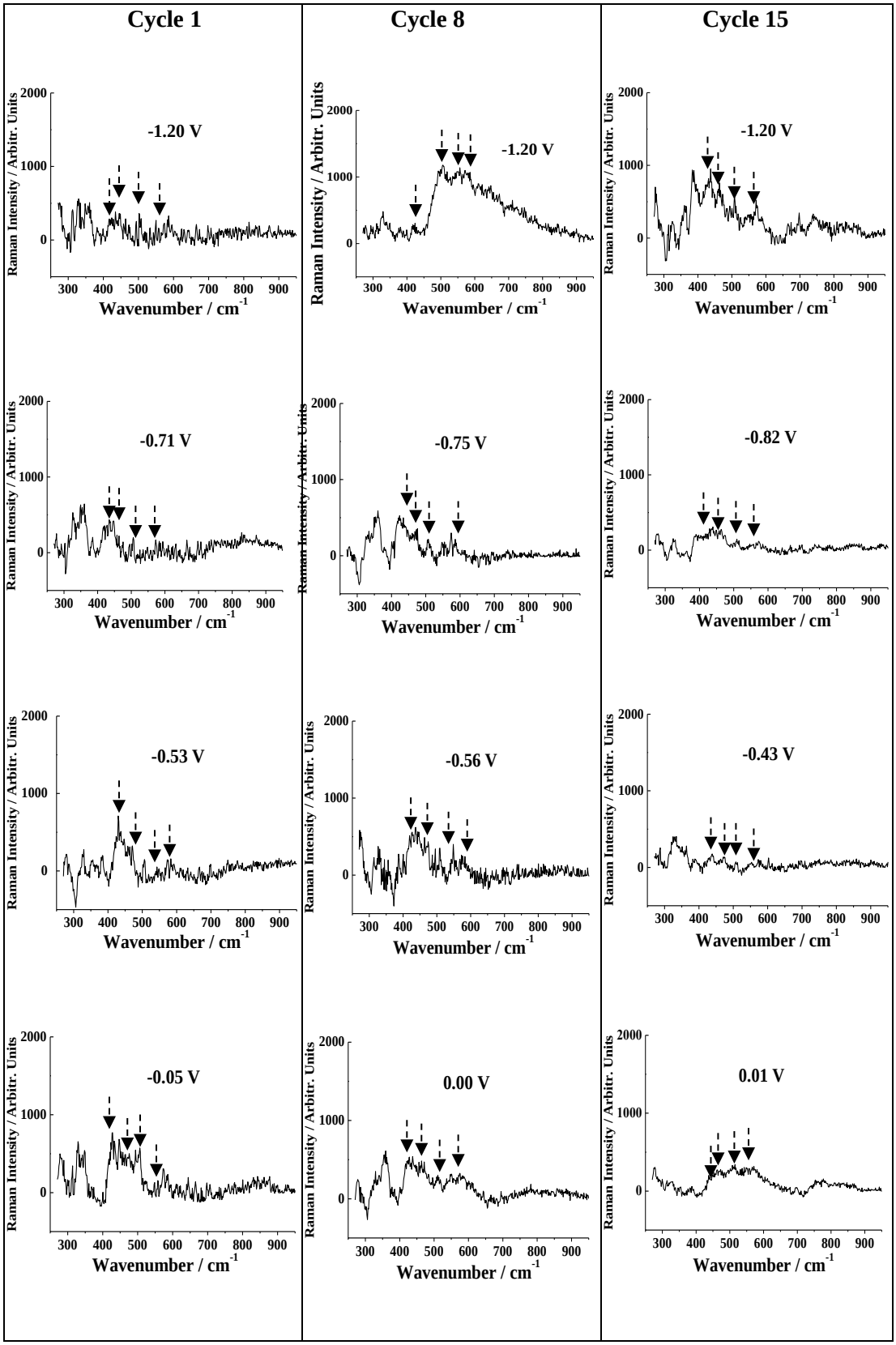


Figure 5.16. Spectra of the residual signals of the in situ spectra in Figures 5.10 - 5.12 after MCR-ALS optimization, with arrows indicating residual bands with components centred around 430, 460, 510 and 560 $cm^{-1}$.

Owing to the substantial difficulties in preparing pure $Fe(OH)_2$, its pyrophoric nature, its decomposition to δ-FeOOH in the presence of water in the course of oxidative processes [140], it was considered impractical and even counter-productive to include a synthesis and an attempted direct measurement of $Fe(OH)_2$ as a standard sample to be included with the other standard components.

### 5.3.3. *In situ* spectra of the O-H stretch region

The spectra recorded *in situ* of the O-H stretch region at various potentials during the active and passive regions of the anodic sweep of the 5$^{th}$ potentiodynamic polarization cycle in 0.05 M NaOH are given in Figure 5.17. The spectra were normalized to the instrument peaks at 2633 $cm^{-1}$ and 2669 $cm^{-1}$. Changes were observed in the intensity of the O-H stretch mode of water as the potential was varied; this behaviour occurred for each cycle. The spectra also contained instrument peaks at 3229 $cm^{-1}$ and 3479 $cm^{-1}$, which were subtracted from the raw spectrum of water in order to obtain the spectrum of pure water only. The spectra of pure water and the instrument peaks at 3229 $cm^{-1}$ and 3479 $cm^{-1}$ were used as pure spectral components for the MCR-ALS optimization of the spectra of the passive film.

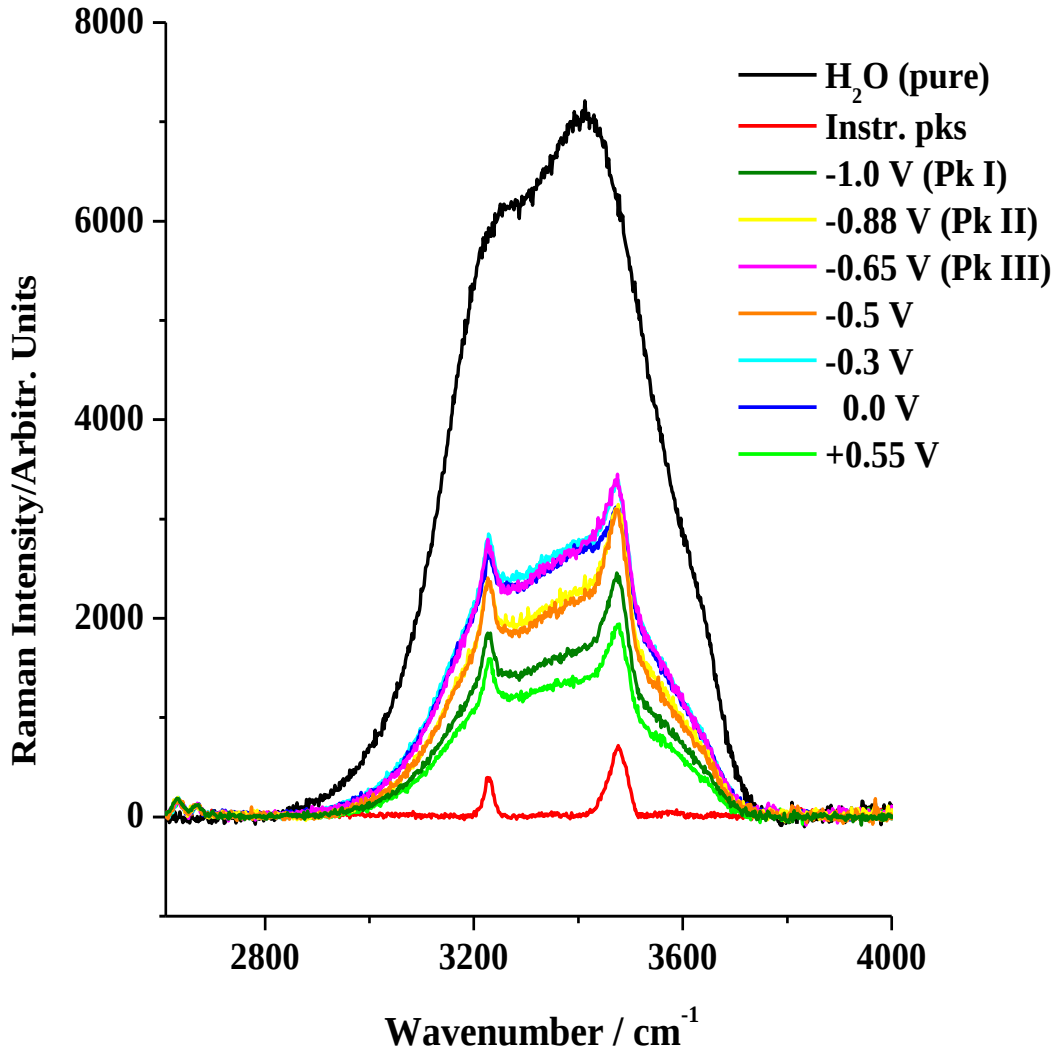


Figure 5.17. Spectra recorded in situ of the OH stretch region during the 5th cycle. Also given are the spectrum of $H_2O$ after subtraction of instrument peaks and the spectrum of the instrument peaks, which were used as pure component spectra for the MCR-ALS optimization.

The amounts of water relative to the instrument peaks determined from the MCR-ALS analysis are plotted in Figure 5.18. The optimal lack of fit was 2.2 %.

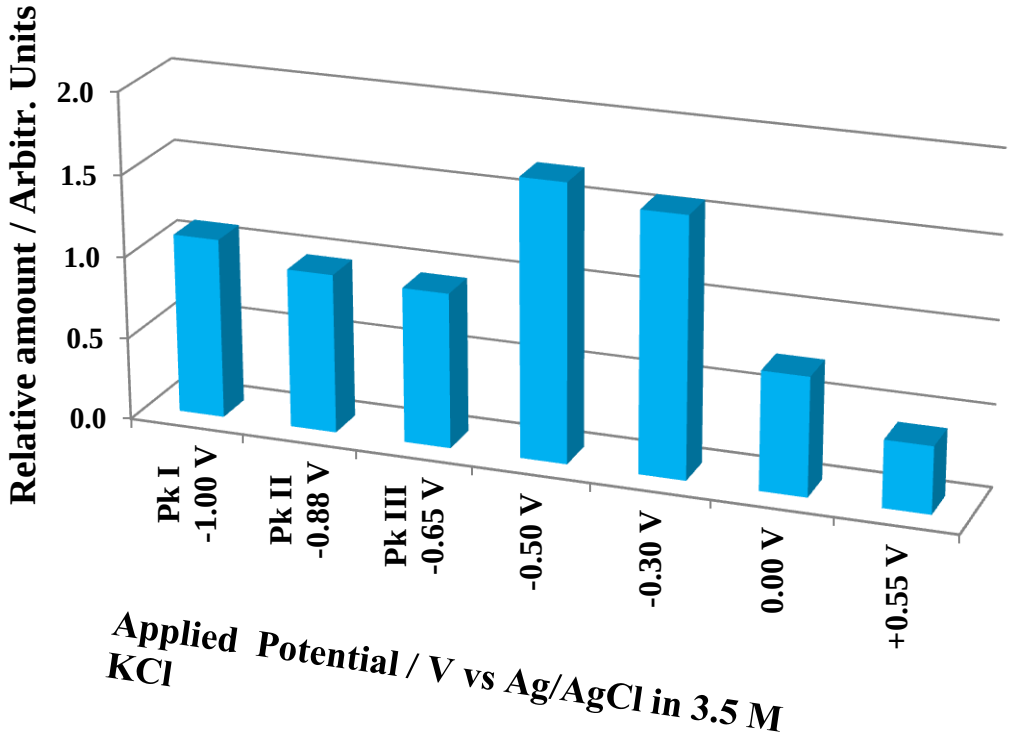


Figure 5.18. Amount of $H_2O$ in the surface film at various potentials in the anodic and cathodic sweep determined using MCR optimization from the spectra recorded *in situ* in the OH stretch region at various potentials in the anodic sweep during the 5$^{th}$ cycle.

## 5.4. DISCUSSION

The enhancement of the Raman spectra afforded by the 636.4 nm excitation as well as the application of Multivariate Curve Resolution provides an opportunity to conduct a more precise investigation of the distribution of the identified iron compounds in the passive film at different stages of growth under the conditions of the present work. Factors that limit the precision of the results yielding in practice a 20 % lack of fit are the use of a limited number of standard reference spectra in the MCR-ALS analysis and the still relatively low signal to noise ratio of the spectra. However, since Figure 5.16 provides the spectral

composition of the residuals of the fitted Raman spectra at similar potentials displayed in Figure 5.14, the disadvantage of other possible compounds in the set of reference spectra is reduced. Indeed the residuals provide evidence of the presence of $Fe(OH)_2$ and associated compounds to be discussed in more detail below.

In Figures 5.11, 5.12 and 5.13 the variation in the composition of the passive film is shown in the initial stage of growth in the 1$^{st}$ cycle, midway in the 8$^{th}$ cycle and at the later stage of growth in the 15$^{th}$ cycle, respectively, of repeated potentiometric polarization in 0.05M NaOH. The respective histograms illustrate the relative amounts of γ-$Fe_2O_3$, α-FeOOH, δ-FeOOH and γ-FeOOH at comparable potentials in the anodic region at different stages of growth. It is apparent that the film formed on the iron surface is a mixture of compounds and that the composition varies with the applied potential and with the number of cycles. This supports previous conclusions regarding the complexity of the film growth namely that a number of different mechanisms may be occurring at different potentials [23,24,142] and that the surface species undergo chemical changes during the potentiodynamic perturbation [14,21,23,24,142].

For the first cycle it is evident that compounds had already formed on the surface at -1.20 V (Figure 5.2), in spite of the prior polarization for 20 minutes at -1.40 V intended to reduce surface oxides which had formed in air and upon immersion in the solution. It was not possible to record spectra at -1.40 V because the surface was obscured with $H_2$ bubbles; for the same reason the potential was not applied below -1.20 V for subsequent cycles. γ-$Fe_2O_3$ and FeOOH compounds are present on the surface at -1.20 V as shown in Figure 5.11 whereas only Fe and /or $Fe(OH)_2$ are expected at this potential [22]. It is possible that the original polarization for 20 minutes at -1.40 V did not completely reduce the surface oxides back to iron, leaving a residual oxide or hydroxide layer. This has been observed and explained similarly in a previous study [16]. For cycles 8 and 15 γ-$Fe_2O_3$ and FeOOH compounds are also observed to be present at -1.20 V as shown in Figures 5.12 and 5.13.

As the applied potential increases through the active region from -1.20 V to Peak III' at around -0.55 V which is the beginning of the passive region, the amounts of α-FeOOH, δ-FeOOH and γ-FeOOH are observed to increase for Cycles 1 and 8, probably due to oxidation of $Fe(OH)_2$. This is expected to occur

over peaks II, III and III' from theoretical calculations at these potentials (Fe $\rightarrow$ FeOOH and $Fe(OH)_2 \rightarrow$ FeOOH [24], $Fe(OH)_2 \rightarrow$ $\alpha$-FeOOH and $\delta$-FeOOH [40], $Fe(OH)_2 \rightarrow$ FeOOH [16,22,24,40,94] via $Fe(OH)_2 + OH^- \rightarrow FeOOH + H_2O + e^-$ and $Fe_3O_4 \rightarrow$FeOOH [94]. As the potential is increased further into the passive region the intensities of the FeOOH compounds begin to decrease overall and at the same time the amount of $\gamma$-$Fe_2O_3$ begins to increase relative to the FeOOH compounds. This may be explained by ageing of the FeOOH to $\gamma$-$Fe_2O_3$, and at the higher anodic potential of +0.64 V the amount of $\gamma$-$Fe_2O_3$ has increased significantly relative to FeOOH indicating yet further ageing. The trends observed in the anodic region for Cycles 1 and 8 are similar, although the relative amounts of the different FeOOH compounds are different and the amount of $\gamma$-$Fe_2O_3$ is greater relative to that in Cycle 1. Similar trends are also observed for the four anodic potentials in Cycle 15 although the overall intensities are weaker, and spectra were not recorded at potentials greater than 0.01 V in the anodic region. The overall amounts of components decreased as the applied potential was increased corresponding to the Raman spectra becoming weaker and broader as the cycle progressed as shown in Figures 5.5-5.9. At all three stages of growth (Figures 5.11-5.13) it is apparent that an increase in the amount of FeOOH compounds occurs in the active region of the anodic sweep and as the potential is increased through the passive region ageing of the FeOOH compounds to $\gamma$-$Fe_2O_3$ occurs with a significant increase in $\gamma$-$Fe_2O_3$ at the highest anodic potential in the passive region.

For the cathodic sweep the results vary for the different stages of film growth represented by Cycles 1, 8 and 15. For Cycle 1 the amounts of FeOOH compounds increase with increasingly negative potentials and the amount of $\gamma$-$Fe_2O_3$ becomes negligible, appearing only in a small amount at -0.95 V. For cycle 8 the FeOOH compounds decrease significantly over the cathodic region but the amounts of $\gamma$-$Fe_2O_3$ increase significantly, while for Cycle 15 there is an overall decrease in both FeOOH and $\gamma$-$Fe_2O_3$. A number of different factors may contribute to the variations observed. The overall intensities of the FeOOH and $\gamma$-$Fe_2O_3$ compounds at each potential determined from the MCR-ALS analysis in these figures depends on both the intensity of the spectra at each potential and the amount of residual spectra due to components not included in the set of pure

component spectra, such as $Fe(OH)_2$ and other intermediates. Another factor is variation in the polarization profile between the first and subsequent cycles, particularly in the cathodic sweep of Cycle 1, where no current peak V was observed in the 1$^{st}$ cycle at potential comparable with the subsequent cycles (Figure 5.1). Another possible variation may be the amount of hydration or amorphous character of the different cycles.

A comparison of the change in the overall amounts of the components at -1.20 V with those for Peaks III and the passive regions in Figure 5.14 shows that with an increased number of cycles the overall amounts of components in the passive region generally decrease towards the later cycles. The reduction in intensities of components and the broadening of the Raman peaks in the 15$^{th}$ and later cycles as the anodic potential is swept to more positive values is considered to result from increased hydration of the surface or formation of an amorphous structure. At -1.20 V on the other hand, the total amounts of components are observed to increase after the first cycle, indicating overall growth of the passive film with increased cycling.

The residual signals which were not fitted by the MCR-ALS optimization are suggested to be due to $Fe(OH)_2$, $Fe(OH)_3$ and intermediate compounds which form in the oxidation of $Fe(OH)_2$ to FeOOH, such as $HFeO_2^-$ (ferrous hydroxo-complex) and $FeO_x(OH)_{3-2x}$ (amorphous ferric oxyhydroxide) [45]. The residual bands vary in intensity with potential and cycling. However it is noted that during the first and eighth cycles the residual spectra at each of the selected potentials are similar and thus are considered to arise from compounds of the same nature. The residual spectra in cycle 15 are substantially weaker and broader, as are the raw spectra, again being consistent with the increasingly amorphous or hydrated nature of the surface with increased cycling in the passive region. Band components appearing at positions around 430, 460, 510 and 560 $cm^{-1}$ have been marked in Figure 5.16 as they are close to bands expected for $Fe(OH)_2$. These bands are present throughout the anodic region from -1.20 V to well into the passive region where they appear to broaden, particularly for the eighth cycle. The relative intensities of the bands vary and it appears that at around 0 V which is well into the passive region, amorphous compounds begin to appear.

The MCR-ALS analysis of the amounts of water in the film from the spectra recorded *in situ* of the O-H stretch region is shown in Figure 5.18. This

demonstrates that more water becomes incorporated into the film as the surface begins to passivate at -0.55 V and supports reports in the literature of increased surface hydration of the passive film in this region [21,27,30]. Since the surface was observed to be visibly darker and less shiny at this potential, the result also confirms that the measurements are determining the increased hydration of the film rather than modulation of the scattered light by the electrolyte. Should the latter be responsible for changes in the water spectrum, the less reflective film surface would have caused in a decrease in the spectral intensity resulting from the presence of water, rather than the observed increase. It is only at anodic potentials well into the passive region, at around 0.0 V, that the measured amount of water begins to decrease. This observation corresponds with those of ellipsometric studies, namely that with further increases of the anodic potential, the passive film begins to progressively dehydrate [26]. It is seen from Figures 5.11 - 13 and 5.14 that near 0.00 V the ratio of $\gamma$-$Fe_2O_3$ to FeOOH compounds has increased which may be explained by ageing of FeOOH to $Fe_2O_3.H_2O$ [22] and with loss of water to $\gamma$-$Fe_2O_3$. Ageing of FeOOH to $Fe_3O_4$ can also occur [22]. Given the expected reactions involving oxidation of $Fe(OH)_2 \rightarrow Fe_3O_4$ and the observation of $Fe_3O_4$ in previous studies of the passive film on iron in neutral borate and 1M alkaline solutions [22,24,40,101,139] it is somewhat surprising that no $Fe_3O_4$ was fitted in the MCR-ALS optimization. The absence of $Fe_3O_4$ bands may be the result of oxidation of the outer part of $Fe_3O_4$ to $\gamma$- $Fe_2O_3$ [26], which would agree with the two layer model [142,144] with an inner layer composed of $Fe_3O_4$ and $\gamma$-$Fe_2O_3$ with the $Fe_3O_4$ adjacent to the metal surface and the $\gamma$-$Fe_2O_3$ adjacent to and underneath a layer of a loosely bound outer layer of FeOOH, so that the $Fe_3O_4$ is not detected even though it may be present.

Alternatively, $Fe_3O_4$ may not have formed under the current experimental conditions, so that the invisible protective film formed on the surface of iron would be $\gamma$-$Fe_2O_3$, which has been described previously as the cubic oxide in crystalline continuity with the metal [46]. The solution was not de-aerated and was continuously flowing over the iron surface, so that oxygen was not in short supply. The cubic oxide $Fe_3O_4$ is formed under conditions of poor oxygen supply by secondary reactions such as interaction between ferrous and ferric hydroxides [46]. This would also explain the observation in a SERS study of rotating

vs. stationary iron electrodes in which $Fe(OH)_2$ was predominantly found on the surface of a rotating disk electrode while $Fe_3O_4$ formed predominantly on a stationary electrode [145]. The finding of only $\gamma$-$Fe_2O_3$ on the surface is also supported by a SERS study on low carbon steel [102], and which forms as a result of conversion of the iron from $Fe_3O_4$ to $\gamma$-$Fe_2O_3$ by dissolved oxygen in the solution. It has been concluded that the longstanding controversy regarding the composition of the passive film is partly the result of the surface potential employed, the history of the iron surface and the chemistry of the solution [142]. The present results support this conclusion.

From Figure 5.14 it follows that $\gamma$-$Fe_2O_3$, $\alpha$-FeOOH and $\gamma$-FeOOH are major components of the surface film at the beginning of the anodic sweep at a potential of -1.20 V. Further oxidation at Peak III results in increased formation of $\delta$-FeOOH and decreased amounts of $\gamma$- $Fe_2O_3$. Further anodic polarization to the passive region results in a general increase in the amounts of $\gamma$-$Fe_2O_3$, and well into the passive region the amounts of $\alpha$-FeOOH and $\gamma$-FeOOH have decreased while $\gamma$- $Fe_2O_3$ and $\delta$-FeOOH have increased. In the ellipsometric study of iron in 0.05M NaOH [21] an oxidation process at a potential equivalent to -0.62V (vs Ag/AgCl in 3.5 M KCl) was attributed to a progressively growing outer layer of FeOOH, while oxidation of the outer part of the inner layer of $Fe_3O_4$ to $Fe_2O_3$ was suggested to occur in the passive region at a potential equivalent to -0.42V (vs Ag/AgCl in 3.5 M KCl).

The observations of the composition of the passive film at the four different regions of the anodic sweep complement the two-layer model described in a previous ellipsometry and electrochemical study [21]. The brown colour reported by them to appear at peak III which was attributed to $\delta$-FeOOH [21] also appeared in the present study at peak III. This is consistent with the MCR-ALS results for this potential in which $\delta$-FeOOH was determined as the major iron oxy-hydroxide formed well into the passive region, but during formation over the anodic sweep $\gamma$-FeOOH and $\alpha$-FeOOH were also present in significant amounts (Figures 5.11 – 5.13 and 5.14).

The observation in the present study of greater amounts of water in the surface film at the onset of passivation corresponds to the lower refractive index (and lower density), due to a porous film of FeOOH containing considerable

electrolyte [21]. In addition the observation in the present study that $\gamma$-$Fe_2O_3$ was present predominantly at -1.20 V and well into the passive region supports the findings from refractive index and density measurements [21] of an inner adherent layer formed by reduction of FeOOH in the cathodic sweeps. However, the inner layer in this study would be $\gamma$-$Fe_2O_3$ and not $Fe_3O_4$ as proposed in the ellipsometric study. From index of refraction and film density measurements in ellipsometric studies [21,26] it was concluded that the passive film on iron formed in 0.05M NaOH was composed of an inner, compact layer of high density and an outer porous layer containing electrolyte of $Fe(OH)_2$ which is oxidized to FeOOH with anodic polarization. Although the composition cannot be determined from the above optical measurements, the inner layer was suggested to be $Fe_3O_4$ [21] in view of certain Raman studies of iron in alkaline solution [10]. The densities of $Fe(OH)_2$ (3.40 g/cm$^3$) and FeOOH (4.28 g/cm$^3$) are easily distinguished from that of $Fe_3O_4$ (5.18 g/cm$^3$); however, the density of $\gamma$-$Fe_2O_3$ (5.24 g/cm$^3$) is very similar to that of $Fe_3O_4$ and so the presence of $\gamma$-$Fe_2O_3$ is not unexpected. Indeed $\gamma$-$Fe_2O_3$ is thermodynamically favoured at potentials in the passive region [115] and from XRD studies of the passive film formed on iron in alkaline solution at different potentials in the passive region $\gamma$-$Fe_2O_3$ was found at all potentials except in the transpassive region where $Fe_3O_4$ was found instead [146].

The presence of $\gamma$-$Fe_2O_3$ in the passive film would be favourable for passivation of iron. The protective qualities of the cubic oxide on the iron surface can be related to the conductivity of the oxide [146]: $\gamma$-$Fe_2O_3$ is a poor conductor and would protective and render the film passive, whereas $Fe_3O_4$ is $10^6$ times more conductive, probably due to rapid oscillation between the $Fe^{2+}$ and $Fe^{3+}$ sites [147], and would therefore be considerably less-protective.

As the number of potentiodynamic cycles was increased from Cycle 1 to 18 the spectra of the passive film changed: they evolved from showing distinct bands for the first few cycles to weaker, very broad bands for Cycle 18 (Figures 5.5 to 5.9). This indicates that the passive film evolves from a more crystalline nature during its initial stages of growth during cycles 1 to 15 to a more amorphous one from cycles 15 to 18. This observation may explain the different reports of the crystalline/amorphous nature of the passive film given in the literature. It also highlights the importance of detailed monitoring of the film growth during

potentiodynamic polarization, not only over different potentials but also over different cycles.

## 5.5. CONCLUSIONS

The unique combination of Raman microscopy *in situ* with pre-resonance enhancement, slow potentiodynamic polarization and Multivariate Curve Resolution with Alternating Least Squares (MCR-ALS) analysis of the spectra has provided further insights into the composition of the passive film on iron at various stages during its growth by repeated cycling in 0.05 M NaOH. The enhanced intensity afforded by the 636.4 nm excitation line for Raman bands of the iron oxide compounds has enabled detection and differentiation of the different iron oxides and oxy-hydroxides on the surface even during the initial stages of growth. Owing to the extent of overlap of the Raman bands of the different iron oxide compounds, MCR-ALS analysis was used to determine the relative amounts of six different iron oxide compounds expected to form on iron surfaces in 0.05 M NaOH: $Fe_3O_4$ (magnetite), $\gamma$-$Fe_2O_3$ (maghemite), $\alpha$-$Fe_2O_3$ (hematite), $\alpha$-FeOOH (goethite), $\delta$-FeOOH (feroxyhyte) and $\gamma$-FeOOH (lepidocrocite), using standard Raman spectra of these compounds as initial input data. The residual error established by the analysis was attributed to other components which were not included as initial data and to the relatively low signal to noise ratio of the spectra. Examination of the residual component spectra showed that approximately half of the residual Raman bands present could be attributed to $Fe(OH)_2$. The other bands remain unassigned, but may include intermediate compounds in the oxidation of $Fe(OH)_2$ to FeOOH such as ferric hydroxide, ferrous hydroxo-complexes and amorphous ferric oxyhydroxide.

Using pre-resonance enhancement and MCR-ALS it was possible to identify the different FeOOH compounds on the surface and to distinguish more clearly between $Fe_3O_4$ and $\gamma$-$Fe_2O_3$ during the initial stages of growth of the passive film on iron by cyclic polarization. The observations agree with a two layer model for the passive film of an inner, high density compound with an outer layer of lower density determined from an ellipsometric study in 0.05M NaOH [21,26]. The present work is consistent with the concepts of this model in which the inner layer is $\gamma$-$Fe_2O_3$, while the outer layer contains a mixture of $\delta$-FeOOH, $\alpha$-FeOOH and

γ-FeOOH in amounts which along with other components such as $Fe(OH)_2$ and intermediates formed in the oxidation of $Fe(OH)_2$ vary with potential and with cycling. The passive film becomes more hydrated at the beginning of the passive region and dehydrated at more anodic potentials well into the passive region, corresponding with an increase in γ-$Fe_2O_3$. $Fe_3O_4$ was not detected in the spectra and this may be either because it is adjacent to the metal surface, forming the innermost part of the inner layer with γ-$Fe_2O_3$ forming the outermost part. Alternatively, $Fe_3O_4$ may not be present so that γ-$Fe_2O_3$ is the only component of the inner layer formed on the surface of iron and in crystalline continuity with the metal, protecting the metal from further oxidation, and covered with an outer, more loosely bound layer of varying amounts of δ-FeOOH, α-FeOOH and γ-FeOOH. Being a poor conductor γ-$Fe_2O_3$ would render the film passive, whereas $Fe_3O_4$ is much more conductive and is thus less likely to form a protective, passive film.

The evolution of the passive film from a more crystalline nature to a more amorphous one during growth with increased cycling highlights the importance of detailed monitoring of the film growth during potentiodynamic polarization, not only over different potentials but also over different cycles, and also may explain the different reports of the crystalline/amorphous nature of the passive film given in the literature.

# CHAPTER 6

# ANALYSIS OF THE COMPOSITION OF THE PASSIVE FILM ON IRON UNDER PITTING CONDITIONS IN 0.05 M NaOH/NaCl USING RAMAN MICROSCOPY *IN SITU* WITH ANODIC POLARIZATION AND MCR-ALS

*(Content published online in Journal of Raman Spectroscopy [148])*

## 6.1. INTRODUCTION

Extensive studies of the localized breakdown of the passive film formed specifically on iron under the influence of aggressive anions, reviewed by a number of authors [6,48,64,76-78], have shown that the initiation and stability of localized breakdown of the passive film is affected by numerous factors. The complexity in experimental conditions is the probable source of the different and sometimes conflicting mechanisms proposed for the initiation and growth of pits. However, there is general agreement on the pitting process in several respects, namely that: (a) localized adsorption of aggressive anions on the surface is the first step in pitting; (b) adsorption of anions always occurs at defect sites on the surface; (c) a dynamic equilibrium exists between localized breakdown and re-passivation of the passive film; and (d) when a critical level of aggressive anion concentration is reached at which re-passivation is hindered, the equilibrium is shifted in favour of the localized breakdown and stable pitting occurs. A major difference in the mechanisms of the stable pitting proposed by the various pitting theories (see Chapter 1, Section 1.3.2 and in more detail Appendix 1) concerns whether the aggressive anion is incorporated into the passive film or not [6].

The presence of chloride ions near the surface of iron in a solution of NaOH results in the formation of a dark green gelatinous precipitate [44,52,80-93], and different ferrous hydroxide compounds are involved in the formation of this compound depending on the ratio of $[Cl^-]/[OH^-]$ [84,89] as discussed in detail in Chapter 1, Section 1.3.4. As the $[Cl^-]/[OH^-]$ ratio in the electrolyte in the present study is unity, the compound formed after addition of chloride could be either

Green Rust I or a hydrated magnetite and thus the nomenclature Green Complex will be used for its description.

In Chapter 5 it was shown that the iron oxides and oxy-hydroxides present on the surface of iron in 0.05 M NaOH in the passive region during cyclic potentiodynamic polarization were largely $\gamma$-$Fe_2O_3$, $\alpha$-FeOOH, $\delta$-FeOOH, $\gamma$-FeOOH as well as $Fe(OH)_2$. The relative amounts of these compounds were found to vary with potential and also with different cycles. In addition, the amount of water was found to increase as the potential was increased into the passive region, but at higher anodic potentials the water content was found to decrease.

It was the purpose of the present work to further examine the state of the passive film in the presence of chloride ions by first investigating the relative amounts of the Green Complex as well as the seven iron oxide and oxyhydroxide compounds investigated in Chapter 5 and second by determining the relative amount of water incorporated in the film before and during the onset of stable pitting. It was considered that this information would provide new insights into the pitting process.

## 6.2. EXPERIMENTAL PROCEDURE

### 6.2.1. Potentiodynamic Polarization

The experimental conditions for the three-electrode cell were the same as those already described in Chapter 3, except that a Schlumberger SI1286 potentiostat was used. The iron surface was initially subjected to cathodic polarisation for 20 minutes at –1.40 V to remove oxide compounds formed in air and upon immersion in the 0.05 M NaOH solution. A passive film was grown on the surface by subjecting the iron to two cycles of potentiodynamic polarization; for each cycle the potential was swept first anodically and then cathodically between -1.20 V and +0.60 V at a sweep rate of 10 mV/s, these procedures being similar to those of Chapter 5. During the anodic polarization oxidation reactions occurred, leading to a series of current peaks. These processes are illustrated in Figure 6.1. During the third anodic sweep the potential was held at –0.55 V, being the beginning of the passive region. At this point a solution of NaCl was added to the electrolyte such that its concentration in the electrolyte was 0.05 M,

so that the resulting electrolyte solution was 0.05 M NaOH + 0.05 M NaCl with pH 12.7.

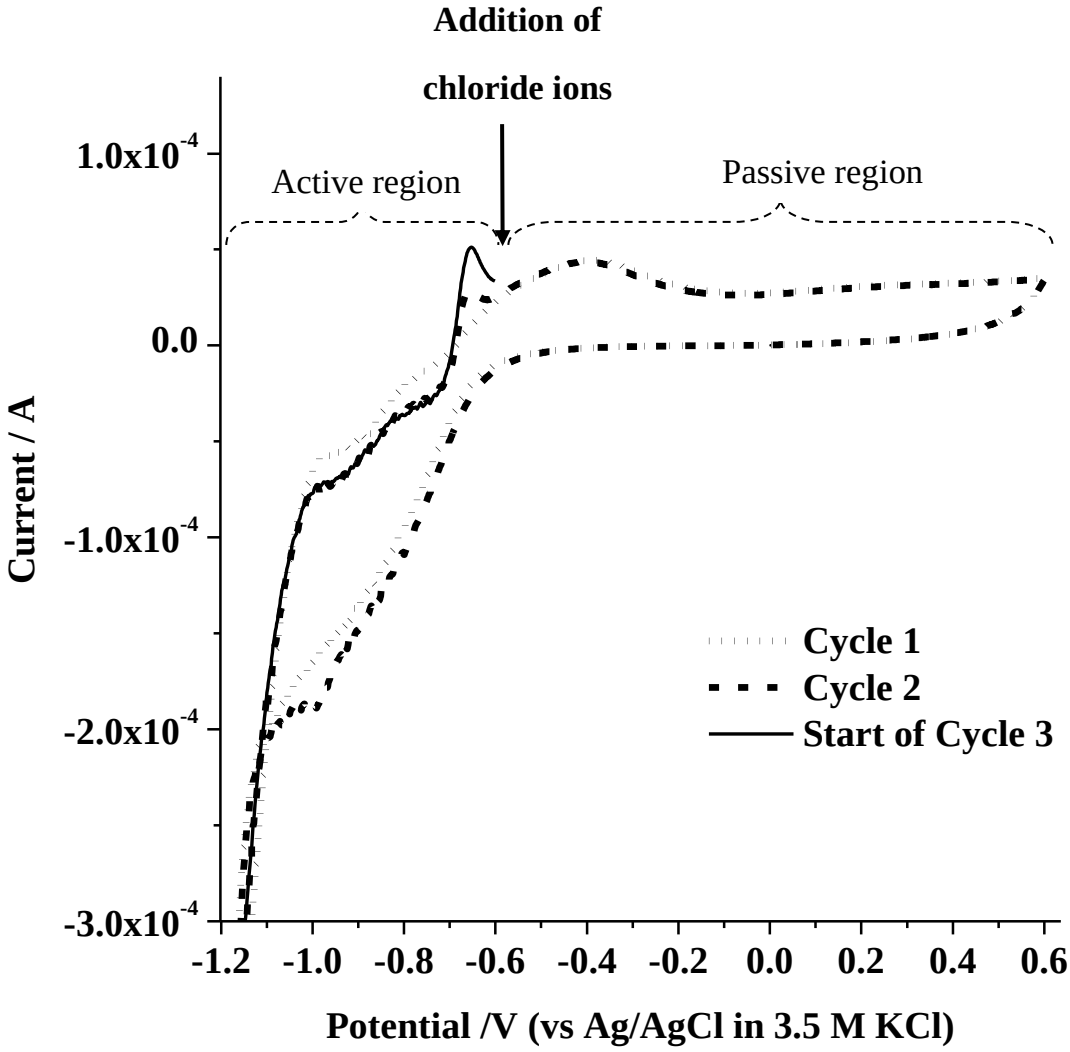


Figure 6.1. Initial polarisation cycles in 0.05 M NaOH at 10mV/s between –1.2 V and +0.6 V, after cathodic reduction at –1.4 V and before addition of NaCl at –0.55 V in the anodic sweep of the 3rd cycle. The active and passive regions are indicated by brackets. The arrow indicates point on the 3rd anodic cycle at which chloride ions were added.

The potential was kept at –0.55 V and the current was then monitored as a function of time for 1200 s. During this period, Raman spectra were recorded of the iron surface as discussed below. The potential was then increased by +0.10 V

and held there for another 1200 s while corresponding current and Raman measurements were carried out. This procedure was repeated until the pitting potential was reached, being that at which stable pitting occurred as indicated by a steady sharp increase in current. At this point the potential was held constant while spectra were recorded of various pits that were visible and the surface regions adjacent to the respective pits. The potential was then increased above the pitting potential and spectra were again recorded of various pits and their adjacent surfaces.

The above experiment was repeated under identical conditions but using argon ion laser excitation of wavelength 514.5 nm after cleaning and polishing the iron sample to the same surface roughness. Thus *in situ* Raman spectra could be recorded of the O-H stretch region at the same potentials as used previously.

### 6.2.2. Raman Microscopy

The experimental conditions used for recording the Raman spectra *in situ* of the iron oxide and oxyhydroxide compounds have been described in Chapters 4 and 5. For the Raman spectra obtained *in situ* of the O–H stretch vibration between 4300 and 2300 $cm^{-1}$, the 514.5 nm excitation line of a Coherent Innova 308 argon-ion laser was used at an output power of 500 mW with 120 s integration time. The other experimental conditions are identical to those described in the previous Chapters.

### 6.2.3. Preparation of Green Complex for the MCR-ALS optimization

The structure of synthetically prepared Green Rusts has often been found to differ from that of the Green Rusts in the corrosion products [82,93]. For this study a Green Complex was prepared using reagents of the same chloride ion concentrations as those used in the electrolyte under pitting conditions. 10 ml of a 0.05 M $FeCl_2$ solution were added to 20 ml of a 0.05 M NaOH solution. A green gelatinous precipitate formed which was quickly filtered, placed on a glass slide and covered with a cover slip to prevent rapid aerial oxidation. A Raman spectrum was immediately recorded of the prepared compound using the 636.4 nm excitation line at a laser power of 19 mW (0.3 mW at the sample) and integration time of 130 s using the 20× long working distance objective. Weak and broad

bands were observed in the Raman spectrum at 555 $cm^{-1}$ and 1097 $cm^{-1}$; with time the compound eventually converted to $Fe_3O_4$ (Fig 6.2).

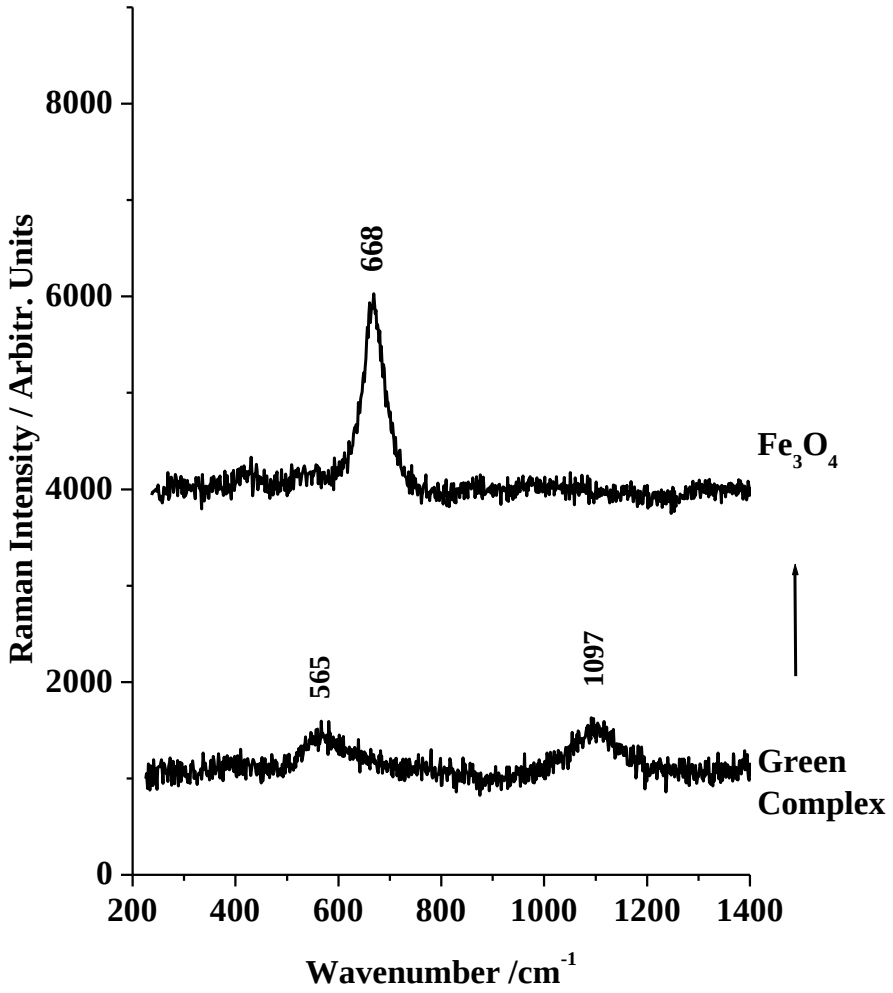


Figure 6.2. Raman spectra of freshly prepared Green Complex (lower spectrum) which converted with time to $Fe_3O_4$ (upper spectrum). The spectrum of Green Complex was truncated from 270 $cm^{-1}$ to 950 $cm^{-1}$ for the MCR-ALS analysis. Recorded using 636.4 nm excitation at 19 mW (0.3 mW at the sample) and 130 s integration time.

The bands at 550 and 1097 $cm^{-1}$ have been attributed to $Fe(OH)_2$ [18,92]. Green Rust I has been reported to have bands at 430, 503 $cm^{-1}$ [41] or 505 $cm^{-1}$ [86] and 560 or 544 $cm^{-1}$ due to the $Fe(OH)_2$ component, and at 303, 387 and 698 $cm^{-1}$ from the $Fe(OH)_3$ component [45]. The compound formed therefore appears to be more a hydrated, amorphous magnetite compound than a Green Rust, and hence

the nomenclature Green Complex will be used as discussed previously. This complex is considered to be more likely to form than Green Rust I in a solution of 0.05 M NaCl + 0.05 M NaOH.

### 6.2.4. MCR-ALS

This technique is a least squares optimization method which enables a determination of the relative amounts of components present in a mixture by performing iterative optimization of the resolved concentration and spectral profiles of the individual components subject to selected constraints. The method has been described in detail in Chapter 3, Section 3.4 and is based on the MCR-ALS toolbox of MATLAB [118]. The spectra of the seven individual pure iron oxide and oxy-hydroxide compounds recorded previously as described in Chapter 4, namely $Fe_3O_4$ (magnetite), $\alpha$-$Fe_2O_3$ (hematite), $\gamma$-$Fe_2O_3$ (maghemite), $\alpha$-FeOOH (goethite), $\beta$-FeOOH (akaganeite), $\delta$-FeOOH (feroxyhyte) and $\gamma$-FeOOH (lepidocrocite) together with the spectrum of the prepared Green Complex were used as pure component spectra for the optimization. All spectra were adjusted to the same height for the instrumental peak at 1562 $cm^{-1}$ for the optimization. This was essential to ensure that the relative intensities in the matrix of pure component spectra were accurate; in particular the spectrum of the Green complex which was recorded using a different objective (20×) from that for the other iron oxide and iron oxy-hydroxide powder samples (100×).

As discussed in Chapter 4, Section 4.1, the selection of the seven iron oxide and oxyhydroxide compounds was directly guided by earlier investigations of the passive film on the surface of iron in alkaline solutions using Raman, XPS, Mössbauer, ellipsometry and SIMS studies and their respective conclusions identifying these compounds as constituents. The MCR-ALS analysis has the advantage that a significant percentage lack of fit indicates the presence of additional compounds besides those chosen as the pure components. These residual components can be determined and identified as shown in Chapter 5.

MCR-ALS optimization was also used to determine the relative amounts of water in the film over the passive region from the Raman spectra recorded *in situ* of the O–H stretch region, after adjusting the spectra to the same height for the instrumental peaks at present in each spectrum at 2633 and 2669 $cm^{-1}$.

## 6.3. RESULTS

### 6.3.1. Raman spectra of the passive film at different potentials

After the addition of the 0.05 M sodium chloride at the beginning of the passive region, Raman spectra were recorded of the surface at various constant values of the applied potential between –0.55 V and +0.30 V for 1200 s using an excitation wavelength of 636.4 nm and a laser beam spot size of 5 μm diameter. The chronoamperometric data are shown in Fig 6.3. At +0.10 V a sharp increase in current is observed after 1000 s which signals the onset of stable pitting.

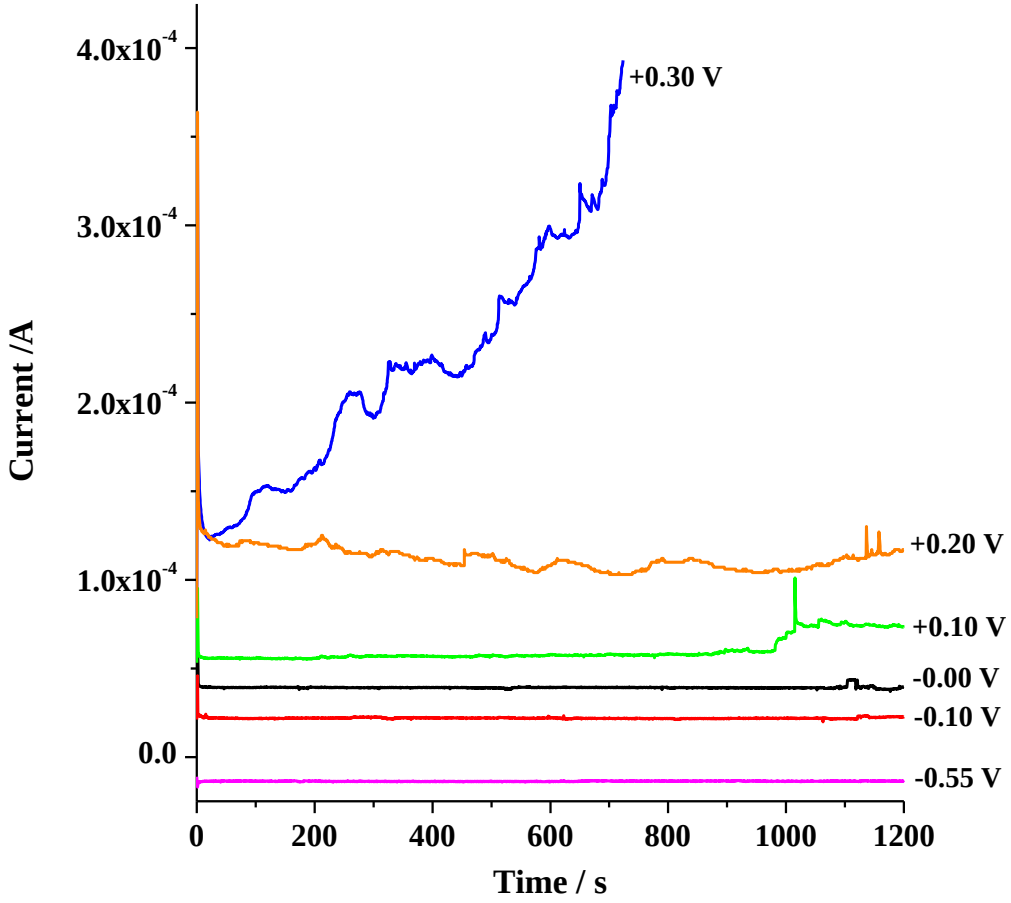


Figure 6.3. Chronoamperometric traces recorded at –0.55 V at 10 mV/s between -1.20V and +0.60 V during the third potentiodynamic polarization cycle after addition of 0.05 M NaCl to the 0.05 M NaOH solution.

The Raman spectra recorded at each applied potential are given in Figure 6.4. The spectra have been corrected by the subtraction of a curved baseline which increased continuously, particularly toward low wave-number shifts arising from reflection by the metal surface and from the holographic notch filter used. A polynomial fitting function was used in this procedure.

When stable pitting was observed at +0.10 V, Raman spectra were recorded of various pits that were visible on the surface and of surfaces adjacent to the pits, these being shown in Figure 6.5. Similar spectra were also recorded at +0.30 V which was 0.20 V more positive than the pitting potential. These spectra are also shown in Figure 6.5.

MCR-ALS optimization was used to determine the relative amounts of Green Complex, $Fe_3O_4$, $\gamma$-$Fe_2O_3$, $\beta$-FeOOH, $\delta$-FeOOH and $\gamma$-FeOOH from the Raman spectra of Figures 6.4(a) and (b) and 6.5(a) and (b). In all cases the compounds $\alpha$-$Fe_2O_3$ and $\alpha$-FeOOH were not present in significant amounts.

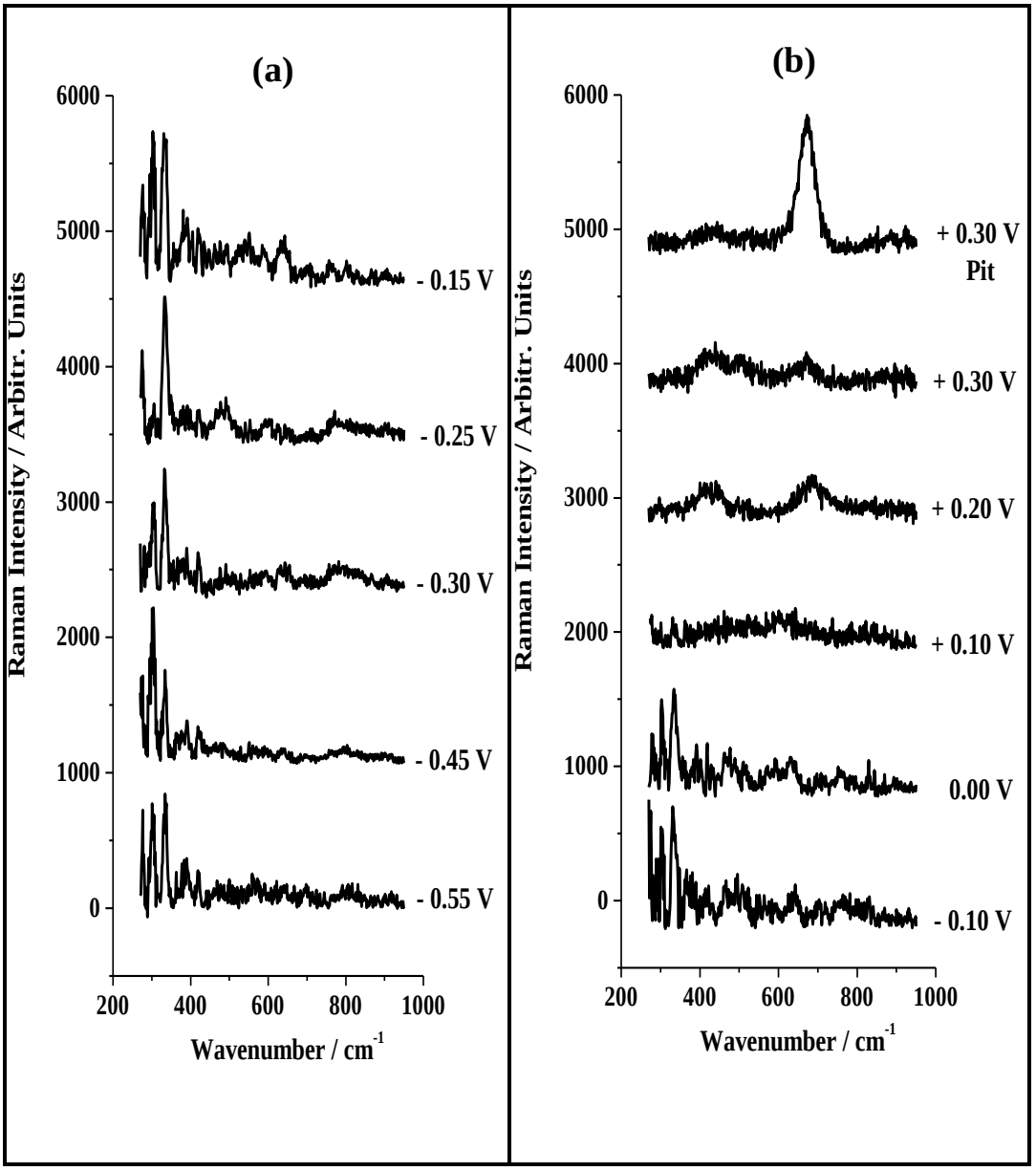


Figure 6.4. Raman spectra of surface recorded *in situ* with pre-resonance enhancement while the applied potential was held for 1200 s at potentials between (a) –0.55 V and –0.15 V and (b) –0.10 V and +0.30 V, after the addition of 0.05 M NaCl to the 0.05 M NaOH solution at –0.55 V. Recorded using 636.4 nm excitation at 105 mW (2 mW at the sample) and 130 s integration time.

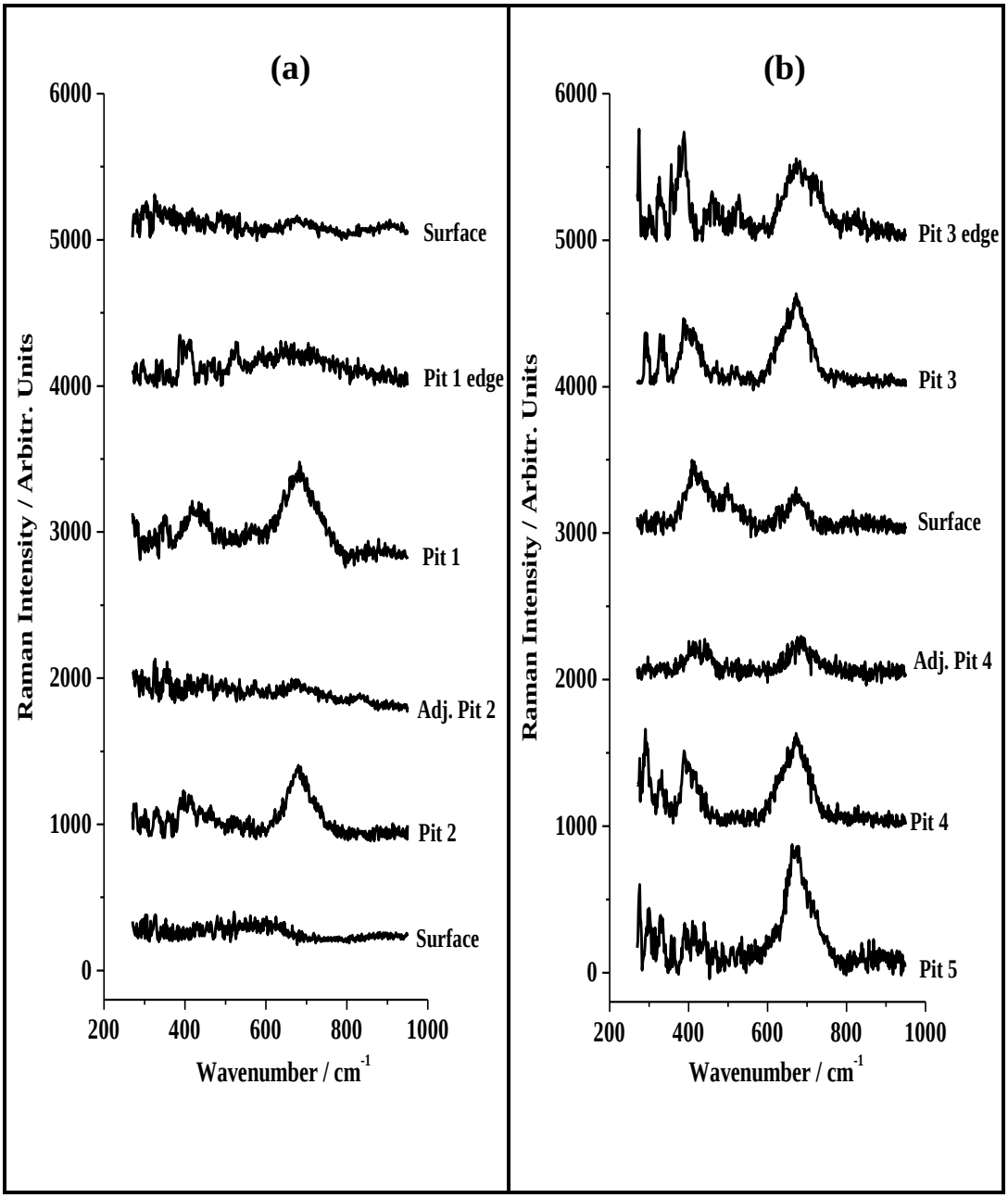


Figure 6.5. Raman spectra recorded *in situ* of pits and adjacent surfaces while the applied potential was held at (a) +0.10 V and (b) +0.30 V after addition of chloride ions to the 0.05 M NaOH electrolyte. The locations of the pits and their adjacent surfaces are respectively displayed in Figures 6.6 (Pits 1 and 2) and 6.7 (Pits 3, 4 and 5). Recorded using 636.4 nm excitation at 105 mW (2 mW at the sample) and 130 s integration time.

The compositional analyses shown in Figure 6.6 are derived from the spectra of Figure 6.4 recorded *in situ* at different potentials during anodic polarisation in the passive region. The average optimal lack of fit was 8.5%. An

analysis of the composition of a pit is included in Figure 6.6 for comparison purposes.

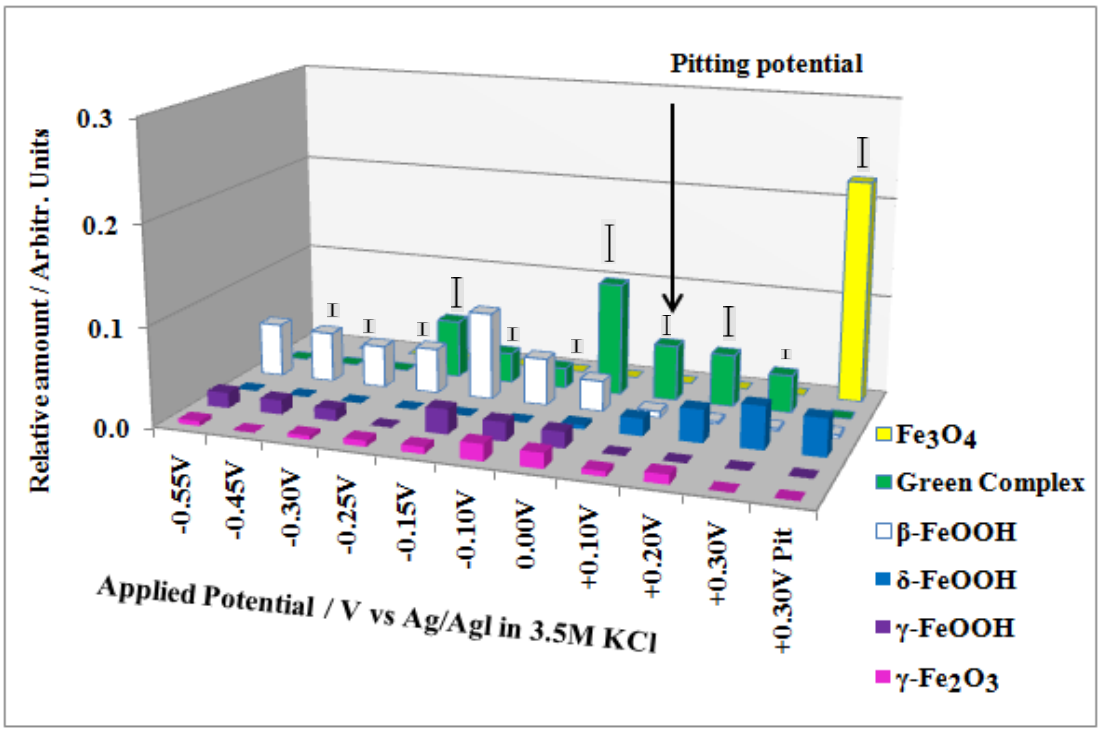


Figure 6.6. Relative amounts of five iron oxide components and Green Complex determined using MCR-ALS optimization from spectra recorded *in situ* of a 5µm diameter area on the iron surface at different potentials in the passive region after addition of $Cl^-$ to the 0.05 M NaOH solution. The average optimal lack of fit was 8.5%.

The composition of the pit components and their adjacent surfaces corresponding to the potentials of +0.10 V and +0.30 V are shown in Figures 6.7 and 6.8, respectively, each with average optimal lack of fit values of 6.1 %.

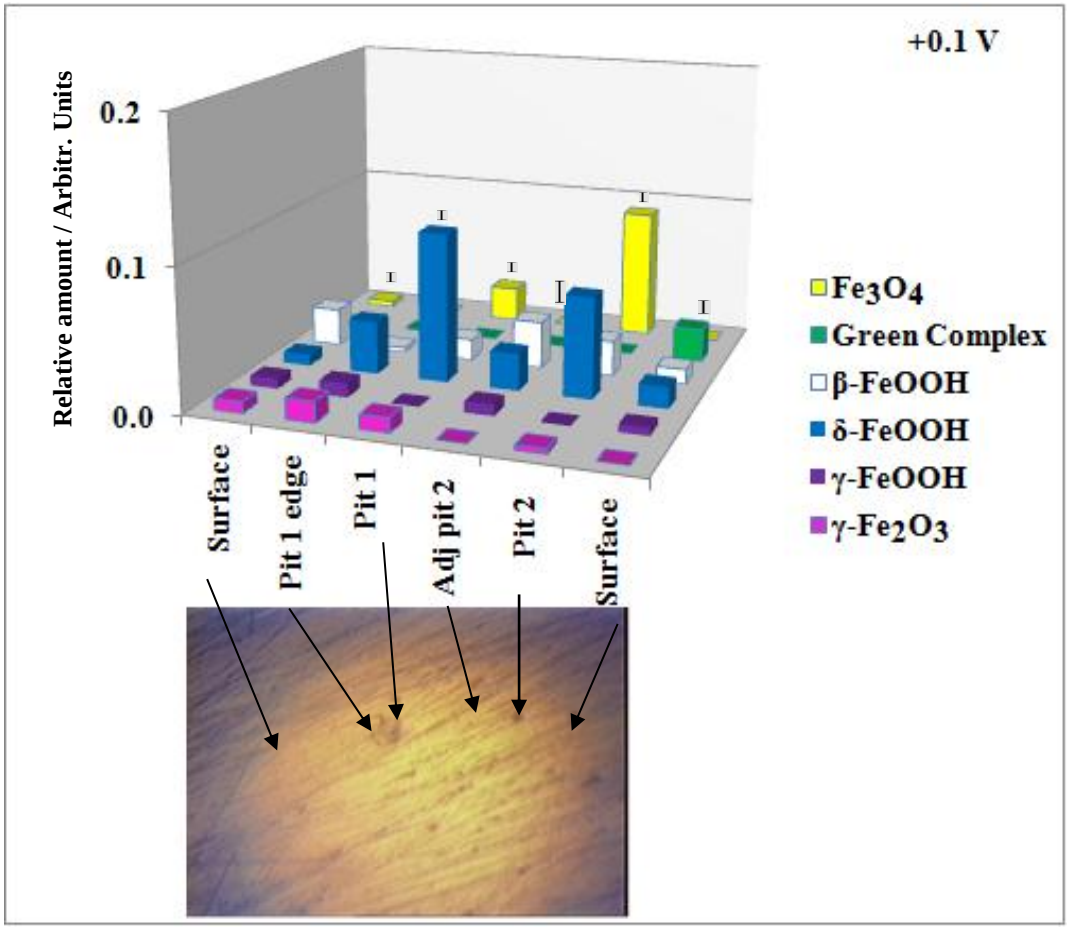


Figure 6.7. Relative amounts of five iron oxide components and Green Complex determined using MCR-ALS optimization from spectra recorded *in situ* from pits and the surrounding areas on the iron surface during stable pitting at +0.10 V. (Photo 500 µm × 375 µm). The average optimal lack of fit was 6.1 %.

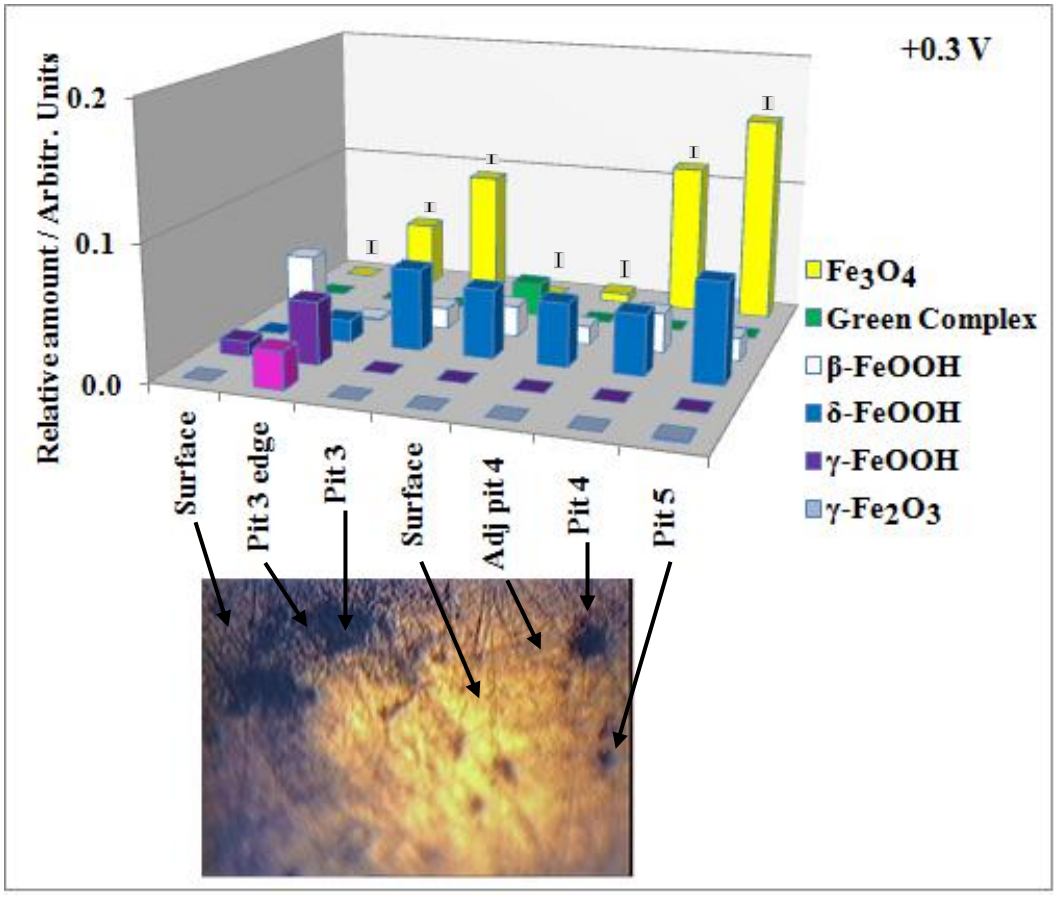


Figure 6.8. Relative amounts of five iron oxide components and Green Complex determined using MCR-ALS optimization from spectra recorded *in situ* from pits and the surrounding areas on the iron surface during stable pitting at +0.3 V. (Photo 500 μm × 375 μm). The average optimal lack of fit was 6.1 %.

These lack of fit values for the results of Figures 6.6, 6.7 and 6.8 are small, considering (i) the relatively low signal-to-noise ratio of the Raman spectra of the surface areas, in spite of the pre-resonance enhancement as well as (ii) possible contributions coming from other components that were not included with the eight pure component spectra, such as $Fe(OH)_2$ and intermediate complexes which may form during oxidation of $Fe(OH)_2$ [45].

Figure 6.9 shows the component spectra fitted by the MCR-ALS optimization, along with the residual spectra, for some of the key spectra recorded at the pitting potential: the surface at +0.10 V (from Figure 6.6), the surface and edge of Pit 1 and the surface of Pit 2 (from Figure 6.7).

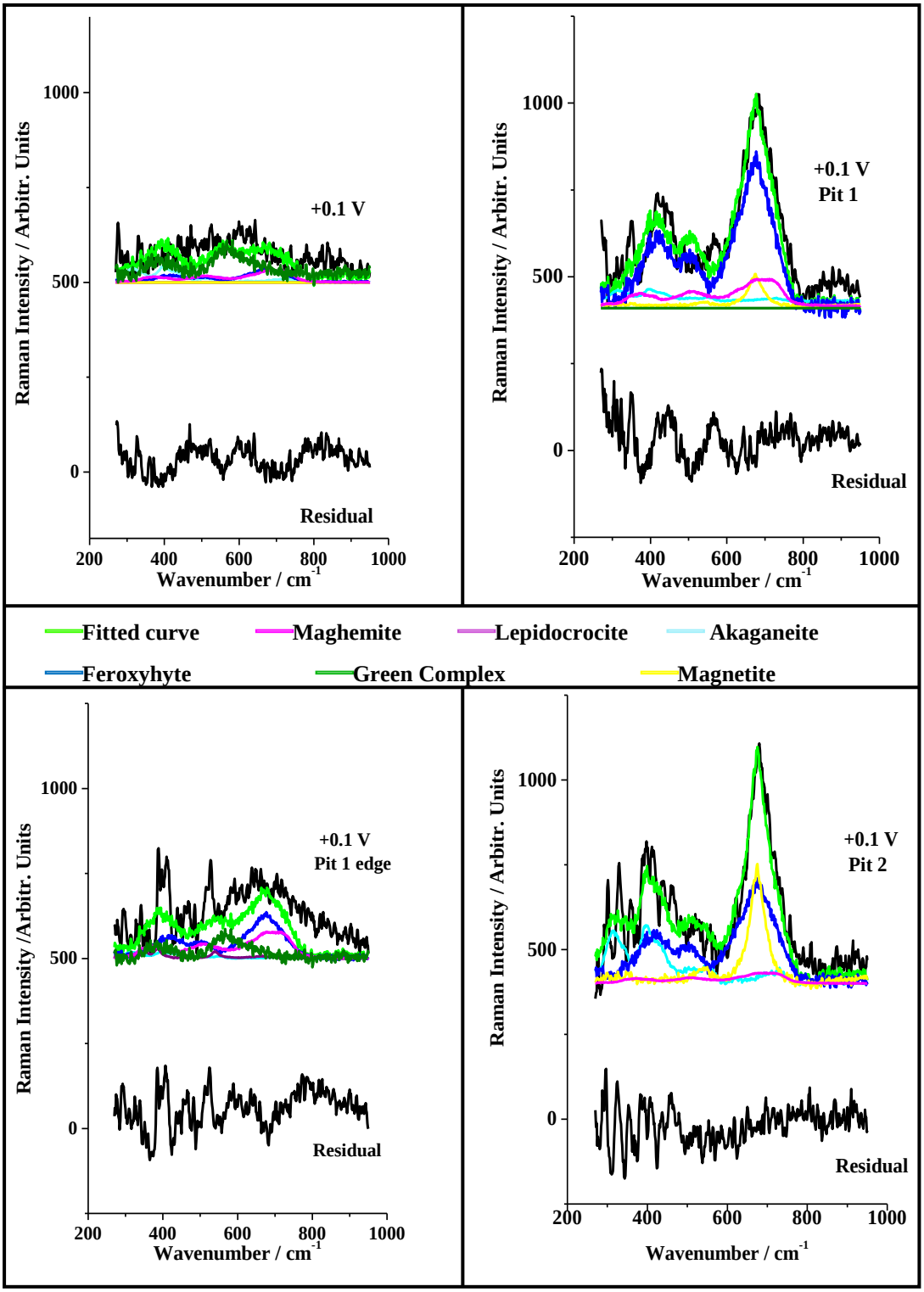


Figure 6.9. MCR-ALS optimized fits for *in situ* spectra recorded at the pitting potential (+0.1 V) of the surface (top left), Pit 1 (top right) the edge of Pit 1 (bottom left) and Pit 2 (bottom right), showing the fitted curve (green spectrum), component spectra and the residual spectra for each.

The residual spectra show weak, broad bands between 450 and 600 $cm^{-1}$ which were also observed in the spectra recorded *in situ* of the surfaces during the growth of the passive film, and which suggest the presence of intermediate iron oxide species other those included in the MCR-ALS optimization, such as $Fe(OH)_2$, $Fe(OH)_3$ and intermediate complexes already described in Chapter 5. The additional bands are present in the spectrum of the surface at +0.1 V at around 630, 780, 827 and 900 $cm^{-1}$ are unassigned.

After removing the iron sample from the cell and allowing the surface to dry in air, Raman spectra shown in Figure 6.10 were recorded of a pit that had formed and its adjacent surface.

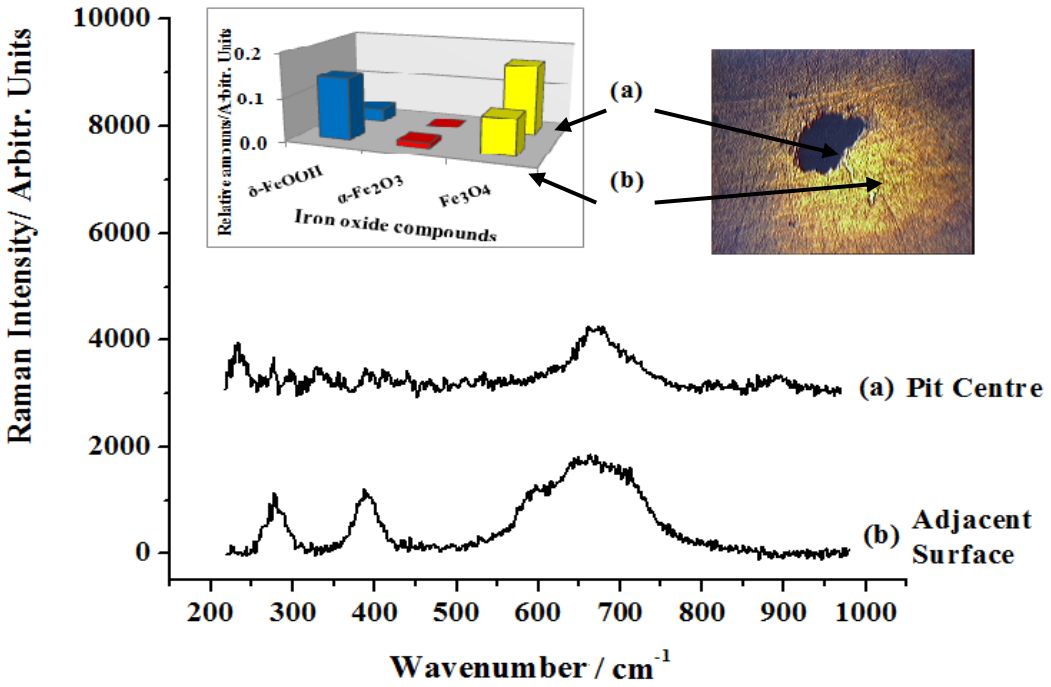


Figure 6.10. Raman spectra measured *ex situ*: (a) At the centre of a large pit (top right inset with a picture area of 500 μm × 375 μm) formed after being held for 1200 s at an anodic potential of +0.30 V in 0.05 M NaOH containing 0.05 M NaCl. (b) Raman spectrum of the adjacent surface measured under the same conditions as (a). The excitation wavelength was 636.4 nm. Top left inset: MCR-ALS optimization of the spectra, showing the centre of the pit composition to be mostly $Fe_3O_4$ with some δ-FeOOH, and the adjacent surface mostly δ-FeOOH, with some $Fe_3O_4$ and a small amount of $\alpha$-$Fe_2O_3$. The average optimal lack of fit was 1.7 %.

Using MCR-ALS the relative amounts of components in the pit centre were determined to be mainly $Fe_3O_4$ with a small amount of δ-FeOOH, while the adjacent surface contained mostly δ-FeOOH with some $Fe_3O_4$ and a small amount of α-$Fe_2O_3$.

### 6.3.2. Raman spectra of the O-H stretch region

Besides *in situ* spectra of the passive film in the O–H stretch region, Raman spectra were also recorded in the same region for the seven iron oxide compounds ($Fe_3O_4$, α-$Fe_2O_3$, γ-$Fe_2O_3$, α-FeOOH, β-FeOOH, δ-FeOOH, γ-FeOOH) at 514.5 nm and with a reduced laser power of 20 mW (0.3 mW at the sample) to avoid heating of the powders. No bands due to water were detected. However, four peaks at 2633, 2669, 3229 and 3479 $cm^{-1}$ were present in the spectra; these peaks were also present in a spectrum created by light scattering from the surface of a mirror and are therefore instrumentally-induced. They were found to vary linearly in intensity with integration time.

The spectra recorded *in situ* of the O–H stretch region at the different potentials are given in Figure 6.11. They include a spectrum of pure water and the instrumental peaks that could also be created with a mirror as mentioned above. The stronger instrumental peaks at 3229 and 3479 $cm^{-1}$ overlap the spectra of the O–H mode. The weaker instrumental peaks at 2633 and 2669 $cm^{-1}$ are indicated with asterisks and are displayed in an expanded form in the inset. The spectra were normalized such that latter two peaks had the same intensity, the normalized spectra being used for the MCR-ALS analysis. The spectrum of the instrumental peaks at 3229 and 3479 $cm^{-1}$ was subtracted from the raw spectrum to obtain a spectrum of pure water only. The spectra of pure water and the instrument peaks at 3229 $cm^{-1}$ and 3479 $cm^{-1}$ were used as pure spectral components for the MCR-ALS optimization of the spectra.

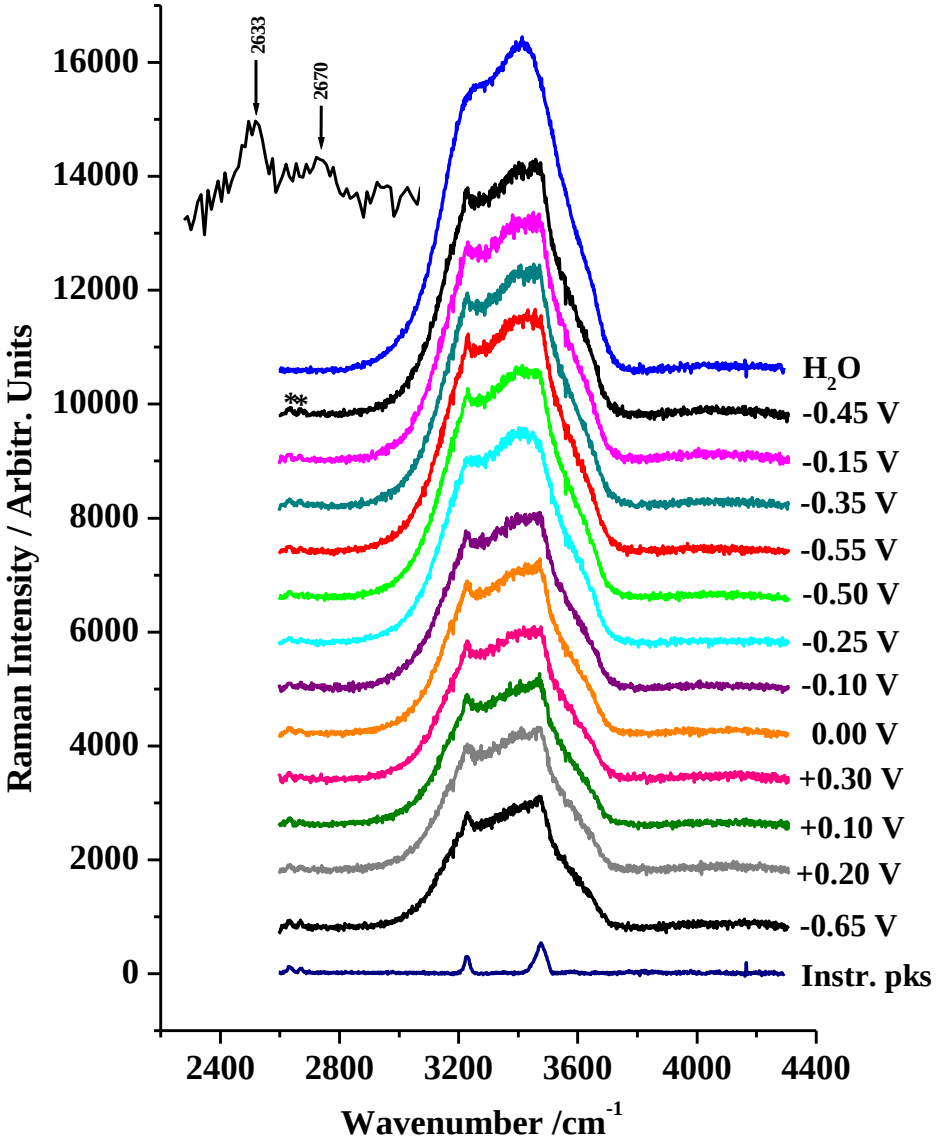


Figure 6.11. Raman spectra recorded *in situ* of the O-H stretch region that provide the $H_2O$ content of the passive film at different potentials in the passive region after addition of 0.05 M NaCl to the 0.05 M NaOH solution. The two instrument peaks at 2633 and 2670 $cm^{-1}$ (marked with asterisks) were used to normalize the Raman spectra; these are shown on an enlarged scale in the inset to the figure. The spectra of pure $H_2O$ and the instrumental peaks at 3229 and 3479 $cm^{-1}$ were used as pure component spectra for the MCR-ALS optimization. The uppermost curve shows the Raman spectrum of the pure $H_2O$ after subtraction of these instrumental peaks.

The relative amounts of water at the respective potentials determined from the MCR-ALS optimization are plotted in Figure 6.12. The average lack of fit for the optimization was 2.0 %.

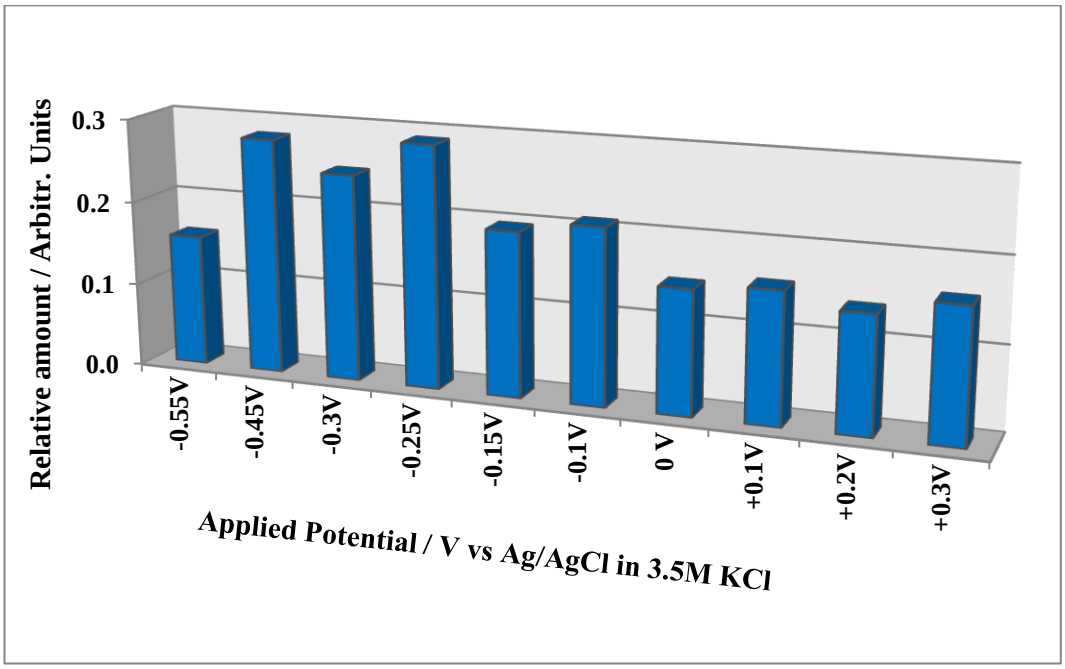


Figure 6.12. Relative amounts of water determined using MCR-ALS optimization from Raman spectra recorded *in situ* of the surface in the passive region at different potentials after addition of 0.05 M NaCl. The average optimal lack of fit was 2.0 %.

## 6.4. DISCUSSION

As shown in Chapter 5 the composition of the passive film in 0.05 M NaOH was found to be highly dependent on the applied potential. At the beginning of the passive region of the anodic potential sweep (–0.55 V) the compounds present on the surface were mainly α-FeOOH, δ-FeOOH and γ-FeOOH, which had formed as a result of oxidation during the anodic sweep. As the potential was increased through the passive region ageing of the FeOOH compounds to γ-$Fe_2O_3$ occurred, accompanied by a decrease in the amount of water incorporated in the film. The Pourbaix diagrams for the iron-water system, shown in Figures 3.8 and 3.9 in Chapter 3.3.1, present the species expected to be stable at different pH values and potentials, determined from thermodynamic considerations [115]. At the electrolyte pH of 12.7 and in the potential region between –0.55 and 0.60 V

(–0.35 and –0.40 V vs SHE) the species $Fe_2O_3.nH_2O$ (or FeOOH) and $Fe_2O_3$ are predicted and they are observed on the surface. At potentials more positive than 0 V (+0.2 V vs SHE), formation of complex aqueous $FeO_4^{2-}$ ions is also thermodynamically favourable. However, due to ageing of FeOOH compounds, a $\gamma$-$Fe_2O_3$ passive film is formed on the surface and this protects the iron from dissolution, which agrees with previous observations.

Figure 6.6 shows the changes in composition of the surface film, determined by the MCR-ALS analysis, from the potential of –0.55 V at which NaCl was added to the 0.05 M NaOH solution through a series of potentials until the final potential of + 0.30 V was attained. With the addition of $Cl^-$ ions at –0.55 V, the most significant effects in comparison with the results obtained previously are the formation of significant amounts of β-FeOOH and the absence of δ-FeOOH and α-FeOOH, these being major components in the film at this potential in the solution without $Cl^-$ ions. As the potential is increased to –0.25 V the formation of Green Complex occurs. γ-FeOOH and $\gamma$-$Fe_2O_3$ are present in relatively small amounts at –0.55 V and increase slightly as the potential is increased to 0 V. It is noted that a similar increase in these components was observed at these potentials in the absence of $Cl^-$ ions (Chapter 5). It can be seen from Figure 6.6 that as the pitting potential of +0.1 V is reached, significant changes occur in the composition of the film: β-FeOOH and $\gamma$-$Fe_2O_3$ decrease considerably and the amount of Green Complex decreases after a maximum is reached at 0 V. Simultaneously δ-FeOOH begins to form and increases in amount with further increases in potential. In the absence of $Cl^-$ ions the amount of δ-FeOOH was observed to decrease at potentials greater than 0 V while at the most positive potentials of the passive region the amount of $\gamma$-$Fe_2O_3$ increased. The addition of $Cl^-$ ions therefore affects the way the composition of the passive film changes with increasing potential.

Another change observed in the neighbourhood of the pitting potential was a decrease in the amount of water incorporated in the passive film, as shown in Figure 6.12. A similar decrease in water content was observed around the same potential without the addition of $Cl^-$ ions which suggests that the decrease in water content in the surface film is a result of the increased anodic potential. The initial increase in the amount of water observed with increasing anodic potential

followed by a decrease at high5er anodic potentials agrees with observations during previous ellipsometry studies [25,33]. In a reflectivity study [45] it was found that the higher refractive index of the passive film corresponding to higher anodic potentials is due to dehydration induced by the high anodic electric field.

However, in the present case, the migration of $Cl^-$ ions to the anodic surface would increase under the influence of higher anodic potentials. This may also contribute to the removal of the bound water molecules by forming chloride-containing iron complexes as proposed in the Hydrated Polymeric Model [30].

As already described earlier in Chapter 1, Section 1.3.3, different roles have been suggested for the water incorporated in the passive film in the pitting of iron in the presence of $Cl^-$ ions. In some studies the water has been described as facilitating pitting by providing paths for migration of the $Cl^-$ ions [25] while in other studies the water incorporated in the film has been suggested to play a protective role [47,48]. Mössbauer studies [32,45,52] inferred that the passive film has an amorphous character which is due to incorporation of water. The presence of water in the passive film was found to result in an increase in the Fe-O distance, suggesting that the H atoms introduced can lead to increased structural flexibility by forming M-OH bonds in addition to M-O bonds, which would promote a more glass-like structure for the film [47]. The amorphous nature of the film afforded by the bound water prevents $Fe^{2+}$ from diffusing from the metal base to hydration sites at the oxide/solution interface [48].

In a kinetic study of localized corrosion of stainless steel in the presence of $Cl^-$ ions [81] two reactions were described to occur simultaneously at the passive film surface with $Fe^{2+}$ ions which have moved through the oxide film to the film/solution phase boundary and the electrolyte:

i) $Fe + 2Cl^- \rightarrow FeCl_2 + 2e^-$

ii) $2Fe + 3H_2O \rightarrow Fe_2O_3 + 6H^+ + 6e^-$.

At the same time, dissolution of the oxide can also occur:

iii) $Fe_2O_3 + 6H^+ + 4Cl^- \rightarrow 2FeCl_2^+ + 3H_2O$.

The last reaction (iii) occurs only at a very slow rate [4, 81], as the dissolution of $Fe_2O_3$ occurs only very slowly even in highly acid solutions. At pH 12.7 it would be able to proceed only under the influence of chloride ions which would render the initiated pit or breakdown area acidic by hydrolysis reactions [4].

As long as the second and third reactions occur at the same rate, the thickness of the oxide film will not change. If the second reaction occurs faster than the third, the oxide film would grow more quickly than it dissolves and the surface would re-passivate; this would be encouraged by increased amounts of water and insufficient chloride concentrations [81]. On the other hand, conditions of decreased amounts of water or increased amounts of chloride ions would enable faster dissolution of the passive film, allowing the formation of stable pits [81]. This mechanism correlates well with both the De-passivation–Re-passivation theory and Chemical Dissolution theory for pit initiation.

The mechanism is further supported by the observations in the present study of a decrease in the amount of water in the neighbourhood of the pitting potential (Figure 6.12) accompanied by a change in composition of the passive film (Figure 6.6). It has previously been established that more chloride is adsorbed on the surface at the pitting sites [7]. With the decrease in water observed from -0.10 V and the decrease in $\gamma$-$Fe_2O_3$, the dynamic equilibrium that existed up to this point between re-passivation assisted by the water molecules incorporated in the film and pitting by the increased amounts of adsorbed chloride at selected sites on the surface may shift toward stable pitting.

It is noted that at the potential of 0 V, in which the amount of water decreases, there is a substantial increase in the Green Complex formation (Figure 6.6). The increase in formation of this hydrated, amorphous complex at this potential is consistent with an increase in the concentration of chloride ions at the surface and occurs at the expense of water available there. The environment afforded by the Green Complex would provide conditions favourable for pitting. The $\delta$-FeOOH formed at the pitting potential may be the oxidized product of $Fe(OH)_2$ formed from secondary reactions of dissolution products, $FeCl_2$ and NaOH [7]. Increased pitting corrosion with increasing anodic potential would result in increasing formation of $\delta$-FeOOH. This would explain the high amount of $\delta$-FeOOH found in the pits as shown in Figures 6.6, 6.7 and 6.8. In a detailed study of the anodic behaviour of iron in borate buffer with added $Cl^-$ ions [20], pitting was found to occur at a particular stage in the formation of the passive film which was suggested to be a transition in the development of the film when the outer phase

was initially forming. This observation corresponds with the formation of δ-FeOOH at the pitting potential in the present study (Figure 6.6).

The present studies indicate that stable pitting is encouraged by a combination of factors which include high anodic potential, decrease in the amount of water in the film and decrease in the amounts of Green Complex, β-FeOOH, γ-FeOOH and γ-$Fe_2O_3$. Information on the events leading up to the pitting potential can be inferred from the composition of the film at the potentials just prior to pitting. Green Complex appears in the film in significant amounts at 0.0 V, just prior to the pitting potential. As mentioned earlier, the Green Complex is a hydrated, amorphous $Fe_3O_4$ compound, in which the iron atoms are present as both $Fe^{2+}$ and $Fe^{3+}$. It has been shown that the stability of the passive film on iron is linked to the $Fe^{2+}$ content of the passive film [149]. The decrease in β-FeOOH, γ-FeOOH and γ-$Fe_2O_3$ may be due to dissolution of the $Fe^{3+}$-containing iron oxide compounds under the influence of chloride ions, resulting in soluble $Fe^{3+}$ and $Fe^{2+}$ complexes which contribute to the formation of the Green Complex. With the increased amount of $Fe^{2+}$ already in the film, an increase in potential to 0.1 V would attract more $Cl^-$ ions to the surface and, with further loss of β-FeOOH, γ-FeOOH and γ-$Fe_2O_3$, stable pitting occurs. This is accompanied by a decrease in the amount of Green Complex and the formation of δ-FeOOH on the surface. From Figure 6.6 it is seen that at the pitting potential the major components of the pits are δ-FeOOH and $Fe_3O_4$. As the anodic potential is increased to +0.30 V (Figure 6.8) the pits consisted mostly of $Fe_3O_4$ with smaller amounts of δ-FeOOH and β-FeOOH. The stabilisation of $Fe_3O_4$ in the pits is probably afforded by restricted oxygen supply in these areas due to rapid build-up of iron oxide compounds such as δ-FeOOH as an outer layer. Other components are also present on the surface at the pitting potential, besides the Green Complex and seven iron oxide and iron oxyhydroxides, as indicated by residual bands from MCR-ALS optimized spectra of a pit surface and surface at +0.1 V. The sharp bands observed between 200 and 350 $cm^{-1}$ are also present in the spectra for many of the other spectra between recorded at the different potentials, and may be due to iron chloride complexes, such as $FeCl_2.20H_2O$ and $FeCl_3.100H_2O$ complexes in the liquid and glassy states which show sharp bands in this region [150]. Although very weak, the residual bands observed between 400 – 600 $cm^{-1}$ for the spectra

recorded at the pitting potential show that some of these components are very similar to those observed in the passive film during its growth in 0.05M NaOH, and are most likely due to $Fe(OH)_2$, $Fe(OH)_3$ and other intermediate complexes which may form during slow oxidation of $Fe(OH)_2$. These components were present in the pit as well.

*Ex situ* spectra of the dried surface in Figure 6.10 show the pit composition to be primarily $Fe_3O_4$ with some δ-FeOOH, while the surface adjacent to the pit indicated mainly δ-FeOOH with some $Fe_3O_4$ and a smaller amount of α-$Fe_2O_3$. However, from the *in situ* data in Figures 6.6, 6.7 and 6.8 neither $Fe_3O_4$ nor α-$Fe_2O_3$ was present on the surfaces adjacent to the pits; instead the composition of the surfaces consisted of various amounts of δ-FeOOH, β-FeOOH, γ-FeOOH, Green Complex and γ-$Fe_2O_3$.

## 6.5. CONCLUSIONS

Raman microscopy with pre-resonance enhancement has been used to examine the composition of the passive film on iron in 0.05 M NaOH (pH 12.7) in the presence of 0.05 M NaCl under conditions of anodic polarisation. MCR-ALS analysis was used to resolve the spectra into seven individual iron oxide and oxy-hydroxide compounds generally found in the passive film under these conditions, namely $Fe_3O_4$ (magnetite), γ-$Fe_2O_3$ (maghemite), α-$Fe_2O_3$ (hematite), α-FeOOH (goethite), β-FeOOH (akaganeite), δ-FeOOH (feroxyhyte), γ-FeOOH (lepidocrocite) and a Green Complex which is a hydrated, amorphous magnetite compound, determined from individual spectra of these components. Hence it was possible to determine the relative amounts of these compounds in the film. MCR-ALS analysis was also used to determine the relative amount of water from spectra recorded in the O–H stretch region.

The composition of the film is influenced by the applied anodic potential, while stable pitting occurs when a combination of conditions is reached. These are reduced water content, a change in composition of the passive film and a sufficiently high anodic potential which results in an increased amount of $Cl^-$ ions at the surface. Prior to stable pitting the film was composed mainly of β-FeOOH, Green Complex and smaller amounts of γ-$Fe_2O_3$ and γ-FeOOH. Just before the pitting potential the amounts of the $Fe^{3+}$- containing components in the passive

film decreased together with a significant increase in the amount of Green Complex, confirming previous studies linking the stability of the passive film with the $Fe^{2+}$ content [149]. At the pitting potential δ-FeOOH was formed and at higher potentials increased in amount, ultimately becoming a major component of the film together with significant amounts of Green Complex. The stable pits which formed were composed mainly of $Fe_3O_4$ with some δ-FeOOH.

The observation at the pitting potential of reduction in amount of water incorporated in the surface and change in composition confirm the mechanism of stable pitting occurring when the passive film is no longer able to maintain re-passivation at the same rate as dissolution by the increased amount of locally adsorbed $Cl^-$ ions. These observations indicate that water plays a protective role in the passive film and reinforce the models for pit initiation based on the De-passivation-Re-passivation theory and Chemical Dissolution theory, described in Appendix A1.4 and A1.8, respectively.

The differences between the *in situ* studies within the electrolyte and *ex situ* investigations when the samples were dried show that while the compositions of the stable pits were comparable in both sets of measurements with the major components being $Fe_3O_4$ and δ-FeOOH, the surface compositions were substantially different. The presence of the electrolyte and *in situ* measurements are thus essential in determining the nature of the passive film and the conditions for the creation of pits.

# CHAPTER 7
# OVERALL CONCLUSIONS AND SUGGESTIONS FOR FURTHER WORK

## 7.1. OVERALL CONCLUSIONS

The unique combination of Raman Microscopy with pre-resonance enhancement and Potentiodynamic Polarization has provided further insights into the composition of the passive film formed on iron in 0.05 M NaOH (pH 12.7), *in situ*, both during its growth and during its localized breakdown in the presence of 0.05 M NaCl.

The added use of Multivariate Curve Resolution with Alternating Least Squares (MCR-ALS) has provided a more accurate method to determine the relative amounts of the different iron oxide compounds in the passive film from the *in situ* Raman spectra. Previous characterizations from Raman spectra in the literature of the relative amounts of different iron oxides and iron oxy-hydroxides in the passive film have not been possible because the bands of these compounds overlap extensively, particularly for $Fe_3O_4$, δ-FeOOH and γ-$Fe_2O_3$. MCR-ALS was also used to monitor changes in the amounts of water in the film from spectra recorded *in situ* in the O-H stretch region, both with and without addition of 0.05 M sodium chloride solution.

The discussion will first deal with the properties of the passive film on iron in 0.05 M NaOH. Although it was not possible to separately analyse different layers of the passive film, the results in the present study are consistent with the concept of a two layer model for the passive film of an inner, high density compound with an outer layer of lower density, in agreement with ellipsometry studies conducted in 0.05M NaOH in the literature [21,26]. The results have also shown that the passive film becomes more hydrated at the beginning of the passive region, corresponding with an increase in relative amounts of δ-FeOOH, α-FeOOH and γ-FeOOH compounds and becomes less hydrated at more anodic potentials well into the passive region, corresponding with an increase in γ-$Fe_2O_3$.

Careful monitoring of the film growth during potentiodynamic polarization at different potentials and over the first 18 cycles has revealed that the passive

film evolves from a more crystalline nature during its initial stages of growth during cycles 1 to 15 to a more amorphous nature over cycles 15 to 18. This observation may explain the different reports of the crystalline/amorphous nature of the passive film given in the literature. The results in this study corroborate the two layer model for the passive film on iron, with $\gamma$-$Fe_2O_3$ forming the inner layer and the outer layer consisting of $\delta$-FeOOH, $\alpha$-FeOOH, $\gamma$-FeOOH and other components such as $Fe(OH)_2$ and other intermediates. The amounts of these components vary with potential and with cycling. In the passive region of anodic polarization the film became increasingly hydrated with increasing anodic potential and with increased cycles became amorphous, comparing well with the Hydrated Polymeric Oxide model for the passive film.

$Fe_3O_4$ was not detected in the spectra and this may be because it is adjacent to the metal surface, forming the innermost part of the inner layer with $\gamma$-$Fe_2O_3$ forming the outermost part. Alternatively, $Fe_3O_4$ may not be present at all, so that $\gamma$-$Fe_2O_3$ is the only component of the inner layer formed on the surface of iron and in crystalline continuity with the metal, protecting the metal from further oxidation and covered with an outer, more loosely bound layer of varying amounts of $\delta$-FeOOH, $\alpha$-FeOOH and $\gamma$-FeOOH. Being a poor conductor, $\gamma$-$Fe_2O_3$ would render the film passive whereas $Fe_3O_4$ is much more conductive and is thus less likely to form a protective, passive film.

The investigation of the composition of the film after addition of $Cl^-$ ions to the 0.05 M NaOH electrolyte has shown that this affects the composition of the passive film and that stable pitting occurs when a combination of conditions is reached. These are reduced water content, a change in composition of the passive film and a sufficiently high anodic potential which would result in increased amounts of $Cl^-$ ions at the surface. Prior to stable pitting, the film was composed mostly of $\beta$-FeOOH and Green Complex with smaller amounts of $\gamma$-$Fe_2O_3$ and $\gamma$-FeOOH. In the neighbourhood of the pitting potential the amounts of these components in the passive film decreased significantly and $\delta$-FeOOH was formed. At higher potentials the amount of $\delta$-FeOOH continued to increase ultimately becoming a major component of the film together with Green Complex. It appears that areas in the passive film composed of predominantly $\delta$-FeOOH would be less resistant to attack by chloride ions than those consisting of $\beta$-FeOOH with Green

Complex and smaller amounts of γ-$Fe_2O_3$ and γ-FeOOH. The significant changes in the composition around the pitting potential occurred along with reduction in hydration, so that re-passivation could no longer be maintained at the same rate as dissolution by the chloride ions, thereby enabling stable pitting. These observations reinforce the models for pitting based on the De-passivation-Re-passivation and the Chemical Dissolution theories.

The results also confirm that bound water in the passive film plays a crucial role in maintaining the delicate balance between activation and re-passivation of pits in the presence of chloride ions. The observation at the pitting potential of reduction in amount of water incorporated in the surface confirms the protective role of water in the passive film.

The differences between the *in situ* studies within the electrolyte and *ex situ* investigations when the samples were dried show that while the compositions of the stable pits were comparable in both sets of measurements with the major components being $Fe_3O_4$ and δ-FeOOH, the surface compositions were substantially different. The presence of the electrolyte and *in situ* measurements are thus essential in determining the nature of the passive film and the conditions for the creation of pits.

The combined use in this study of pre-resonance enhancement of the different iron oxide compounds with MCR-ALS analysis has been shown to enable the identification and more accurate determination of the relative amounts of many of the iron oxides, including those with similar frequencies for the strongest bands. This would be very useful in practical applications, for example, for determination of the lepidocrocite/goethite (L/G) ratio on weathering steel structures, which is an indicator of the progress of formation of stable rust patinas on the surfaces [151]. The use of the MCR-ALS technique with iron oxide spectra as pure component spectra which have been recorded under the same conditions, would lead to a more accurate L/G ratio, and also enable accurate determination of the contribution of other iron oxides present with relatively weaker spectral intensities.

The use of the *in situ* Raman measurements with pre-resonance enhancement in combination with electrochemical control would provide a useful tool for monitoring corrosion products formed on iron in contact with typical environmental electrolytes such as sea water and ground water.

## 7.2. SUGGESTIONS FOR FURTHER WORK

Although significant enhancement of the iron oxides was achieved with the 636.4 nm line of the R6G dye in the tuneable dye laser, this wavelength may not have provided optimum enhancement of the Raman bands. The choice of wavelength was limited by the bandpass width of the 632.8 nm HNF used to filter out the Rayleigh scattering, and using a wavelength closer to the 640 nm absorption band for ligand field transitions of the FeOOH compounds would probably provide even greater enhancement of the Raman spectra and this would be useful to investigate.

It would be valuable to perform similar studies in which the pH and composition of the electrolyte were changed. Similarly the introduction of temperature as an additional variable would provide new insights.

The combination of techniques described in these studies would be well suited for *in situ* studies of the pitting behaviour of passive films on other iron based metals such as carbon steels and stainless steels. The use of other excitation wavelengths could be explored to obtain enhancement of other metal oxides, for example, for Ni, Mo and Cr which are commonly found in stainless steels. Other important metal systems which could be studied using these techniques are Al, Cu and Zn.

# REFERENCES


(1) A.T. Fromhold, Jr. in *Passivity of Metals* Ed. R.P. Frankenthal and J. Kruger, The Electrochemical Society Inc., Princeton, New Jersey, **1978,** 59 - 81.

(2) U.R. Evans, *The Rusting of Iron: Causes and Control*; Edward Arnold Ltd.: London, UK, **1972**; Vol. 7.

(3) N. Sato, *Corrosion Science* (1987) **27**, 421-433.

(4) M. Cohen in *Passivity of Metals* Ed. R.P. Frankenthal and J. Kruger, The Electrochemical Society Inc., Princeton, New Jersey, **1978**, 521-545.

(5) N. Sato in *Passivity of Metals*; Ed. R.P. Frankenthal and J. Kruger, The Electrochemical Society Inc., Princeton, New Jersey **1978**, 29-58.

(6) Z. Szklarska-Smialowska, *Pitting Corrosion of Metals*; NACE: Houston, Texas, **1986**.

(7) C.-J. Lin, R.-G. Du and T. Nguyen *Corrosion* (2000) **56**, 41-47.

(8) E.E. Stansbury and R.A. Buchanan, *Fundamentals of Electrochemical Corrosion*; 1st ed.; ASM International, Materials Park Ohio, USA, **2000**

(9) J.R. Galvele, J. Electrochemical Society (1976) **123**, 464-474.

(10) J. Dünnwald, R. Lossy and A. Otto in *Passivity of Metals and Semiconductors,* Froment M, Ed., Elsevier Science: Amsterdam, **1983**, 107-112.

(11) M. Froelicher A. Hugot -Le Goff, C.Pallotta, R.Dupeyrat and M.Masson in *Passivity of Metals and Semiconductors* M.Froment, Ed., Elsevier Science: Amsterdam, **1983**, 101-105.

(12) J. Dünnwald R. Lossy and A. Otto *Fresenius' Zeitschrift fuer Analytische Chemie* (1984) **319**, 738-742.

(13) J.C. Rubim and J. Dünnwald *Journal of Electranalytical Chemistry and Interfacial Electrochemistry* (1989) **258**, 327-344.

(14) J.C. Rubim *Journal of the Chemical Society, Faraday Transactions 1* (1989) **85**, 4247-4258.

(15) J. Gui and T.M. Devine *Journal of the Electrochemical Society* (1991) **138**, 1376-1384.

(16) C.A. Melendres. M. Pankuch Y.S. Li and R.L. Knight *Electrochimica Acta* (1992) **37,** 2747-2754.

(17) M.S. Odziemkowski T.T. Schuhmacher, R.W.Gillham and E.J.Reardon *Corrosion Science* (1998) **40**, 371-389.

(18) N. Boucherit A. Hugot-Le Goff and S. Joiret , *Corrosion Science* (1991) **32**, 497-507.

(19) P. Allongue and S. Joiret, *Physical Review B*, (2005) **71**, 115407/1-115407/7.

(20) B. MacDougall and J.A. Bardwell, *Journal of the Electrochemical Society*, (1988) **135**, 2157-2161.

(21) Z.Q. Huang and J.L. Ord *Journal of the Electrochemical Society* (1985) **132**, 24-28.

(22) R.S. Guzman Schrebler, J.R. Vilche and A.J. Arvia *Electrochimica Acta*, (1979) **24**, 395-403.

(23) D.D.Macdonald and B. Roberts, *Electrochimica Acta*, (1978) **23**, 557-564.

(24) D.D.Macdonald and B. Roberts, *Electrochimica Acta* (*1978*) **23**, 781-786.

(25) T. Zakroczymski, C-J. Fan and Z. Szklarska-Smialowska, *Journal of the Electrochemical Society* **(**1985) **132**, 2868-2871.

(26) T. Zakroczymski C-J. Fan and Z. Szklarska-Smialowska, *Journal of the Electrochemical Society* (1985) **132**, 2862-2867.

(27). T. Ohtsuka, J.-C. Ju, S. Ito and H. Einaga *Corrosion Science* (1994) **36**, 1257-1266.

(28) H. Konno and M. Nagayama in *Passivity of Metals*, Ed. R.P. Frankenthal and J. Kruger, The Electrochemical Society Inc., Princeton, New Jersey, **1978**, 585-606.

(29) N. Sato *Corrosion Science* (1990) **31**, 1-19.

(30) J. O'M. Bockris *Corrosion Science* (1989) **29**, 291-312.

(31) S. Matsuda, K. Sugimoto and Y. Sawada in *Passivity of Metals*; Ed. R.P. Frankenthal and J. Kruger, The Electrochemical Society Inc., Princeton, New Jersey, **1978**, 699-713.

(32) W.E. O'Grady, *Journal of the Electrochemical Society* (1980) **127**, 555-563.

(33) N. Sato *Journal of the Electrochemical Society* (1982) **129**, 260-264.

(34) M. Nagayama and M. Cohen, *Journal of the Electrochemical Society* (1962) **109**, 781-790.

(35) A.J. Davenport, L.J. Oblonsky, M.P. Ryan and M.F. Toney *Journal of the Electrochemical Society* **(**2000) **147**, 2162-2173.

(36) M.P. Ryan, R.C. Newman and G.E. Thompson, *Journal of the Electrochemical Society* (1995) **142**, L177-L179.

(37) G. Okamoto and T. Shibata, *Corrosion Science* (1970) **10**, 371-378.

(38) W.E. O'Grady and J.O'M. Bockris, *Surface Science* (1973) **10**, 249-251.

(39) N. Sato, K. Kudo and R. Nishimura *Journal of the Electrochemical Society* (1976) **123**, 1419-1423.

(40) A. Hugot-Le Goff, J. Flis, N. Boucherit, S. Joiret and J. Wilinski *Journal of the Electrochemical Society* (1990) **137,** 2684-2690.

(41) V. Schroeder and T.M. Devine, *Journal of the Electrochemical Society*, (1999) **146**, 4061-4070.

(42) I. Díez-Pérez P. Gorostiza, F. Sanz and C. Müller *Journal of the Electrochemical Society* (2001) **148**, B307-B313.

(43) A.J. Davenport, J.A. Bardwell and C.M. Vitus *Journal of the Electrochemical Society* (1995) **142**, 721-724.

(44) N. Sato, K. Kudo and T. Noda *Electrochimica Acta* (1971) **16**, 1909-1921.

(45) T. Misawa, K. Hashimoto and S. Shimodaira *Corrosion Science* (1974), **14**, 131-149.

(46) U.R. Evans *The Corrosion and Oxidation of Metals*; Edward Arnold Ltd., London, **1976**.

(47) J. Kruger *Corrosion Science* (1989) **29**, 149-162.

(48) T.E. Pou, O.J. Murphy, V. Young and J. O'M. Bockris *Journal of the Electrochemical Society* (1984) **131**, 1243-1251.

(49) V. Rives and M. Angeles Ulibarri *Coordination Chemistry Reviews* (1999) **181**, 61-120.

(50) V. Jovancicevic, R.C. Kainthla, Z. Tang, B. Yang and J. O'M. Bockris *Langmuir* (1987) **3**, 388-395.

(51) R.W. Revie, J.O'M. Bockris and B.G. Baker *Surface Science* (1975) **52**, 664-669.

(52) T. Misawa K. Hashimoto and S. Shimodaira *Journal of Inorganic Nuclear Chemistry* (1973) **35**, 4167-4174.

(53) C. Gabrielli, S. Joiret, M. Keddam, H. Perrot, N. Portail, P. Rousseau and V. Vivier *Journal of the Electrochemical Society* (2006) **153,** B68-B74.

(54) L.J. Oblonsky S. Virtanen, V. Schroeder and T.M. Devine *Journal of the Electrochemical Society* (1997) **144**, 1604-1609.

(55) S. Haupt and H.H. Strehblow *Corrosion Science* (1989) **29**, 163-182.

(56) C. Lukac, J.B. Lumsden, S. Smialowska and R.W. Staehle *Journal of the Electrochemical Society* (1975) **122**, 1571-1579.

(57) J.A. Bardwell, B. MacDougall and M.J. Graham *Journal of the Electrochemical Society* (1988) **135**, 413-418.

(58) Y.M. Kolotyrkin *Journal of the Electrochemical Society* (1961) **108**, 209-216.

(59) H.P. Leckie and H.H. Uhlig *Journal of the Electrochemical Society* (1966) **113**, 1262-1267.

(60) T.P. Hoar and W.R. Jacob *Nature* (1967) **216**, 1299-1301.

(61) E. McCafferty *Journal of the Electrochemical Society* (1990) **137**, 3731-3737.

(62) J.A. Richardson and G.C. Wood *Journal of the Electrochemical Society* (1973) **120**, 193-202.

(63) K. Hashimoto and K. Asami *Corrosion Science* (1979) **19**, 251-260.

(64) M. Janik-Czachor and Z. Szklarska-Smialowska *Corrosion Science* (1971) **11**, 901-914.

(65) J. Kruger in Passivity and its Breakdown on Iron and Iron-Base Alloys, NACE, Houston, **1976**, 91-98.

(66) M.A. Heine, D.S. Keir and M.J. Pryor *Journal of the Electrochemical Society* **(**1965) **112**, 24-32.

(67) M.J. Pryor in *Localized Corrosion*; Ed. R.W. Brown, B.F. Brown and J. Kruger, Ed.; NACE: Houston, Texas, **1974,** 2-9.

(68) G. Okamoto and T. Shibata, in *Passivity of Metals*; Ed. R.P. Frankenthal and J. Kruger, The Electrochemical Society Inc., Princeton, New Jersey, **1978**, 646-677.

(69) T.P. Hoar *Corrosion Science* (1967) ***7***, 341-355.

(70) N. Sato *Electrochimica Acta* (1971) **16**, 1683-1692.

(71) N. Sato *Journal of the Electrochemical Society* **(**1982) **129**, 255-260.

(72) L.F. Lin, C.Y. Chao and D.D. MacDonald *Journal of the Electrochemical Society* (1981) **128**, 1194-1198.

(73) D.D. MacDonald *Journal of the Electrochemical Society* (1992) **139**, 3434-3449.

(74) G. Okamoto *Corrosion Science* (1973) **13**, 471-489.

(75) P.C. Pistorius, Thesis, St. John's College, University of Cambridge, UK, **1991**.

(76) J.R. Galvele in *Passivity of Metals*; Ed. R.P. Frankenthal and J. Kruger, The Electrochemical Society Inc., Princeton, New Jersey, **1978**, 285-327.

(77) N. Sato *Corrosion Science* (1987) **27**, 421-433.

(78) P. Zaya and M.B. Ives in *Passivity of Metals and Semiconductos*; Ed. M.Froment, Elsevier: Amsterdam, **1983**, 287-292.

(79) J. Kruger, *International Materials Reviews* (1988) **33,** 113-130.

(80) T. Ohtsuka, K. Azami and N. Sato *Corrosion Science* (1990) **31**, 155-160.

(81) J. Tousek *Corrosion Science* (1978) **18** , 53-59.

(82) S. Simard, M. Odziemkowski, D.E. Irish, L. Brossard and H. Menard *Journal of Applied Electrochemistry* (2001) **31**, 913-920.

(83) C. Ruby, A. Gehin, M. Abdelmoula, J-M.R. Genin and J-P. Jolivet *Solid State Sciences* (2003) **5**, 1055-1062.

(84) J. M. Genin, P. Bauer, A.A. Olowe and D. Rezel *Hyperfine Interactions* (1986) **29**, 1355-1360.

(85) L. Rongguang, R. Srinivasan R.L. Spicer, and B.H. Davis *Colloids and Surfaces A. Physiochemcial and Engineering aspects* (1996) **113**, 97-105.

(86) N. Boucherit and A. Hugot-Le Goff *Faraday Discussions* (1982) **94**, 137-147.

(87) Ph. Refait, J-B. Memet, C. Bon, R. Sabot and J.-M.R. Genin *Corrosion Science* (2003) **45**, 833-845.

(88) Ph. Refait, M. Abdelmoula and J.-M.R. Genin *Corrosion Science* (1998) **40,** 1547-1560.

(89) Ph. Refait and J.-M.R. Genin *Corrosion Science* (1993) **34**, 797-819.

(90) M.M. Scherer and A.G.B. Williams *Environmental Science and Technology* (2004) **38**, 4782-4790.

(91) K. Ritter, M.S. Odziemkowski and R.W. Gillham *Journal of Contaminant Hydrology* (2002) **55**, 87-111.

(92) M. Pascale, L. Bonin, W. Jedral, M.S. Odziemkowski and R.W. Gillham *Corrosion Science* (2000) **42**, 1921-1938.

(93) I.R. McGill, B. McEnaney and D.C. Smith *Nature* (1976) **259**, 200-201.

(94) N. Boucherit, A. Hugot Le-Goff and S. Joiret *Corrosion* (1992) **48**, 569-579.

(95) N. Boucherit and A. Hugot Le-Goff *Faraday Discussions* (1992) **94**, 137-147.

(96) Ph. Refait and J.-M.R. Genin *Corrosion Science* (1994) **36**, 55-65.

(97) M.G.S. Ferreira, T.M. e Silva, A. Catarino, M. Pankuch and C.A. Melendres *Journal of the Electrochemical Society* (1992) **139**, 3146-3151.

(98) D. Thierry, D. Persson, C. Leygraf, D. Delichere, S. Joiret, C. Pallotta and A. Hugot-Le Goff *Journal of the Electrochemical Society* (1988) **135**, 305-310.

(99) D.Thierry, D.Massinon and A. Hugot-Le Goff *Journal of the Electrochemical Society* (1991) **138**, 879-880.

(100) C. Kumai and T.M. Devine, *Corrosion* (2005) 61, 201 - 218.

(101) S. Joiret, M. Keddam, X.R.Novoa, M.C. Perez, C. Rangel and H. Takenouti *Cement and Concrete Composites* (2002) **24**, 7-15.

(102) W.-C. Baek, T. Kang, H.-J. Sohn and Young Tai Kho, *Electrochimica Acta* (2001) **46**, 2321-2325.

(103) J.E. Maslar, W.S. Hurst, W.J. Bowers, J.H. Hendricks and M.I. Aquino *Journal of the Electrochemical Society* (2000) **147**, 2532-2542.

(104) I.M. Geronov, T. Tomov and S. Georgiev *Journal of Applied Electrochemistry* (1975) **5**, 351-358.

(105) D.A. Long *Raman Spectroscopy*; McGraw-Hill: London, UK, **1977**.

(106) N.B. Colthup, L.H. Daly and S.E. Wiberley *Introduction to Infrared and Raman Spectroscopy*; Academic Press: New York, **1964**.

(107) J.R. Ferraro and K. Nakamoto *Introductory Raman Spectroscopy,* 6th edition Academic Press Limited, London, **1994**.

(108) G. Keresztury in *Handbook of Vibrational Spectroscopy Theory and Instrumentation*, *Volume 1,* Ed. J.M. Chalmers and P.R. Griffiths, Wiley, Chichester, UK, **2002**.

(109) D.P. Strommen and K. Nakamoto, *Journal of Chemical Education*, (1977) **54**, 474-478.

(110) Raman Tutorial, Kaiser Optical System Incorporated,

http://www.kosi.com/raman/resources/tutorial/index.html.

(111) Jobin-Yvon T64000 System User Manual Part. No. 31 087 018, **1992**.

(112) F.G. Smith and T.A. King, *Optics and Photonics: An Introduction*, John Wiley & Sons, Ltd., Chichester: UK **2000.**

(113) P.W. Atkins *Physical Chemistry*, 3rd Ed.; W.H. Freeman, New York, **1986**.

(114) Spectra-Physics *Instruction Manual for Model 375 Dye Laser with Model 376 Dye Circulator*, Spectra-Physics, **1978**.

(115) M. Pourbaix, Atlas of Electrochemical equilibria in aqueous solutions; 2nd English ed. ; Pergamon Press: Oxford, UK, **1974**.

(116) J.A. von Frauenhofer and C.H. Banks *Potentiostat and its Applications*; Butterworths: London, **1972**.

(117) J.E. Harrar and I. Shain *Analytical Chemistry* (1966) **38**, 1148-1158.

(118) J. Jaumot, R. Gargallo, A. de Juan and R. Tauler *Chemometrics and Intelligent Laboratory Systems* (2005) **76**, 101-110.

(119) M.K. Nieuwoudt, J.D. Comins and I. Cukrowski, *J. Raman Spectroscopy* (2011) **42**, 1335-1339.

(120) D.L.A. de Faria, S.V. Silva and M.T. de Oliviera *Journal of Raman Spectroscopy* (1997) **28**, 873-878.

(121) I.R. Beattie and T.R. Gilson *Journal of the Chemical Society A. Inorganic, Physical, Theoretical* (1970) **6**, 980-986.

(122) M.J. Graham J.A. Bardwell, R. Goetz, D.F. Mitchell and B. MacDougall *Corrosion Science* (1990) **31**, 139-148.

(123) D.D. MacDonald and D. Owen *Journal of the Electrochemical Society* (1973) **120**, 317-324.

(124) M. Stratmann, K. Bohnenkamp and H.J. Engell *Corrosion Science* (1983) **23**, 969-985.

(125) S.J. Oh, D.C. Cook, and H.E. Townsend, *Hyperfine Interactions* (1998) **112**, 59-65.

(126) M. Refass, R. Sabot, C. Savall, M. Jeannin, J. Creus and Ph. Refait, *Corrosion Science* (2006) **48**, 709-726.

(127) M. Reffass, R. Sabot, M. Jeannin, C. Berziou and Ph. Refait, *Electrochimica Acta* (2007) **52**, 7599-7606.

(128) M. Langumier, R. Sabot, R. Obame-Ndong, M. Jeannin, S. Sablé and Ph. Refait, *Electrochimica Acta* (2009) **54**, 4389-4396.

(129) U. Schwertmann and R.M. Cornell, *Iron oxides in the laboratory, preparation and characterization*, VCH, Weinheim, **1991**.

(130) Ph. Colomban, S. Cherifi and G. Despert, *Journal of Raman Spectroscopy* (2008) **39**, 881-886.

(131) F. Froment, A. Tournie and P. Colomban, *Journal of Raman Spectroscopy* (2008) **39**, 560-568.

(132) T. Ohtsuka, *Materials Transactions, Japan Institute of Metals* (1996) **37**, 67-69.

(133) S. Réguer, D. Neff, L. Bellot-Gurlet and Ph. Dillmann, *Journal of Raman Spectroscopy* (2007) **38**, 389-397.

(134) A.P. Lee, J. Webb, D.J. Macey, W.van Bronswijk, A.R. Savarese and G.C. de Witt *Journal of Biological and Inorganic Chemistry* (1998) **3**, 614-619.

(135) D. Neff, L. Bellot-Gurlet, P. Dillmann, S. Reguer and L. Legrand *Journal of Raman Spectroscopy* (2006) **37**, 1228-1237.

(136) J.T. Keiser and C.W. Brown *Corrosion Science* (1983) **23**, 251-259.

(137) D.M. Sherman and T.D. Waite, *American Mineralogist* (1985) **70**, 1262-1269.

(138) M.K. Nieuwoudt, J.D. Comins and I. Cukrowski *Journal of Raman Spectroscopy* (2011) **42**, 1353-1365.

(139) R. Paterson, H. Rahman *Journal of Colloid and Interface Science* (1983) **94**, 60-69.

(140) H.D. Lutz, H. Möller and M. Schmidt, *Journal of Molecular Structure* (1994) **328**, 121-132.

(141) L.J. Simpson and C.A. Melendres *Electrochimica Acta* (1996) **41**, 1727-1730.

(142) J. Gui and T.M. Devine *Corrosion Science* (1991) **32**, 1105-1124.

(143) F.C. Ho and J. L. Ord *Journal of the Electrochemical Society* (1972) **119**, 139-145.

(144) J.L. Ord and D.J. De Smet *Journal of the Electrochemical Society* (1976) **123**, 1876-1882.

(145) I.C. Thanos *Electrochimica Acta* (1986) **31**, 811-823.

(146) C.L. Foley, J. Kruger and C.J. Bechtoldt *Journal of the Electrochemical Society* (1967) **114**, 994-1000.

(147) F.A. Cotton and G.W. Wilkinson *Advanced Inorganic Chemistry, A Comprehensive Text*, 3rd ed., John Wiley and Sons, Inc., New York, **1972**.

(148) M.K. Nieuwoudt, J.D. Comins and I. Cukrowski *Journal of Raman Spectroscopy* (2012) **43**, 928-938.

(149) W S. Li, J.L. Luo *International Journal of Electrochemical Science* (2007) **2**, 627-665.

(150) H. Kanno, J. Hiraishi, *Journal of Raman Spectroscopy* (1982) **12**, 224 – 227.

(151) J. Aramendia, L. Gomez-Nubla, K. Castro, I. Martinez-Arkarazo, D. Vega, A. Sanz López de Heredia, A. García Ibáñez de Opakua, J. M. Madariaga, *Journal of Raman Spectroscopy*, DOI: 10.1002/jrs.3158.

# APPENDICES

## APPENDIX 1: THEORIES OF PITTING CORROSION

In this section a summary is presented of a review [6,47] of the different theories proposed for the mechanism of pitting of passive films on metals.

### A1.1 Adsorption Theory

This model proposes that a competitive adsorption occurs between $Cl^-$ ions and $O^{2-}$ ions in the formation of pits, which will develop at sites where adsorbed $O^{2-}$ is displaced by $Cl^-$. However, the adsorption of $Cl^-$ ions on uncovered sites on the surface leading to breakdown does not explain the induction time observed for pitting. Also, the observed relationship between induction time and film thickness is not adequately explained by this model.

### A1.2 Anion penetration and migration theories

These models propose that $Cl^-$ ions permeate through the protective oxide film, and that breakdown of the passive film occurs when the aggressive anion reaches the bare metal. The first step to passivity breakdown is the adsorption of $Cl^-$ ions on the oxide film. Permeation may occur in different ways:

The diffusion of $Cl^-$ ions by way of dislocations from the electrolyte/oxide to the oxide/metal surface;

The entry of anions under the influence of the electrostatic field across the film/solution interface when the field reaches a value corresponding to *Ep*. However, migration of $O^{2-}$ ions in the reverse direction is impossible;

The exchange of $O^{2-}$ by $Cl^-$ ions at sites where the metal-O bond is weakest. $Cl^-$ ions that displace $O^{2-}$ ions from inside the oxide surface penetrate the passive film and agglomerate inside the pits, leading to crevice corrosion;

The migration of $Cl^-$ ions to create anion vacancies and the exchange of $Cl^-$ ions with $O^{2-}$ and $OH^-$. The induction time is the time for migration of $Cl^-$ ions through discrete defects in the film to bare metal. *Ep* is the potential at which $Cl^-$ ions are adsorbed onto the passive film.

The migration of $Cl^-$ ions assisted by bound water in the passive film: this assumes a passive film as a hydrated oxide with a gel-like structure. Three different bridges are possible in the film: $H_2O$-M-$OH_2$, HO-M-OH, and O-M-O.

Hydrated oxide films have a strong buffering ability that prevents film breakdown because of their good repairing action assured by the abundance of water molecules in the structure of the film. In contrast a well-developed oxide which has lost protons has less capacity to repair the film destroyed by $Cl^-$ ions. The $Cl^-$ ions adsorbed on the surface then migrate to the film under the electric field and replace the water molecules so that no repair of the film occurs. Alternatively, the reaction between the metal ions and $Cl^-$ ions proceeds to form solvated ions or salt-like films.

This migration theory is supported by the following:

(1) reflection electron diffraction methods which indicate that anodic films have an amorphous or microcrystalline structure and are composed of a hydrous oxide;

(2) a longer passivation time that leads to smaller contents of bound water, and at potentials above a certain value the bound water content is less than at lower potentials,

(3) the induction time for pit nucleation decreases after ageing, as a result of expulsion of bound water molecules from the film.

The anion penetration and migration theories are contradicted by the following arguments:

Nucleation is too fast to be explained by migration through a continuous oxide film;

The diameters of $Cl^-$ ions and $O^{2-}$ ions are larger than that of $Fe^{3+}$ so their transport through $\gamma$-$Fe_2O_3$ should be less rapid; and pitting under the influence of other anions such as $SO_4^{2-}$cannot occur in this way as they would be too large.

### A1.3 Mechano-chemical models

Changes in the interfacial forces of the film result in the film being mechanically stressed and damaged by pores and flaws. If the electrolyte inside the pores remains neutral, formation of insoluble hydroxide leads to re-passivation. But if hydrolysis results in acidification of the electrolyte, this leads to migration of $Cl^-$ ions and auto-catalysis. Formation of pits in the passive film is facilitated by weak sites such as flaws or pores in the oxide film. This model

describes the pitting potential as the potential at which adsorption of $Cl^-$ ions occurs at the bare metal at the base of pores.

In another model the adsorbing $Cl^-$ ions replace water and reduce the interfacial tension of the oxide/solution interface by mutually repulsive forces between the charged particles. Repulsion of the anions breaks up the oxide layer.

Another model suggests that passivity breakdown occurs as the film attains a thickness, L, at which mechanical stresses become critical as a result of electrostriction pressure (dielectric deformation resulting from precipitating opposite charges by the electric field). The $Cl^-$ ions reduce the surface forces that counteract electrostriction by adsorption. In this model the critical pitting potential is described as the potential above which this electrostriction pressure exceeds the compressive stress resulting in film breakdown.

The weakness of this model is that mechanical breakdown of the film is not sufficient for pit initiation, and it is based on the assumption that pores and flaws are equally distributed in the film.

### A1.4 Point defect model for pit initiation

This model [73] assumes that the passive film forms bilayers, with a highly disordered inner adjacent to the metal (barrier layer) containing numerous point defects and an outer film comprised of a precipitate layer that may incorporate anions and/or cations from the solution. Passivity is attributed to the barrier layer. During film growth, anions diffuse from the film/solution interface to the metal/film interface. Cations diffuse but do not contribute to film growth; they result in dissolution, thereby creating metal vacancies at the metal/film interface. These submerge into the metal and disappear, but when the cation diffusion rate exceeds the rate of vacancy submergence, the metal vacancies generate voids. When these voids reach a critical size they cause the passive film to suffer local collapse. In the presence of $Cl^-$ ions, film breakdown occurs more easily because the $Cl^-$ ions incorporate into the outer layer by occupying vacancies in the film. Increasing $Cl^-$ ion concentration and an increasing electric field result in an increase in cation vacancies which pile up at the metal/film interface leading to localized breakdown.

### A1.5 Local acidification theory [9]

According to this theory pits develop at micro pits already on surface because hydrolysis of corrosion products occurs at these sites causing acidification. The corrosion products are transported by diffusion. A low pH of the pit solution is one of the critical factors in maintaining pit growth. Film breakdown occurs constantly even below *Ep.* When a crack in the passive film is produced and the electric field is high enough, metal dissolution occurs followed by hydrolysis:

$$M = M^{n+} + ne^-$$

$$M^{n+} + nH_2O = M(OH)_n + nH^+$$

The pH inside the pit drops; for each metal a critical acidification is necessary to sustain pit activity and prevent re-passivation. Acidification depends on $I \times X$, where I = current density and X = pit depth. The critical acidification is assumed to be equal to the pH at which the passivating oxide film is in equilibrium with a metal ion concentration of $10^{-6}$ M. The induction time is that necessary to achieve the critical pH in the pits. According to this model the critical pitting potential of a metal can be evaluated from its anodic behaviour in a low-pH solution. However, a limitation of this theory is that it does not explain the lack of effect of pH on the critical pitting potential for many metals. The attainment of a critical pH in a fissure is insufficient to initiate pitting in stainless steel and Cr. Also, it does not explain the specific action of $Cl^-$ ions, nor the increase of induction time with increasing film thickness.

### A1.6 Chemical dissolution theories

It is accepted that any mechanism of passivity or iron dissolution should include consideration of the formation and existence of metal-anion complexes. A stable insoluble species would inhibit corrosion and a transient, readily dissociable complex would accelerate corrosion. All the models in this group assume that metal dissolution occurs by transient complex formation.

In one model $Cl^-$ ions are directly involved in the anodic process. In neutral solutions the $Cl^-$ ions form iron-chloride complexes that dissociate and remove $Fe^{2+}$ from the surface. Three or four $Cl^-$ ions jointly adsorb on the oxide surface around a lattice cation, with one next to a surface anion vacancy. This transitional

complex has high energy and its probability of formation will be slight. Once formed however, the complex can readily separate from the lattice, with the cation dissolving more readily in the solution than the non-complexed cations in the film surface in the absence of $Cl^-$ ions. Under a high anodic field, a further cation comes up to replace the missing one. The field increases at the thinned point of the film. Upon arriving at the film/solution interface, rather than a stabilising oxide forming, the cation finds several $Cl^-$ ions, so the process accelerates because of the increasing field. Pits are thought to nucleate at defects in the film where the oxide thickness is smaller and the potential difference across the oxide/solution is higher. This supports the observed increase in induction time with film thickness but it does not explain the critical pitting potential. In this model the pitting potential is described to be a potential sufficiently negative to prevent adsorption of halide ions.

In another chemical model the thickness of the passive film decreases during pit initiation and the current density for iron dissolution results from consumption of the passivating $\gamma$-$Fe_2O_3$ layer. The passive film disappears locally at the critical pitting potential. It is assumed that pit nucleation starts with chemisorption of $Cl^-$ ions replacing $O^{2-}$ or $OH^-$ ions at the oxide surface and the formation of two-dimensional nuclei of chloride salt on the passivated surface.

Another model considers the reduction of film thickness at sites where $Cl^-$ions agglomerate. Above the critical potential, transpassive, potential-dependent dissolution occurs. This potential is lower at $Cl^-$ ion adsorption sites and is affected by the electronic properties of the passive film, and hence by the electron acceptor levels introduced by anion adsorption as well as by the dislocation-induced electron levels. Pitting only occurs when a critical concentration of aggressive anions and a critical acidity is locally built up.

A yet further model is based on fact that slow dissolution of the passive film occurs in the anodic range with the release of cations, which occurs faster at locally defective sites than elsewhere. The $Cl^-$ ions migrate to these sites forming chloride salts. Hydrolysis and a high concentration of $Cl^-$ ions result in local acidification which accelerates passive film dissolution below these islets of chloride salts. When the local pH attains a value at which the chloride salt is precipitated at the bottom of the pit, re-passivation is prevented and pit growth continues because the salt layer does not protect the metal from corrosion.

### A1.7 Thermodynamic theory of pitting

Pitting initiates on the surface of a nonporous oxide film with salt nuclei. The exit of $Fe^{2+}$ ions from the passive film is assisted by a strong electric field and accelerated by the presence of $Cl^{-}$ ions at the surface. At potentials more positive than the pitting potential an iron chloride salt layer tends to form instead of an iron oxide layer, whereas at potentials more negative than pitting potential the opposite is true. Equilibrium between the iron oxides and salt on the metal surface may be achieved when both layers have the same potential and when an equilibrium exists between the $Fe^{2+}$ cations and the electrons in these layers. This equilibrium is achieved when the activity of the anion in the pit has been increased by the potential difference between the inside and outside of the pit. In this model the pitting potential is described as the potential at which this equilibrium is achieved, and is higher than the potential for $Fe \rightarrow Fe^{2+} + 2e^{-}$. Calculations agree well with experimental values for some metals but not for others.

### A1.8 De-passivation – re-passivation theory

This model is a modification of the competitive adsorption theory between $Cl^{-}$ ions and $O^{2-}$ ions on the metal surface; it assumes that competition exists between film formation and film dissolution. A dynamic breakdown and repair of the passive film occurs, and in the absence of $Cl^{-}$ ions the defects formed at sites of localized dissolution in the passive film are rapidly healed, while in presence of $Cl^{-}$ ions, at sufficiently high potentials, the metal surface becomes activated at these defective sites and attacked by formation of soluble corrosion products. Pitting occurs at potentials where the breakdown of passivity is greater than re-passivation. In pits that are in an active state local metal dissolution occurs most intensively at the bottom of the pit, while the pit mouth area tends to be re-passivated, because of the gradient in pH generated along the pit depth.

### A1.9 Bipolar Ion Selective theory [77]

In this model the passive layer is produced by the bipolar nature of the ion-selective precipitate film on the metal. The metal is covered with a porous corrosion-precipitate of hydrated metal oxides or insoluble metal salts, which

accelerates or decelerates further corrosion of the underlying metal. For localized anodic dissolution to occur under a precipitate film there must be some ionic species migrating through the film: in alkaline solution the hydrated iron oxides are cation selective. From membrane theory the ion selective property of a membrane is determined by the sign and concentration of the fixed charge of preferentially adsorbed ions in the membrane, and will be cation selective if the fixed charge is negative. $Cl^-$ ions are prevented from migrating into the inner solution; instead, $H^+$ migrate out of the occluded solution leaving dissolved $Fe^{2+}$. Due to a water concentration gradient $H_2O$ will diffuse inward, metal hydroxides will form in the occluded solution, and corrosion will be retarded. If the corrosion precipitate possesses a bipolar character with an anion-selective layer on the metal side and a cation-selective layer on the solution side, it will not allow anodic ion transport; i.e. not allow $Cl^-$ ions to migrate from the solution to the occluded solution, but will allow outward flow of $H^+$ (Figure A1.1).

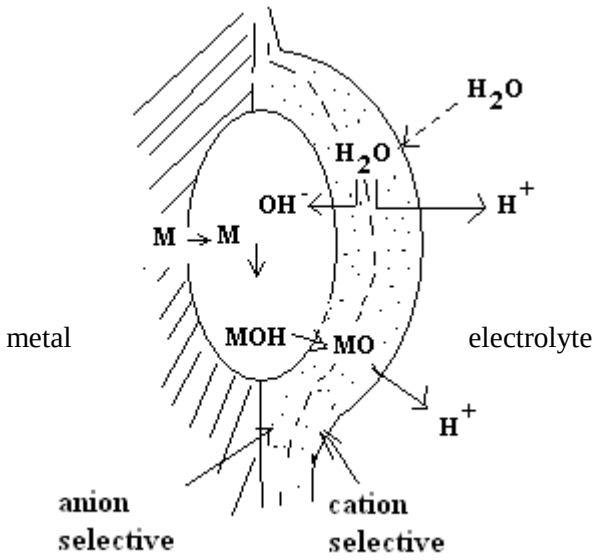


Figure A1.1 Pit initiation mechanism according to the Bipolar Ion Selective theory [77]

When a high anodic potential is applied, the electric field in the neutral region between the anion and cation selective layers becomes extremely high so that dissociation of $H_2O$ takes place, with $H^+$ diffusing outwards and $OH^-$ or $O^{2-}$ diffusing inwards to combine with the metal ion to form metal hydroxide or oxide, with the final result being formation of a dehydrated oxide layer on the metal surface.

# APPENDIX 2

## A2.1 COMMAND LINES FOR THE MCR-ALS OPTIMIZATION

The command line which was used for the MCR-ALS optimization was as follows:

[copt,sopt,sdopt,ropt,areaopt] = als(d,$x_0$,nexp,nit,[ ],tolsigma,csel,ssel)

where the input variables are:

d = the data matrix D of dimensions n × p (where n = no. of *in situ* spectra and p = wavenumbers)

$x_0$ = the matrix of pure spectral profiles of dimensions m × p (m = no. of pure component spectra)

nit = number of iterations (= 100)

nexp = number of data matrices (= 1)

tolsigma = relative change between consecutive iterations during the optimization, used to set the convergence criterion (=0.1%)

csel = matrix of concentrations or relative amounts of *in situ* spectra of dimensions p × n, if the amounts are not known they are entered as NaN

ssel = matrix of pure component spectra of dimensions m × p, used to set constraints on the optimization of the pure spectral profiles,

and where the output variables are:

copt = OPTimised Concentration: matrix of resolved concentrations (or relative amounts) of the m pure components for the data matrix, D, is of dimensions n x m

sopt = OPTimised Spectra: matrix of individual component spectra of dimensions m x p, may be equal to $x_0$ depending on how ssel was constrained

sdopt = the optimal percent lack of fit in relative standard deviation units [114]:

$$\% \text{ lack of fit} = 100 \times \sqrt{\frac{\sum_{i,j} e_{ij}^2}{\sum_{i,j} d_{ij}^2}}$$

Two values are calculated for this and returned in the sdopt output:

1) (exp) where $e_{ij}$ are the residuals obtained between the raw data set and the reproduced data set using the optimized concentration and spectra profiles, and $d_{ij}$ are the elements of the raw data set, and
2) (PCA) where $e_{ij}$ are the residuals obtained between the data set reproduced from PCA (Principal Component Analysis) and the data set reproduced using the optimized concentration and spectra profiles, and $d_{ij}$ are the elements of the dataset reproduced from PCA (using the same number of components as the raw data set).

The two values should be similar for low noise systems where all possible contributions can be described with a bilinear model [118].

ropt = matrix of residuals, obtained from comparison of the data matrix reproduced using PCA (Principal Component Analysis), $d_{PCA}$, with the data matrix reproduced using the resolved concentration and spectral profiles: ropt = $d_{PCA} - (copt \times sopt)$ , of dimensions $n \times p$

areaopt = a matrix of the area under the concentration profile of each species in the C matrix, of dimension $m \times 1$.

## A2.2 MCR-ALS RESULTS FOR *IN SITU* RAMAN SPECTRA OF IRON OXIDE COMPOUNDS FROM CHAPTER 5

### Table A2.2.1 Optimized concentration profiles for *in situ* spectra of the passive film at different potentials in cycles 1, 2, 8 and 15.

Fitting error (lack of fit, lof) in % at the optimum = 18.00(PCA) 22.38 (exp) mean = 20%

**Cycle 1**

| Data File | Applied Potential / V | Lepidocrocite | Goethite | Feroxyhyte | Maghemite |
|---|---|---|---|---|---|
| isjr2 | -1.2 | 0.077 | 0.029 | 0.011 | 0.030 |
| isjr3 | -0.92 | 0.000 | 0.000 | 0.044 | 0.016 |
| isjr4 | -0.71 | 0.176 | 0.051 | 0.086 | 0.000 |
| isjr5 | -0.53 | 0.113 | 0.089 | 0.055 | 0.031 |
| isjr6 | -0.05 | 0.000 | 0.019 | 0.075 | 0.052 |
| isjr7 | 0.40 | 0.063 | 0.004 | 0.040 | 0.000 |
| isjr8 | 0.64 | 0.000 | 0.029 | 0.059 | 0.057 |
| isjr9 | 0.40(c) | 0.006 | 0.021 | 0.054 | 0.017 |
| isjr10 | 0.00(c) | 0.010 | 0.057 | 0.102 | 0.000 |
| isjr11 | -0.83(c) | 0.060 | 0.097 | 0.033 | 0.001 |
| isjr12 | -0.95(c) | 0.128 | 0.046 | 0.041 | 0.011 |

**Cycle 2**

| Data File | Applied Potential / V | Lepidocrocite | Goethite | Feroxyhyte | Maghemite |
|---|---|---|---|---|---|
| isjr13 | -1.2 | 0.051 | 0.033 | 0.096 | 0.012 |
| isjr14 | -0.92 | 0.000 | 0.023 | 0.041 | 0.027 |
| isjr15 | -0.71 | 0.020 | 0.030 | 0.081 | 0.067 |
| isjr16 | -0.52 | 0.016 | 0.026 | 0.053 | 0.024 |
| isjr17 | -0.05 | 0.043 | 0.014 | 0.067 | 0.030 |
| isjr18 | 0.42(c) | 0.044 | 0.013 | 0.074 | 0.037 |
| isjr20 | -0.80(c) | 0.177 | 0.062 | 0.092 | 0.016 |
| isjr21 | -1.20(c) | 0.000 | 0.021 | 0.061 | 0.069 |

**Cycle 8**

| Data File | Applied Potential / V | Lepidocrocite | Goethite | Feroxyhyte | Maghemite |
|---|---|---|---|---|---|
| isjr71 | -1.2 | 0.010 | 0.000 | 0.080 | 0.058 |
| isjr81n | -0.95 | 0.094 | 0.032 | 0.064 | 0.028 |
| isjr82n | -0.75 | 0.111 | 0.068 | 0.029 | 0.003 |
| isjr83n | -0.56 | 0.126 | 0.078 | 0.018 | 0.027 |
| isjr84n | 0.00 | 0.108 | 0.061 | 0.062 | 0.036 |
| isjr85n | 0.67(c) | 0.000 | 0.016 | 0.000 | 0.125 |
| isjr86n | -0.78(c) | 0.000 | 0.023 | 0.002 | 0.155 |
| isjr87n | -1.12(c) | 0.029 | 0.051 | 0.052 | 0.065 |

**Cycle 15**

| Data File | Applied Potential / V | Lepidocrocite | Goethite | Feroxyhyte | Maghemite |
|---|---|---|---|---|---|
| isjr152n | -1.20 | 0.010 | 0.000 | 0.07 | 0.032 |
| isjr153n | -0.82 | 0.060 | 0.026 | 0.004 | 0.010 |
| isjr154n | -0.43 | 0.058 | 0.017 | 0.015 | 0.000 |
| isjr155n | 0.01 | 0.000 | 0.000 | 0.020 | 0.068 |
| isjr156n | 0.00(c) | 0.016 | 0.019 | 0.017 | 0.002 |
| isjr157n | -0.77(c) | 0.010 | 0.016 | 0.018 | 0.002 |
| isjr158n | -1.02(c) | 0.000 | 0.016 | 0.026 | 0.096 |

## A2.3 MCR-ALS RESULTS FOR *IN SITU* RAMAN SPECTRA OF $H_2O$ FROM CHAPTER 5

### Table A2.3.1 Optimized concentration profiles for *in situ* spectra of the OH stretch region

Fitting error (lack of fit, lof) in % at the optimum = 1.94 (PCA) 2.40 (exp)
mean = 2.2%

| Spectrum File | Applied Potential / V | Copt ($H_2O$) | Copt (Instr. Pks) | $H_2O$ (normalized) |
|---|---|---|---|---|
| **isfei202abn** | **-1.00 (Pk I)** | 0.730 | 0.800 | 1.097 |
| **isfei203bbn** | **-0.88 (Pk II)** | 0.920 | 0.892 | 0.969 |
| **isfei204bn** | **-0.65 (Pk III)** | 1.051 | 0.993 | 0.944 |
| **Isfei205abn** | **-0.50** | 0.620 | 1.048 | 1.690 |
| **isfei206bbn** | **-0.30** | 0.740 | 1.171 | 1.582 |
| **isfei207abn** | **0.00** | 0.842 | 0.608 | 0.722 |
| **Isfei208bbn** | **+0.55** | 1.047 | 0.427 | 0.408 |

## A2.4 MCR-ALS RESULTS FOR *IN SITU* RAMAN SPECTRA OF $H_2O$ FROM CHAPTER 6

**Table A2.4.1 Optimized concentration profiles for *in situ* spectra of the OH stretch region after addition of 0.05 M NaCl**

Fitting error (lack of fit, lof) in % at the optimum = 1.52 (PCA) 2.55 (exp), mean = 2.0%

| Spectral file | Applied Potential / V | Instrument peaks | $H_2O$ | $H_2O$ (normalized) |
|---|---|---|---|---|
| **21dn0551b** | **-0.55** | 0.194 | 1.239 | 0.157 |
| **21dn0452b** | **-0.45** | 0.381 | 1.355 | 0.282 |
| **21dn0302b** | **-0.30** | 0.391 | 1.585 | 0.247 |
| **21dn0251b** | **-0.25** | 0.378 | 1.305 | 0.289 |
| **21dn0152b** | **-0.15** | 0.298 | 1.518 | 0.197 |
| **21dn0101b** | **-0.10** | 0.380 | 1.809 | 0.210 |
| **21dn0002b** | **0.00** | 0.305 | 2.051 | 0.149 |
| **21dp0101b** | **0.10** | 0.318 | 2.030 | 0.157 |
| **21dp0201b** | **0.20** | 0.234 | 1.673 | 0.140 |
| **21dp0302b** | **0.30** | 0.316 | 1.988 | 0.159 |

## A2.5 MCR-ALS RESULTS FOR *IN SITU* RAMAN SPECTRA OF SURFACE AT PITTING CONDITIONS AND AT DIFFERENT POTENTIALS IN THE PASSIVE REGION AFTER ADDITION OF CHLORIDE FROM CHAPTER 6

**Table A2.5.1 Optimized concentration profiles for *in situ* spectra at different potentials after addition of 0.05M NaCl.**

Fitting error (lack of fit, lof) in % at the optimum = 8.20 (PCA) 8.69(exp) (mean = 8. 5%)

| Spectral File | Applied Potential /V | Akaga-neite | Feroxy-hyte | Lepido-crocite | Magne-tite | Maghe-mite | Green Complex |
|---|---|---|---|---|---|---|---|
| **isn551bn** | **-0.55 V** | 0.054 | 0.000 | 0.016 | 0.000 | 0.005 | 0.000 |
| **15dn045Dn** | **-0.45 V** | 0.051 | 0.000 | 0.014 | 0.000 | 0.000 | 0.000 |
| **15dn030Abn** | **-0.3 V** | 0.042 | 0.000 | 0.012 | 0.000 | 0.004 | 0.000 |
| **15dn025Bn** | **-0.25 V** | 0.045 | 0.000 | 0.000 | 0.000 | 0.006 | 0.059 |
| **15dn015Abn** | **-0.15 V** | 0.088 | 0.000 | 0.025 | 0.000 | 0.007 | 0.030 |
| **15dn010Abn** | **-0.1 V** | 0.047 | 0.000 | 0.019 | 0.000 | 0.017 | 0.021 |
| **15dn00Abn** | **0 V** | 0.031 | 0.004 | 0.016 | 0.000 | 0.015 | 0.113 |
| **15dp15Cn** | **+0.1 V** | 0.006 | 0.017 | 0.000 | 0.000 | 0.005 | 0.056 |
| **15dp020Fbn** | **+0.2 V** | 0.003 | 0.033 | 0.000 | 0.000 | 0.009 | 0.052 |
| **15dp035Abn** | **+0.3V** | 0.002 | 0.043 | 0.000 | 0.000 | 0.000 | 0.038 |
| **15dP035Dbn** | **+0.3 V Pit** | 0.003 | 0.038 | 0.000 | 0.223 | 0.000 | 0.000 |

**Table A2.5.2 Optimized concentration profiles for *in situ* spectra during Pitting at +0.1 V**

Fitting error (lack of fit, lof) in % at the optimum = 5.18(PCA) 6.94(exp) (mean = 6.1%)

| Spectral File | +0.1 V Area | Akaga-neite | Feroxy-hyte | Lepido-crocite | Magne-tite | Maghe-mite | Green Complex |
|---|---|---|---|---|---|---|---|
| **esmrn1bn** | **Surface** | 0.026 | 0.008 | 0.007 | 0.004 | 0.008 | 0.000 |
| **esmrnpit1bn** | **Pit 1 edge** | 0.003 | 0.037 | 0.010 | 0.000 | 0.015 | 0.000 |
| **espit1bn** | **Pit 1** | 0.015 | 0.105 | 0.000 | 0.024 | 0.010 | 0.000 |
| **esmrnpit2bn** | **Adj pit2** | 0.033 | 0.026 | 0.008 | 0.000 | 0.000 | 0.000 |
| **espit2bn** | **Pit 2** | 0.025 | 0.071 | 0.000 | 0.091 | 0.004 | 0.000 |
| **esmrn8bn** | **Surface** | 0.011 | 0.015 | 0.005 | 0.000 | 0.000 | 0.024 |

**Table A2.5.3 Optimized concentration profiles for *in situ* spectra during Pitting at +0.3 V**

Fitting error (lack of fit, lof) in % at the optimum = 5.18(PCA) 6.94(exp) (mean = 6.1%)

| Spectral File | +0.3 V Area | Akaga-neite | Feroxy-hyte | Lepido-crocite | Magne-tite | Maghe-mite | Green Complex |
|---|---|---|---|---|---|---|---|
| **SurfAbn** | **Surface** | 0.045 | 0.000 | 0.011 | 0.000 | 0.000 | 0.000 |
| **Pit3Ebn** | **Pit 3 edge** | 0.001 | 0.016 | 0.047 | 0.049 | 0.028 | 0.000 |
| **15D30Pbn** | **Pit 3** | 0.016 | 0.061 | 0.000 | 0.093 | 0.000 | 0.000 |
| **15D30PSBn** | **Surface** | 0.023 | 0.051 | 0.000 | 0.000 | 0.000 | 0.025 |
| **15D30PAbn** | **Adj pit 4** | 0.013 | 0.047 | 0.000 | 0.007 | 0.000 | 0.000 |
| **15D30P4bn** | **Pit 4** | 0.029 | 0.045 | 0.000 | 0.113 | 0.000 | 0.000 |
| **15D30P5bn** | **Pit 5** | 0.017 | 0.074 | 0.000 | 0.154 | 0.002 | 0.000 |

## A2.6 MCR-ALS RESULTS FOR *IN SITU* RAMAN SPECTRA OF SURFACE AT *EX SITU* SPECTRA OF PIT AREA FROM CHAPTER 6

**Table A2.6.1 Optimized concentration profiles for *ex situ* spectrum of pit area**

Fitting error (lack of fit, lof) in % at the optimum = 1.14 (PCA) 2.25 (exp) (mean = 1.7%)

| Spectral File | Feroxyhyte | Hematite | Magnetite |
|---|---|---|---|
| **Pit centre** | 0.030 | 0.000 | 0.161 |
| **Adj. Surface** | 0.143 | 0.011 | 0.083 |